Development of Natural Iron-Based Nano-Rock Modulated Piezo-Responsive Membranes for Simultaneous Piezoelectric Energy Harvesting and Piezocatalytic Wastewater Remediation

Thesis submitted to

Jadavpur University

By

Saheli Ghosh

In partial fulfilment of the requirements for the degree of

Doctor of Philosophy (Ph.D.) in Science

Department of Physics

Jadavpur University

Jadavpur, Kolkata-700032

West Bengal, India

2024

FACULTY OF SCIENCE : DEPARTMENT OF PHYSICS

Certificate from the Supervisors

This is to certify that the thesis entitled *" Development of Natural Iron-Based Nano-Rock Modulated Piezo-Responsive Membranes for Simultaneous Piezoelectric Energy Harvesting and Piezocatalytic Wastewater Remediation"* Submitted by Ms. Saheli Ghosh who got her name registered on 09/03/2022 (Index no.: **91/22/Phys./27** & Registration Number: **SOPHY1109122**) for the award of Ph.D. (Science) Degree of Jadavpur University, is absolutely based upon her own work under the supervision of Prof. Sukhen Das and Dr. Ruma Basu and that neither this thesis nor any part of it has been submitted for either any degree/diploma or any other academic award anywhere before.

Sukhen Das 28/05/2024

Prof. Sukhen Das

Dept. of Physics
Jadavpur University

Prof. Sukhen Das
Department of Physics,
Jadavpur University
Kolkata - 700 032

Ruma Basu 28/5/24

Dr. Ruma Basu

Dept. of Physics
Jogamaya Devi College

Dr. Ruma Basu
Associate Professor
Physics Department
Jogamaya Devi College
92, S. P. Mukherjee Road
Kolkata - 700 026

* Established on and from 24th December, 1955 vide Notification No.10986-Edn/IU-42/55 dated 6th December, 1955 under Jadavpur University Act, 1955 (West Bengal Act XXXIII of 1955) followed by Jadavpur University Act, 1981 (West Bengal Act XXIV of 1981)

ফোন : +৯১-৩৩-২৪১৩-৮৯১৭
ফ্যাক্স : +৯১-৩৩-২৪১৩-৮৯১৭

Website : www.jadavpur.edu

Phone : + 91-33-2413-8917
Fax : + 91-33-2413-8917

Certificate of Similarity Check

This is to certify that the plagiarism checking for this thesis entitled *"Development of Natural Iron-Based Nano-Rock Modulated Piezo-Responsive Membranes for Simultaneous Piezoelectric Energy Harvesting and Piezocatalytic Wastewater Remediation"* authored by Ms. Saheli Ghosh has been performed using professional plagiarism prevention software iThenticate. According to the report generated after plagiarism checking there is a 05% similarity in this thesis, which is in the category "Level 0" (minor similarities) as per the "Promotion of Academic Integrity and Prevention of Plagiarism in Higher Education Institutions Regulations, 2018" of the University Grand Commission (UGC) of India. The common knowledge or coincidental terms up to 10 (ten) consecutive words (as prescribed in the above said UGC Regulation up to 14 (fourteen) terms for such common knowledge or coincidental terms can be excluded) and own works of the candidate published in various peer-reviewed journals (those are attached in the thesis) are excluded from the similarity checking. It is certified that the present thesis submitted by Ms. Saheli Ghosh is plagiarism-free and has followed standard norms of academic integrity and scientific ethics.

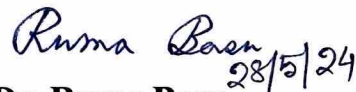*Sukhen Das* 28/06/2024

Prof. Sukhen Das
Dept. of Physics
Jadavpur University

Prof. Sukhen Das
Department of Physics,
Jadavpur University
Kolkata - 700 032

Ruma Basu 28/5/24

Dr. Ruma Basu
Dept. of Physics
Jogamaya Devi College

Dr. Ruma Basu
Associate Professor
Physics Department
Jogamaya Devi College
92, S. P. Mukherjee Road,
Kolkata - 700 026

* Established on and from 24th December, 1955 vide Notification No.10986-Edn/IU-42/55 dated 6th December, 1955 under Jadavpur University Act, 1955 (West Bengal Act XXXIII of 1955) followed by Jadavpur University Act, 1981 (West Bengal Act XXIV of 1981)

ফোন : +৯১-৩৩-২৪১৩-৮৯১৭
ফ্যাক্স : +৯১-৩৩-২৪১৩-৮৯১৭

Website : www.jadavpur.edu

Phone : + 91-33-2413-8917
Fax : + 91-33-2413-8917

Dedicated to

my family

Abstract

Development of Natural Iron-Based Nano-Rock Modulated Piezo-Responsive Membranes for Simultaneous Piezoelectric Energy Harvesting and Piezocatalytic Wastewater Remediation

Saheli Ghosh

Index No.: 91/22/Phys./27   **Registration No.: SOPHY1109122**

Abstract: The world faces a looming energy crisis due to dwindling fossil fuels, geopolitical conflicts disrupting supply chains, inadequate investments in renewables, and soaring global energy demand. Besides, rapid industrialization and growing population generate severe water pollution. Addressing this requires a shift to cleaner energy options and reconsidering production techniques to minimize environmental harm. To combat the situation this work encompasses the synthesis of iron-based nanostructures specifically natural α-hematite because of their nontoxicity, abundance, and biocompatibility in nature besides their exceptional other physicochemical properties. The doping of foreign materials into natural α-hematite such as rare-earth metals (Gadolinium), carbon nanotubes (CNT), etc. into the matrices of natural nano-rock and incorporation into the various polymer matrices (PVDF) unveils the structure-property correlation of such composite systems by enhancing energy harvesting efficacy, especially the piezo energy. As piezoelectric energy harvesting stands as a promising avenue to simultaneously address both the energy crisis and water pollution challenges. This innovative technology harnesses energy from mechanical vibrations, including movement in water bodies, to generate electricity. In this study, the naturally occurring α-hematite-based device can produce a voltage of 53.9V and a current of 011.6 µA with a hand-tapping (force of 14.99N). Even after 75 days, the efficiency remains relatively constant. In addition, the fabricated device generates up to 8V under the flow of water. As vibrations or mechanical stress occur, these materials can simultaneously facilitate catalytic reactions to break down pollutants present in water known as piezocatalysis which has also been employed in this work to degrade carcinogenic dyes like RhB, Congo red, etc. The membrane degrades RhB dye 98.7% under ultrasonic vibration of 33KHz and the membrane is also recyclable for up to 10 cycles without altering the efficacy. Hence integration of these two technologies following the same mechanisms can be a promising avenue to simultaneously address both the energy crisis and water pollution challenges. Thus, this study presents a dual solution by offering clean energy generation and mitigation of water pollution, showcasing the potential of innovative technologies like piezoelectric energy harvesting in tackling these interconnected global challenges.

Acknowledgement

whenever it was needed. Their contributions have played a significant role in shaping my journey.

Most importantly, I would like to express my deepest gratitude to my family for their love, support, and encouragement throughout my journey towards achieving my Ph.D. Ma, Baba, your inspiration, sacrifices, and belief in my potential have been the bedrock upon which I built my academic pursuits. Didi, your encouraging words, laughter, and love have fueled me through the toughest of times. Bonkai (Nephew), your boundless love, innocent smiles, and prayers for me have been a constant source of strength and inspiration throughout my PhD journey. My beloved family, thank you for instilling in me resilience, inspiring me to fearlessly pursue knowledge, and being my source of strength through this incredible journey. I am profoundly grateful for your presence in my life. This achievement is as much theirs as it is mine, and I am forever indebted to them for their endless love and support.

Saheli Ghosh

Saheli Ghosh

CONTENTS

Chapter 1: Introduction

Chapter 4: Water flow and finger-tapping mediated piezoelectric energy generation and carcinogenic dye degradation using a Gd-incorporated natural hematite-based flexible PVDF-HFP membrane

Chapter 5: *Energy harvesting from non-invasive sources and elimination of carcinogenic dye from wastewater using self-poled natural rock-based piezo-responsive membrane*

Publications and Seminar Certificates

ABBREVIATIONS

WHO: World Health Organisation

H_2O: Water

CO_2: Carbond dioxide

CFU: Colony-forming unit

ROS: Reactive oxygen species

$AgNO_3$: Silver nitrate

EDTA: Ethylenediaminetetraacetic acid

BQ: p-benzoquinone

TBA: Tertbutanol

VB: Valance band

CB: Conduction band

RhB: Rhodamine B

MO: Methylene blue

PNP: Piezoelectric nanoparticles

0D- 0 dimensional

1D- 1 dimensional

2D- 2 dimensional

3D- 3 dimensional

AlN: Aluminum Nitride

NP: Nanoparticles

$BiFeO_3$: Bismuth ferrite

$BaTiO_3$: Barium titanate

$SrRuO_3$: Strontium ruthenates

d_{33}: Piezoelectric coefficient (polarisation induced in direction z-axis per unit stress applied in z-axis)

d_{13}: Piezoelectric coefficient

d_{15}: Piezoelectric coefficient polarization induced in the axis per unit shear stress applied about the axis)

PVC: Polyvinyl Chloride

PAN: Polyacrylonitrile

PVDF: Polyvinylidene fluoride

PVAc: Polyvinyl acetate

PLLA: poly-L-lactic acid

DMSO: Dimethyl sulfoxide

PZT: Lead-zirconate-titanate

BNT: Bismuth sodium titanate

$BaTiO_3$: Barium titanate

TiO_2: Titanium oxide

Fe_3O_4: Iron Oxide

ZnO: Zinc Oxide

CNT: Carbon nanotube

C dots: Carbon dot

rGO: Reduced-Graphene oxide

MWCNT: Multi-walled carbon nanotubes

MOD: Metal-organic deposition

PVDF-TrFE: Polyvinylidene fluoride-co-trifluoroethylene

PVDF-HFP: Polyvinylidene fluoride-hexafluoropropylene

PVDF-CTFE: Polyvinylidene fluoride-co-chlorotrifluoroethylene

VSSP: Viscous Solution Spinning

PMMA: Polymethyl methacrylate

PDMS: Polydimethylsiloxane

PHP: Fluoride hexafluoropropylene

PZT: Lead zirconate titanate

MoS_2: Molybdenum disulfide

TC: Curie temperature

NBT: $Na_{0.5}Bi_{0.5}TiO_3$ (Sodium Bismuth Titanate)

BFO: Bismuth ferrite

4-CP: 4-chlorophenol

Au/BiVO$_4$: Au-modified Bismuth vanadate

CIP: Ciprofloxacin

RNA: Ribonucleic acid

DNA: Deoxyribonucleic acid

Au@BTO: Au-doped Barrium titanate

XRD- X-ray diffraction

FTIR- Fourier Transform Infrared Spectroscopy

FESEM- Field Emission Scanning Electron Microscope

TGA- Thermogravimetric Analyzer

DTA- Differential Thermal Analyzer

DFT- Density Functional Theory

KeV- Kilo electron volt

TEM- Transmission Electron Microscope

kV- Kilovolt

JCPDS- Joint Committee on Powder Diffraction Standards

ε' - Dielectric permittivity

σ_{ac}- AC Conductivity

PL- Photoluminescence

EDS/EDAX- Energy-Dispersive X-ray Spectrometer

UV- Ultra Violet

VESTA- Visualization for Electronic and Structural Analysis

ROS- Reactive Oxygen Species

LIST OF PUBLICATIONS

Thesis publications:

1. **Ghosh, S.,** Roy, S., Bardhan, S., Khatua, N., Bhowal, B., Chanda, D.K., Das, S., Mondal, D., Basu, R. and Das, S., 2021. Effect of Size Fractionation on Purity, Thermal Stability and Electrical Properties of Natural Hematite. *Journal of Electronic Materials*, 50(7), pp.3836-3845.

2. **Ghosh, S.,** Bardhan, S., Mondal, D., Sarkar, D., Roy, J., Roy, S., ... & Das, S. (2023). Natural hematite-based self-poled piezo-responsive membrane for harvesting energy from water flow and catalytic removal of organic dye. *Ceramics International*, *49*(9), 14710-14718.

3. **Ghosh, S.,** Mondal, D., Roy, S., & Das, S. (2023). Recent advances in the synthesis and biomedical applications of α-hematite nanoparticles. *Sayam-A Journal of Science*, *1*(1), 01-08.

4. **Ghosh, S.,** Bardhan, S., Mondal, D., Sarkar, D., Roy, J., Roy, S., ... & Das, S. (2023). Natural hematite-based self-poled piezo-responsive membrane for harvesting energy from water flow and catalytic removal of organic dye. Ceramics International, 49(9), 14710-14718.

Co-author publications:

5. Roy, S., Bardhan, S., Pal, K., **Ghosh, S.,** Mandal, P., Das, S. and Das, S., 2018. Crystallinity mediated variation in optical and electrical properties of hydrothermally synthesized boehmite (γ-AlOOH) nanoparticles. *Journal of Alloys and Compounds*, 763, pp.749-758.

6. Roy, S., Pal, K., Bardhan, S., Maity, S., Chanda, D.K., **Ghosh, S**., Karmakar, P. and Das, S., 2019. Gd (III)-doped boehmite nanoparticle: an emergent material for the fluorescent sensing of Cr (VI) in wastewater and live cells. *Inorganic Chemistry*, 58(13), pp.8369-8378.

7. Roy, S., Bardhan, S., Chanda, D.K., **Ghosh, S**., Mondal, D., Roy, J. and Das, S., 2020. Development of a Cu (II) doped boehmite based multifunctional sensor for detection and removal of Cr (VI) from wastewater and conversion of Cr (VI) into an energy harvesting source. *Dalton Transactions*, 49(20), pp.6607-6615.

8. Roy, S., Bardhan, S., Chanda, D.K., Maity, A., **Ghosh, S**., Mondal, D., Singh, S. and Das, S., 2020. Cu (II) and Gd (III) doped boehmite nanostructures: a comparative study of electrical property and thermal stability. *Materials Research Express*, 7(2), p.025020.

9. Roy, S., Bardhan, S., Chanda, D. K., **Ghosh, S.,** Mondal, D., Roy, J., & Das, S. (2020). Development of a Cu (II) doped boehmite based multifunctional sensor for detection

and removal of Cr (VI) from wastewater and conversion of Cr (VI) into an energy harvesting source. Dalton Transactions, 49(20), 6607-6615.

10. Bardhan, S., Roy, S., Chanda, D.K., **Ghosh, S.,** Mondal, D., Das, S. and Das, S., 2020. Nitrogenous carbon dot decorated natural microcline: an ameliorative dual fluorometric probe for Fe 3+ and Cr 6+ detection. *Dalton Transactions*, 49(30), pp.10554-10566.

11. Ghosh, B., Roy, S., Bardhan, S., Mondal, D., Saha, I., **Ghosh, S.,** Basu, R., Karmakar, P., Das, K. and Das, S., 2022. Biocompatible carbon dot decorated α-FeOOH nanohybrid for an effective fluorometric sensing of Cr (VI) in wastewater and living cells. Journal of Fluorescence, pp.1-12.

12. Mondal, D., Roy, S., Bardhan, S., Das, R., Maity, A., Chanda, D.K., Das, S., **Ghosh, S.,** Basu, R. and Das, S., 2022. Effect of microstructural evolution of natural kaolinite due to MWCNT doping: a futuristic 'green electrode'for energy harvesting applications. Journal of Materials Science: Materials in Electronics, pp.1-17.

13. Roy, J., Mukhopadhyay, L., Bardhan, S., Mondal, D., **Ghosh, S**., Chakraborty, S., ... & Das, S. (2022). Piezo-responsive bismuth ferrite nanoparticles mediated catalytic degradation of rhodamine-B and pathogenic E. coli in aqueous medium and its extraction using external magnetic stimulation after successful treatment. *Dalton Transactions*.

14. Mondal,D., Bardhan, S., Das, N., Roy, J., **Ghosh, S.,** Roy, S., Basu, R.,Das, S.,2022 Natural clay-based reusable piezo-responsive membrane for water droplet mediated energy harvesting, degradation of organic dye and pathogenic bacteria.Nano Energy

15. Roy, J., Roy, S., Mondal, D., Bag, N., Chowdhury, J. R., **Ghosh, S.,** ... & Das, S. (2024). Gd-doped bismuth ferrite nanocomposite: A promising candidate for piezocatalytic degradation of organic dyes and pathogenic E. coli. Surfaces and Interfaces, 44, 103579.

16. Mondal, D., Sau, A., Roy, S., Bardhan, S., Roy, J., **Ghosh, S.,** ... & Das, S. (2023). Functionalized MWCNT-integrated natural clay nanosystem: a promising eco-friendly capacitor for energy storage applications. Journal of Materials Science: Materials in Electronics, 34(21), 1597.

17. Bag, N., Roy, J., Mondal, D., **Ghosh, S**., Bardhan, S., Roy, S., ... & Das, S. (2024). Utilization of experimental and theoretical piezoresponse of BTO nanocrystal for rapid decomposition of the pathogenic coliform bacteria. Ceramics International, 50(5), 7998-8009.

18. Roy, J., Mondal, D., Chowdhury, J. R., Bag, N., **Ghosh, S**., Roy, S., ... & Das, S. (2024). Enhanced piezocatalytic activity of BiFeO3 incorporated PVDF-HFP membrane for efficient degradation of carcinogenic industrial pollutant. Ceramics International.

19. Mondal, D., Bag, N., Roy, J., **Ghosh, S.,** Roy, S., ... & Das, S. (2024). Natural clay-modified polycatalytic membrane for removal of Coliform bacteria from wastewater. Langmuir.

LIST OF SEMINARS ATTENDED

1. Participated and presented a poster in the national seminar on "Physics at Surfaces and Interfaces of Soft Materials" organized by the Condensed Matter Physics Research Centre, Department of Physics, Jadavpur University, on 26-27 September, 2019.

2. Participated and presented a poster on "Optical Characterization" in DST-SERB Sponsored One Day Workshop on Material Synthesis and Characterization Techniques, organized by the Department of Physics, Jadavpur University, Department of Physics, 29th February, 2020.

3. Participated in the One-day International Webinar on "New Outlooks in Modern Physics" organized by the Department of Physics, in collaboration with IQAC, Basanti Devi College on 17th July (Friday) 2020.

4. Participated in the International Webinar on 'Nanotechnology Against COVID-19', Organized by Post Graduate and Research Department of Chemistry, Sree Narayana College for Women, Kollam, Kerala, India on 23 July 2020.

5. Participated in the webinar on 'Role of Symmetries in Physics' organized by the Department of Physics, in collaboration with IQAC, Asutosh College, Kolkata, held on 27th August, 2020.

6. Participated and presented a paper entitled "Piezoelectric energy generation under finger tapping and water flow using Gd-incorporated natural hematite decorated PVDF-HFP membrane" in the 7th International Conference on Nanoscience and Nanotechnology (ICONN-2023) organized by the Department of Physics and Nanotechnology, SRM IST, India on March 27- 29, 2023

7. Presented oral and poster and secured "second prize" in Basic sciences category at Anveshan-2022, National research convention, Oral and Poster: "'Vikram': An 'all-in-one' module for combating water pollution and energy crisis", Royal Global University, Assam, 1st and 2nd march 2023.

8. Presented oral and poster in Anveshan-2022, National research convention, Oral and Poster: "'Vikram': An 'all-in-one' module for combating water pollution and energy crisis", Ganpat University, Gujrat, 17th and 18th march, 2023.

9. Participated and presented a paper entitled "Natural rock-based polymeric membrane: an "all-in-one" module for combating water pollution and energy crisis" at the one day seminar in "Commemoration Of Centenary Birth Anniversary Of Prof. Shyamal Sengupta" held at Jadavpur University, Kolkata, India on 7th February 2024.

LIST OF FIGURES

Chapter 1

Chapter 2

assisted degradation of RhB (C/C$_0$) varying hematite powder, PVF0, PVF5, Control (only RhB) (c) Plots of ln(C$_0$/C) with treatment time for hematite powder, PVF0, PVF5, Control (only RhB) (d) Ultrasound-assisted degradation of RhB (C/C$_0$) representing the Scavenging experiments in presence of different oxygen species and showing •OH radicals as one of the main species for piezocatalysis,(e) Plots of ln(C$_0$/C) with treatment time for the scavenging experiment (f) Demonstration of formation of hydroxyl radical due to piezo-electric effect as supported by an increase in fluorescence intensity of 2-hydroxyterephthalic acid (g) Kinetic rate constant for degradation of RhB due to different scavengers (h) Efficiency of piezo catalytic decomposition after each cycle (i) Kinetic rate constants for hematite powder, PVF0, PVF5 and Control (only RhB)

Chapter 4

Figure 4.1 *The work plan for this chapter*

Figure 4.2 *Schematic representation of the synthesis procedure*

Figure 4.3 *(a-b) Experimental and computed XRD pattern of natural α-hematite and Gd incorporated α-hematite respectively (c) Unit cells of Gd incorporated α -hematite (d) XRD pattern of natural Gd incorporated α–hematite nanocomposite membranes suggesting that incorporation of nanocomposite into polymer matrix enhance the polar phase and found maximum in PVGF2.5.*

Figure 4.4 *(a-b) TEM image and the size distribution curve of Gd incorporated α -hematite, (c-e) FESEM micrographs of PVGF0, PVGF2.5, PVGF5, (f) EDX images Gd incorporated hematite NPs, (g-j) mapping of PVGF2.5 membrane suggesting the homogeneous distribution of doped Gd incorporated hematite in the PVDF matrix. The carbon distribution of the membrane does not show due to the use of carbon tape during the EDS mapping measurement.*

Figure 4.5 *(a) Percentage of weight losses of nanocomposite membranes, (b) Derivatives weight loss of the nanocomposite membranes suggesting better stability in doped membranes, (c) FTIR spectroscopy of PVGF0, PVGF2.5, PVGF5, shown polar phase enhancement after nanocomposite inclusion into the polymer matrix (d) Percentage β-*

phase of sample PVGF0, PVGF2.5, PVGF5, (e) Zeta potential of Gd incorporated hematite shows a high positive surface charge.

***Figure 4.6** (a) Dielectric constant with the frequency of α-hematite and Gd-incorporated α-hematite nanoparticles suggesting the Gd incorporation enhanced the NPs dielectric constant, (b) Dielectric constants of PVGF0, PVGF2.5, and PVGF5 respectively (c-d) Tangent loss of NPs and membranes suggesting low energy dissipation (e) Variation of ac conductivities with the frequency for the nanocomposite membranes show the maximum conductivity in PVGF2.5, and (f) Comparison of the dielectric constant of sample PVGF0, PVGF2.5, PVGF5 at 40Hz*

***Figure 4.7** (a) Piezoelectric coefficients of the nanocomposite membranes suggesting PVGF2.5 possess the highest d33 value, (b) Real image of the fabricated device and in the inset the fabricated PVGF2.5 nanocomposite membrane, (c,d) Open circuit voltage and short circuit current due to finger tapping on PVGF0, PVGF2.5 and PVGF5 devices, (e) piezoelectric voltage generation under different applying forces (f,g) Open circuit voltage and short circuit current of the PVGF2.5 device under water flow, (h) performance test of the device over time.*

***Figure 4.8** (a) UV-Vis spectra of dye degradation and decolorization of Rhodamine B (RhB), (b-c) Ultrasound-assisted RhB degradation ln(C_0/C) and (C/C_0) represents the scavenging studies in the presence of several oxygen species and shows •OH radicals as one of the primary species for piezocatalysis, (d) Kinetic rate constant for RhB degradation caused by various scavengers*

Chapter 5

***Figure 5.1** Schematic representation of application of Chapter 5*

***Figure 5.2** Synthesis procedure of nanocomposite*

***Figure 5.3** XRD Analysis of (a) CNT incorporated hematite NP, (b) Microstructural visualization of unit cell from VESTA software, (c) X-ray diffractograms of the nanocomposite membranes, (d-g) FESEM images of CNF0, CNF0.5, CNF1, and CNFNP,*

LIST OF TABLES

Chapter 1

Table 1.1 Different conventional solutions for water pollution

Chapter 2

Table 2.1. Structural and morphological parameters of the three different samples S1 (Bulk), S2 (Intermediate), and S3 (Nano) calculated from XRD and FESEM data

Table 2.2. Elemental composition of samples S1 (Bulk), S2 (Intermediate), S3 (Nano) analyzed from XRF

Table 2.3. Sample area, pore size, and pore volume distribution of samples S1 (Bulk), S2 (Intermediate), and S3 (Nano) from BET

Chapter 5

Table 5.1 Refined parameters of pure hematite and MWCNT-doped hematite nanoparticles

Chapter 6

Table 6.1 Comparison of piezoenergy harvesting and piezocatalysis data with previous works

Chapter 1

Introduction

Chapter 1

Introduction and methodology

In the twenty-first century, with globalization, urbanization, and modernization, the interconnected problems of the world energy crisis and rising water pollution have become crucial issues which require immediate attention [1]. The increasing need for energy due to factors such as population growth, industrialization, and technological progress has resulted in a greater burden on conventional energy sources, which in turn has exacerbated environmental degradation. In addition, the unregulated growth in energy production and consumption has played a major role in water body pollution, putting ecosystems and human health in danger.

1.1 The Energy Crisis: Context and Challenges

The foundation of modern society has been built upon the availability and utilization of energy. Nonetheless, the world is currently experiencing an energy crisis as conventional energy sources, such as coal, wood, and others, have been utilized extensively from the beginning of civilization to the present day. Non-renewable energy sources account for 85% of the energy utilized globally [3]. Therefore, these limited resources of coal, oil, natural gas, etc are quickly running out due to modernization, industrialization, and civilization raising worries about energy security and the risks to the economy, society, and environment that come with relying too much on these conventional energy sources [4]. Figure 1.1 illustrates how the energy demand is driving up continuously. Furthermore, burning fossil fuels generates greenhouse gases that exacerbate climate change and highlight how urgent it is to switch to low-carbon, sustainable energy sources [5]. Therefore, alternate renewable energy sources such as solar, wind, tidal, and mechanical energy sources should be used to combat the problem effectively.
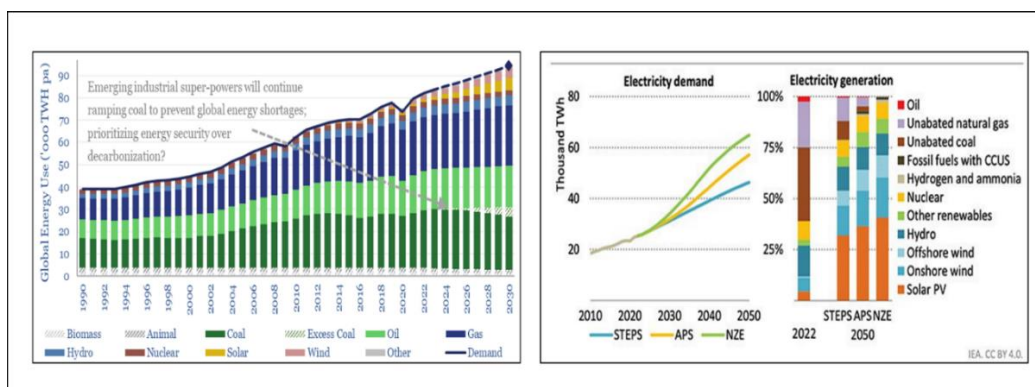
Figure 1.1 *Report of growing energy demand [Source-Thunder said energy, IEA]*

1.2 Water Pollution: Causes and Consequences

Water pollution, caused by integration of hazardous contaminants, both organic and inorganic, to water bodies, such as lakes, rivers, seas, groundwater, and even supplies of drinking water, have become a matter of grave comcern now-a-days [6]. This effect is detrimental for not just the environment but also human health. Aquatic ecosystems, biodiversity, and human health may all suffer as a result of this pollution, which can come from a variety of man-made and natural sources and activities [7]. Enormous factors, such as municipal discharge, agricultural runoff, industrial discharge, and so on, contribute to water pollution.

On the other hand, the energy sector, a fundamental pillar of modern civilization, significantly contributes to water pollution through various stages of energy production, distribution, and consumption. Mining activities, essential for extracting fossil fuels often result in the leaching of toxic substances and heavy metals into nearby water sources [8]. Furthermore, the disposal of untreated industrial effluents and the cooling processes in thermal power plants discharge heated water into rivers and lakes, causing thermal pollution and altering aquatic ecosystems [9].

In addition, a variety of untreated carcinogenic and poisonous effluents from municipalities, companies, farms, and hospitals are being inserted into watebodies erratically. The origins of water contamination and the different waste classes that contaminate water are depicted in Figure 1.2 depicts the causes of water pollution and how they lead to the water crisis [10]. By 2050, only 1% of the water will be available to humans, making it difficult to obtain fresh water [11]. These pollutants not only contaminate surface and groundwater but also pose severe threats to biodiversity and human health, often disproportionately affecting marginalized communities relying on these water sources for sustenance.
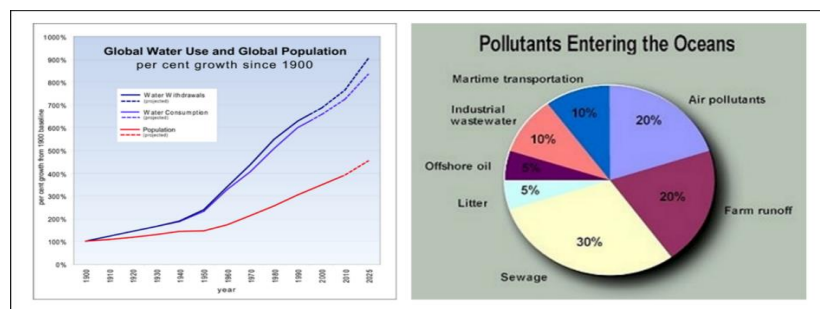
Figure 1.2 *Report of water crisis and water pollution [Source- CDD India, Google (mooredope)]*

1.3 Status of energy crisis in India

An imbalance between supply and demand has resulted in occasional shortages of power, especially in rural parts of India. The country has faced several issues in the energy industry. Coal is still the dominant source of electricity generation [12], causing environmental issues and air pollution even with advancements in the integration of renewable energy. Despite remarkable gains of India in the utilization of renewable energy, technical obstacles remain when integrating intermittent sources like solar and wind into the system [13]. Government measures are promoting the use of LPG over traditional biomass since access to clean cooking fuels is still a problem for many [14]. Considerable capital has been invested in wind and solar projects as a result of policies that have been put in place to increase the use of renewable energy sources, increase energy efficiency, and improve power infrastructure [15]. However, the energy challenges of nation still persist, including ensuring reliable electricity access for all and diversifying its energy mix away from fossil fuels, showcasing the need for ongoing efforts and policy innovations to address the evolving energy landscape.

1.4 Status of water pollution in India

India has serious problems with water pollution from a variety of causes, such as poor waste disposal, untreated sewage, industrial effluents, and agricultural runoff [16]. The rivers, lakes, and groundwater supplies are losing quality due to pollutants such heavy metals, chemicals, and biological contaminants [17]. Growing industrialization and urbanization have raised the pollution levels in water bodies, endangering human health, ecosystems, and access to clean water.

Wastewater management in India remains a critical concern [18]. Untreated wastewater discharges into aquatic bodies comprise a significant amount of both industrial and household effluents. Despite attempts to upgrade the infrastructure for sewage treatment in metropolitan areas, there is still a sizable discrepancy between wastewater generation and treatment capacity [19]. Waterways are frequently exposed to untreated or partially treated sewage because treatment plants operate below their intended capabilities. Lack of adequate sewage treatment and sanitation infrastructure worsens the issue in rural regions.

The Indian government has launched several initiatives to address the problem water pollution and improve wastewater management [20-22]. Programs such as the National Mission for Clean Ganga (Namami Gange) aim to rejuvenate the Ganges River by

controlling pollution, conserving biodiversity, and promoting sustainable wastewater management practices [21]. Additionally, the Atal Mission for Rejuvenation and Urban Transformation (AMRUT) focuses on providing basic services, including water supply and sewage management, in urban areas [22].

Challenges persist in ensuring the effective implementation of these initiatives, including inadequate infrastructure, funding constraints, regulatory enforcement, and the need for community participation [19]. Improving wastewater treatment infrastructure, enhancing monitoring mechanisms, promoting water conservation practices, and raising public awareness about water pollution are crucial steps in addressing water quality concerns of the country.

1.5 Renewable energy sources

One of the most important approaches to solving the urgent energy issue is the global search for renewable energy sources. With depleting reserves of non-renewable resources and escalating environmental concerns, the transition towards renewable energy emerges as a fundamental solution. Harnessing sources such as solar, wind, hydroelectric, geothermal, and biomass offers multifaceted benefits [23]. These resources are widely available, plentiful, and, in contrast to fossil fuels, have less of an adverse effect on the environment, lowering greenhouse gas emissions and slowing down the effects of climate change. Additionally, making investments in renewable energy infrastructure promotes energy security, and independence, and creates jobs in expanding industries [24]. Countries all around the globe may set the path for a sustainable future by giving priority to the development and implementation of renewable energy technologies, guaranteeing dependable access to energy while reducing the negative consequences of the energy crisis. Renewable energy sources are derived from natural processes that are continuously replenished [25]. When compared to non-renewable sources, they have less of an influence on the environment and emit little to no greenhouse gases, which makes them sustainable and ecologically benign. Below are the primary categories of sustainable energy sources like solar energy, wind energy, hydroelectric energy, geothermal energy, biomass energy, tide and wave energy, etc [26].

Solar energy, the most common renewable energy, converts sunlight directly into electricity using solar cells made of semiconductor materials. Modupeola Dada et. al. has discussed how photovoltaic devices are employed to address the increasing need for energy [27]. This

uses sunlight to heat a fluid, typically water or oil, to produce steam and generate electricity through turbines. Layth M. ABD ALI1 et al. have conducted experiments to explore the possibility of developing thermal power plants that use conventional steam to generate electricity [28].

Wind energy is another source of renewable energy that converts the kinetic energy of the wind into mechanical power, which is then used to generate electricity. Lin Pan et al. have proposed an enhanced Sliding Mode Control (SMC) based on the Wind Energy Conversion System (WECS) with offshore wind turbine Permanent Magnet Synchronous Generator (PMSG) coupled to the grid [29].

Hydroelectric energy uses the kinetic energy of flowing water, often harnessed through dams or flowing rivers, to generate electricity. Siri et al. provide information regarding the capability for generating electricity from water that has led to hydropower being a key renewable energy source, as well as how hydropower contributes to a holistic energy future [30].

Geothermal energy utilizes heat from the interior of the earth to produce steam, which drives turbines and generates electricity. Assad et al. studied a hybrid system to harvest geothermal energy, consisting of a single flash steam geothermal power plant and a solar thermal system with a parabolic trough collector [31].

Biomass energy involves using organic materials, such as wood, agricultural residues, and organic waste, to produce heat, electricity, or biofuels through combustion or other processes. Makul et al. have analyzed the various biomass sources and their potential for application as alternative energy options [32].

Tidal energy captures the energy from the rise and fall of tides to generate electricity. The energy extracted from the tides through consistent and predicted vertical motions of the water, resulting in tidal currents, might be transformed into kinetic energy to generate power. Chowdhury et al. have depicted the current prospects of tidal energy technology in the in the context of an energy crisis [33]. Wave energy, quite similar to tidal energy, converts the kinetic energy from ocean waves into electricity. Rodrigues et al. have portrayed how wave energy can be harvested using triboelectric nanogenerators [34].

1.6 Different processes of wastewater remediation

Wastewater treatment uses a variety of scientific techniques and technology to get rid of impurities. Ledezma et al. have depicted the different conventional solutions for water pollution such as adsorption, coagulation, precipitation, ion exchange, etc [35]. Rafiq et al. have described the photocatalytic degradation for wastewater treatment [36]. Several of these techniques have been mentioned in the following table 1

Table 1.1 Different conventional solutions for water pollution

Processes	Techniques	Mechanisms	References
Physical Process	Filtration	uses physical barriers—such as gravel, sand, or membranes—to keep the water and solid particles apart	[37]
	Adsorption	involves drawing impurities out of the water by attaching them to a surface, such as activated carbon or certain clays	[38]
	Sedimentation	permits heavier particles to separate from the water by settling to the bottom of a tank due to gravity using a gravitational field	[39]
Chemical Process	Coagulation/Flocculation	Wastewater is treated with chemicals to create floc, or bigger particles that are easier to remove	[40]
	Precipitation	In order to create insoluble compounds that separate from the water, chemicals are added	[41]
	Oxidation-Reduction	Organic pollutants are decomposed by chemical oxidation (like hydrogen peroxide, ozone, or chlorine)	[42]

Biological Process	Activated Sludge	Use aerobic microorganisms to break down organic content in wastewater	[43]
	Biological Nutrient Removal	Add certain microorganisms to wastewater to extract nutrients like phosphate and nitrogen	[44]
	Constructed Wetlands	utilizes microbiological, adsorption, and filtration mechanisms found in wetland habitats to naturally remove contaminants	[45]
Advanced Treatment Technologies	Membrane Filtration	use fine-pore membranes to separate impurities from water	[46]
	Reverse Osmosis	applies pressure to remove impurities by forcing water through a semi-permeable membrane	[47]
	Ion Exchange	efficiently removes impurities by exchanging ions in the water with ions bound to a resin	[48]
Electrochemical Process	Electrocoagulation	Uses an electric current to destabilize and accumulate pollutants to make their removal easier	[49]
	Electrochemical Oxidation/Reduction	Induces oxidation or reduction processes using electrodes to break down contaminants	[50]
	Photocatalysis	uses light (usually UV) to activate catalysts (like titanium dioxide) to convert organic molecules into less toxic and simpler forms	[51]

Numerous criteria, such as the kind and concentration of pollutants, the amount of wastewater, environmental requirements, and the viability of the economic viability of the process, influence the choice of remediation technique or combination of processes. Although these processes have gained the interest of researchers over time, however, their low efficiency, long reaction time, low biocompatibility, production of secondary pollution as end products, and costly procedure hinder their advancement.

As a solution piezo-responsive simultaneous energy generation and wastewater treatment came in front row to new generation researchers [52-54].

1.7 Piezoelectric energy harvesting: an inventive remedy

Piezoelectric energy harvesting represents an innovative solution in the dominion of renewable energy by tapping into mechanical vibrations or movements and converting them into electrical energy[53,55]. Piezoelectric materials generate a voltage when subjected to mechanical stress, such as vibrations, pressure, or movement [56]. Incorporating piezoelectric devices into infrastructure, buildings, or wearable technology allows for the capture of otherwise wasted mechanical energy from various sources, including footsteps, vehicle movements, machinery vibrations, or even ambient vibrations in the environment [57-58].

Piezoeelectric phenomenon was first discovered by Pierre and Jacques Curie in 1980 [59]. Initially, its practical applications developed during World War I in sonar technology and extended during World War II in radar systems [60]. By this time, several piezoelectric materials had been invented and were being used in acoustic technology, sensors, actuators, and other areas [61]. Researchers are constantly investigating innovative materials to improve efficacy, reliability, and scalability, as well as to optimize device design and use in a wide range of energy-harvesting applications. Footstep energy might be captured and transformed into electricity to power sensors or lighting by being integrated into pavements, pathways, or floors in high-traffic areas [62]. Piezoelectric devices can be used to capture vibrations produced by machinery and equipment in factories or other industrial settings to create additional electricity [63-64]. In transportation hubs, vibrations from cars, trains, or other infrastructure might be captured and used to power low-power devices like lights or sensors [65]. Piezoelectric devices have the potential to monitor the structural health of infrastructure such as buildings or bridges by using vibrations [66]. They can also provide tiny quantities of electricity for local sensors or devices.

Henceforth, when integrated into various applications, piezoelectric energy harvesting contributes to a more comprehensive approach to renewable energy by tapping into otherwise untapped mechanical energy sources, thereby diversifying the renewable energy mix and possibly lessening the burden on conventional energy sources.

1.7.1 Piezo-responsive materials

There are various piezo-responsive materials like piezoelectric nanoparticles, polymers, nanocomposites, perovskite-type materials, and piezoelectric fibres [63,67] are being developed to date, as discussed herein.

Piezoelectric nanoparticles encompass several types, which can be classified based on their dimension (D) as 0D, 1D, 2D, and 3D materials.

Among various piezoelectric nanoparticles (PNP), 0D PNPs are gaining attention nowadays. These PNPs can be the fundamentals for making other piezoelectric nanomaterials. These nanoparticles serve as building blocks for the development of additional nanomaterials with piezoelectric capabilities, potentially providing benefits in the optical, electrical, pyroelectric, and ferroelectric domains[68]. Tian et al. developed the production of aluminium nanoparticles with a small amount of AlN, explaining the growth process in the presence of AlN nanoparticles[69]. Furthermore, it has been discovered that doping Fe into the nanoparticle matrix improves both ferroelectric and magnetic characteristics. These zero-dimensional nanoparticles are synthesized using a variety of techniques, including solvent casting and vapor-liquid-solid procedures. Wang et al. emphasized that because of their smaller size, 0D materials require a minimum carrier matrix[70]. In another work, Kaur et al. developed a simple co-precipitation approach to create 0D ZnO nanoparticles, beginning with a precursor solution comprising equal molarities of Kaur et al. developed a simple co-precipitation approach to create 0D ZnO nanoparticles, beginning with a precursor solution comprising equal molarities of hexamethylenediamine and zinc nitrate hexahydrate[71]

The one-dimensional (1D) PNPs are said to be those that have a length of more than 1 mm and a dimension of less than 100 nm [68]. One-dimensional (1D) PNs are superior to 0D PNPs, having improved charge transport facilities [72]. For the first time, the nanogenerator has been fabricated using 1D ZnO nanowires that can transform ultrasonic waves into electricity [73]. The nanowires are most commonly used for making piezoelectric harvesting devices. These nanowires are highly sensitive to minor forces, which increases the

production of electricity even with very small forces. It also has good mechanical properties as well as high polarization that provides a wonderful impact on showing the piezoelectric effect [73].
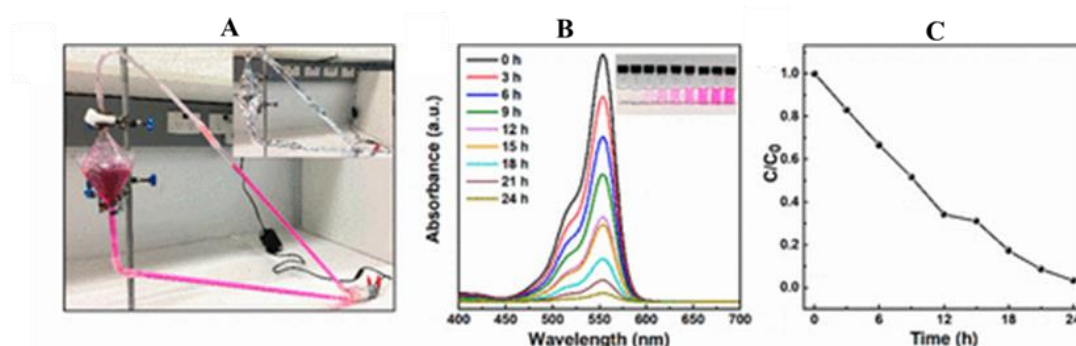
Figure 1.3 *(A) Experimental setup for degrading RhB with fixed BF–BT nanoparticles on nickel foam; a small water pump was used to spray the RhB solution on the nickel foam with piezocatalyst. The experiment was conducted in the dark as shown in the inset picture where the setup was covered with aluminum foil. (B) UV–vis absorption spectra of RhB solution upon piezodegradation by BF–BT nanoparticles under the impact of water at different times. (C) Piezodegradation of RhB with the fixed BF–BT nanoparticles under the impact of water[79]. Copyright 2024, Publisher American Chemical Society.*

Two-dimensional (2D) piezoelectric nanoparticles (PNPs) typically have nanometer-scale thickness [74]. These nanoribbons and nanofibers are transported onto flexible substrates to use the electromechanical coupling of PNPs for energy harvesting purposes. Researchers are exploring many forms of 2D PNPs, such as PZT nanofilms, PZT ribbons, P(VDF-TrFE)-alumina nanofilms, ZnO nanofilms, and BaTiO3 nanofilms[68,75]. The greater surface area exposed to the medium allows 2D PNPs to display higher catalytic actions, which aids in the removal of impurities [76]. As a result of their efficacy and diversity, nanoribbons and nanofilms are gaining importance as fundamental materials in piezoelectric and catalytic applications.

Three-dimensional piezoelectric nanoparticles (3D PNPs) are materials made up of 0D, 1D, and 2D PNPs arranged adjacent to each other, forming interfaces like piezoelectric powders and multilayer polycrystalline material, etc [68]. 3D PNPs are characterized by nano-sized grains with distinct grain boundaries but missing the surface of grains. The forces applied to 3D PNPs often result in the development of third-rank tensors, known as the coupling coefficient or piezoelectric coefficients, such as d_{13}, d_{33}, and d_{15}, depending on the direction

of pressure applied to the material [77]. Minary-Jolandan et al. conducted research into the piezoelectric effect of 3D PNPs and discovered that the piezoelectric effect of nanowires inside 3D PNPs surpasses that of bulk materials[78]. Sun et al. described experimental protocols for the use of piezoelectric nanomaterials, namely 0.7 $BiFeO_3$-0.3$BaTiO_3$ nanoparticles, for dye degradation, including degradation time and rate [Figure 1.3][79].

Piezoelectric nanoparticles offer promising possibilities for numerous applications, yet they come with notable limitations. These considerations include cost-effectiveness, stability, mechanical strength, flexibility, and biocompatibility. As a result, there has been a change in the development of polymer-based materials having piezoelectric characteristics.

Polymer-based piezoelectric materials exhibit piezoelectric properties when subjected to tension. Several families of organic polymers and biopolymers demonstrate piezoelectric effects, including fluoropolymers, polysaccharides, polyamides, polyester, polypeptides, collagen, cellulose, and silk [80]. The inherent flexibility of polymers enables them to withstand high strain, making them popular choices for piezoresponsive materials. Ramadan et al. categorized piezoelectric polymers into three groups: Bulk piezoelectric polymers, Polymer piezoelectric composites, and Voided charged polymers (or cellular polymers) [81]. Bulk piezoelectric polymers can further be divided into semicrystalline and amorphous types [82]. Semicrystalline polymer materials have a crystalline phase, and their crystallinity changes depending on the variation of preparation techniques, thermal stability, etc. Semicrystalline polymers, such as PVDF and co-polymers, poly-L-lactic acid (PLLA), and odd-numbered Nylons, have a crystalline phase that affects their piezoelectric properties [83]. The filler embedded in the polymer matrix plays a crucial role in determining piezoelectricity.Biopolymers like collagen, keratin, and silk are also utilized as piezoresponsive materials[84]. Amorphous piezopolymers, such as PVC, PAN, and PVAc, exhibit quasi-stability, and their polarization does not occur in thermal equilibrium[81]. Their glass transition temperature is a crucial indicator of the poling process. Orientational polarisation is the cause for piezoelectric behavior for this type of polymer [82].Turner et al. describes that semicrystalline polymers generally exhibit superior piezoelectric properties compared to amorphous polymers[82]. Figure 1.4 illustrates the chitosan biopolymer and clay-induced polymer, highlighting the contribution of surface charge density to polarization and subsequent piezocatalysis mechanisms.
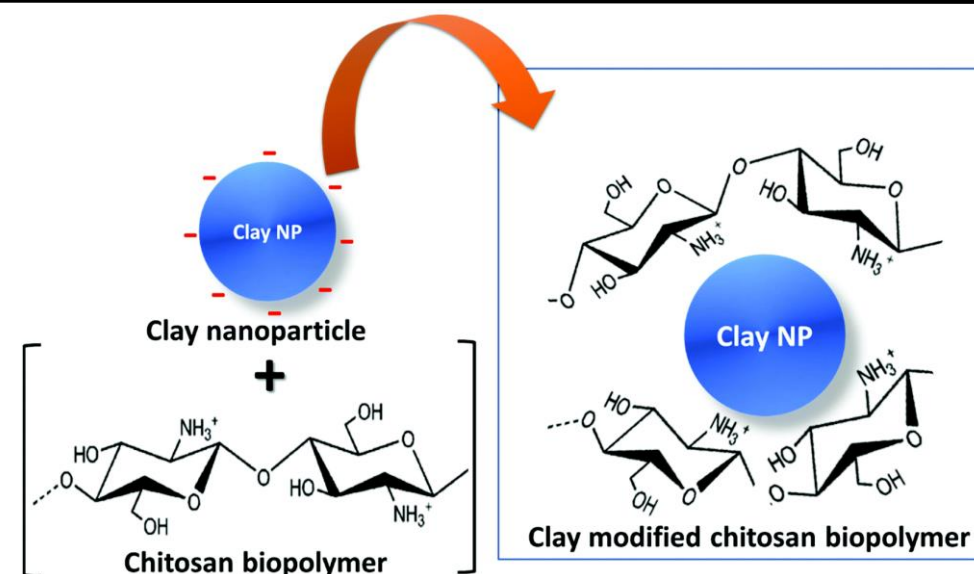
Figure 1.4 *Illustrates the clay moiety surface charge and the effect of the intercalation with chitosan biopolymer that helps in the piezocatalytic performance. [85]Copyright 2022, Publisher Royal Society of Chemistry.*

Polymer-nanocomposites are made up of a wide range of components, including ceramic and ferroelectric fillers. The increased piezo-responsiveness of these composites is dependent not only on the synthesis technique but also on the physicochemical characteristics of the filler components. As a result, it is critical to evaluate features such as electrical properties, mechanical properties, and shape before using them as fillers in the manufacture of piezoresponsive polymer nanocomposites. To enhance the piezoelectric effect, a greater volume proportion of filler materials is required and used [86]. Various ceramics and nanoparticles are inserted into polymers such as PVDF and DMSO to improve the piezoelectric characteristics of the resultant nanocomposites. Fillers are divided into metal-based, ceramic, carbon-based, and hybrid fillers [87-88]. Ceramic fillers are generally made of inorganic compounds including nonmetal, metal, and metalloid atoms [89]. To develop piezoelectric characteristics, promising piezoceramics such as sodium potassium niobate (KNN), lead zirconate titanate (PZT), bismuth sodium titanate (BNT), and barium titanate ($BaTiO_3$) are introduced into polymers [90]. Metal-based fillers, including titanium dioxide (TiO_2), ferrites, zinc oxide (ZnO), and iron oxide (Fe_3O_4), can also be used to create polymer nanocomposites with remarkable piezoelectric properties [91]. Carbon-based fillers, such as carbon nanotubes (CNT), carbon dots (C dots), and reduced graphene oxide (rGO), are being used to provide intrinsic multifunctional

characteristics [92]. Adding rGO and surface-functionalized multi-walled carbon nanotubes (MWCNT) to PVDF can improve its beta phase and dielectric characteristics. Hybrid materials, such as rGO-Fe$_3$O$_4$-ZnO, TiO$_2$- MWCNT, etc. can be synthesized as hybrid fillers for incorporation into polymers like PVDF, PDMS, or Kapton film [93]. These hybrid fillers significantly enhance the properties of the resulting polymer-nanocomposites. Figure 1.5 illustrates the mechanism of reactive oxygen species (ROS) generation and dye degradation using MWCNT-kaolinite composite-doped polymer as an example which has been explained in section 1.8.1.
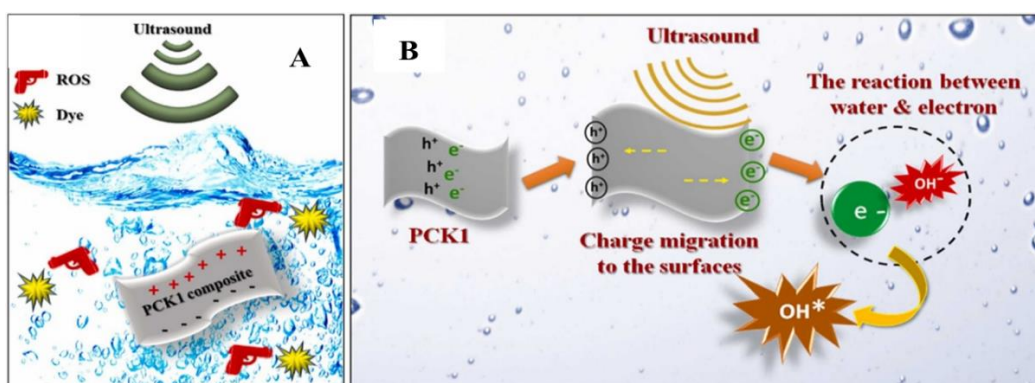
Figure 1.5 (A) Mechanism of dye degradation under ultrasound using piezoresponse membrane, (B) Mechanism of ROS production in a flexible membrane-like piezocatalyst under ultrasonic eradication. [52]

Nanofibers are fibers with dimensions ranging from 1 nanometer to 1 micrometer [94]. There are several methods for making piezoelectric fibers, including hydrothermal, sol-gel, electrospinning, and metal-organic deposition (MOD) [95]. There are three types of piezoelectric nanofibers: organic, inorganic, and hybrid. PVDF-CTFE, PVDF-TrFE, and PVDF-HFP are examples of organic fibers that are commonly synthesized using melt and wet spinning. In contrast, inorganic piezoelectric fibers have greater piezoelectric coefficients than organic fibers. Ceramic fibers are produced using techniques such as Thermoplastic Extrusion, Sol-Gel Extrusion, and Viscous Solution Spinning (VSSP). To develop piezoresponsive fibers, researchers have fabricated a variety of nanofibers. For example, Jolly Bhadra et al. used electrospinning to create polyvinylidene fluoride hexafluoropropylene (PHP) and zinc oxide (ZnO), silica, and (ZnO) composite nanofibers, highlighting the applicability of ZnO-mesoporous silica PHP nanofibers for low-powered clothing devices [96]. Furthermore, Yu et al. created a fiber substrate made of

polydimethylsiloxane (PDMS) with carbon nanotube (CNT) sheets serving as inner and outer electrodes, as well as polymethyl methacrylate (PMMA) and PDMS, resulting in a stretchable, flexible, and bendable fiber-mediated device capable of converting various mechanical stimuli into electricity [97]. Another research group synthesized piezoelectric nanofibers of lead zirconate titanate ($PbZr_{1-x}Ti_xO_3$ or PZT) using sol-gel processing and electrospinning, observing a lower elastic modulus (42.99 GPa) compared to bulk material due to the smaller grain size (10 nm) in PZT nanofibers [98]. Lee et al. described the use of MoS2/Carbon fiber-based piezocatalysts for the degradation of RhB dye [99].

As most of the pizoresponsive materials are chemically synthesized they have several difficulties such as toxicity, non-biocompatibility, and so on. Hence incorporation of naturally available material into piezoelectric polymer can not only eliminate the issues but also enhance the property of piezoelectric polymer and make them stable and flexible.

1.7.2 Mechanism of generation of piezoelectric energy

Piezoelectric energy generation is elucidated through dipolar polarization [100]. The internal rotation of polar atomic groups associated with the asymmetric carbon triggers polarization and β-phase formation in the PVDF membrane, increasing piezoelectric properties [101]. External force or stress applied to the device prompts the separation and accumulation of charges toward opposite electrodes, creating a piezo-potential that boosts polarization [102]. This potential affects electron mobility, driving electrons to flow through the external circuit. Upon release of the force, charges flow in the opposite direction, leading to the appearance of negative edges. The mechanisms is illustrated by the Figure 1.6.

In the case of finger tapping, the tapping acts as an external stimulus which is the source of applied force. When it comes to water flow, the water flow acts as an external stimulation to start the charge separation process, allowing for the production of piezoelectric energy from that water flow as well.
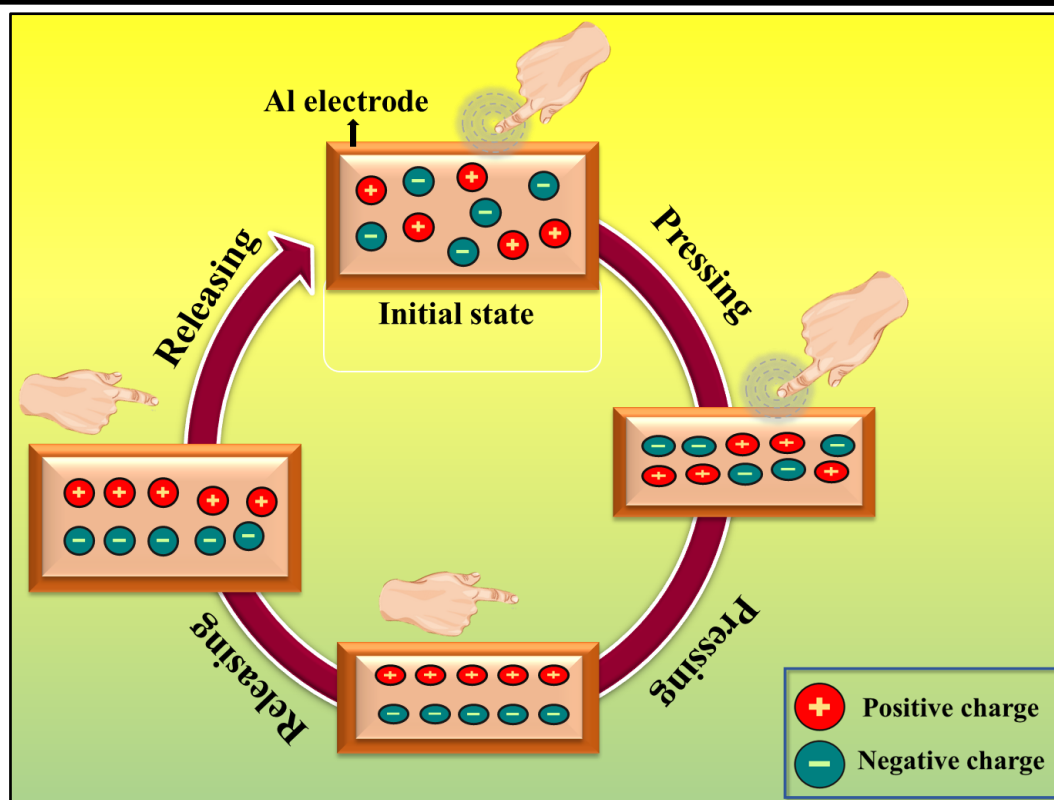
Figure 1.6 Mechanism of piezoelectric energy generation

1.8 Piezocatalysis: an emergent wastewater treatment

Nowadays piezocatalysis is a pioneering technology in the field of wastewater treatment that combines piezoelectric materials and catalysis to degrade pollutants in water [103]. This innovative method uses mechanical pressure or stress applied to certain materials to generate electrical charges. This creates reactive oxygen species (ROS)such as free radicals which in turn activate catalytic reactions that break down contaminants in water [85].

In several respects, this technology has enormous promise in efficiency, environmental friendliness, applicability, renewable energy sources, integration with nanotechnology, etc [104]. Degradation of contaminants in wastewater in water can be accelerated by the combined effects of catalysis and piezoelectricity enhancing the efficacy of degradation percentage.

As piezocatalysis usually doesn't need extra reagents or chemicals, less secondary pollution is produced. It may be used on a variety of contaminants and wastewater kinds, such as organic dye, pharmaceutical, and other contaminants. The external force or stress applied to piezoelectric materials can be generated from various waste mechanical sources, like vibrations, and motion, which makes it potentially sustainable. Nanoscale piezoelectric

materials can boost catalytic activity because of their larger surface area, which is how piezocatalysis and nanotechnology can be integrated and work together.

Piezocatalysis is a potentially effective and environmentally beneficial way to degrade contaminants in wastewater. However, further research and development are needed to refine this technology, improve its effectiveness, and make it economically viable for widespread implementation in wastewater treatment processes.

1.8.1 Mechanism of piezocatalysis

Various piezocatalysis mechanisms have been proposed by researchers. Bößl et al. introduced the concept of bulk polarisation, which can help to increase piezoelectric potential [104]. Bulk polarisation can occur in two ways: first, by increasing the polarity of each unit, and second, by crystal development in the direction of polarization, as proposed by Tu et al [105]. Under external stress, charge separation occurs between the material's surfaces, resulting in the formation of a piezoelectric potential. This phenomenon generates reactive oxygen species (ROS)-like superoxide and hydroxyl radicals via redox reactions. Superoxide radicals are created when negative charges (e^-) combine with dissolved oxygen, whereas positive charges yield hydroxyl radicals [106].

$$\text{Oxidation: } OH^- + h^+ \rightarrow \bullet OH \qquad (1.1)$$

$$\text{Reduction: } O_2 + e^- \rightarrow \bullet O_2^- \qquad (1.2)$$

Piezocatalytic processes are normally carried out under ultrasonication, with two types of forces—vertical and horizontal—causing deformation such as bending or compression [107]. This deformation alters the charge distribution, causing it to move toward the surface as both the conduction and valence bands become inclined. As a result, both electrons (e^-) and holes (h^+) travel to the opposite surface, resulting in the development of a piezoelectric potential during ultrasonication [Figure 1.7],. This piezoelectric potential begins the redox process, which produces reactive oxygen species (ROS) such as hydroxyl radicals ($\bullet OH$) and superoxide ions ($\bullet O^{2-}$). Two potential techniques have also been mentioned for the piezocatalysis process in the breakdown of organic dye [108]. First, acoustic waves create potential differences, and then the generation of electron-hole pairs due to shock waves created by ultrasonication.

Although these two mechanisms are interrelated to each other, initializing the formation of ROS [Figure 1.7], enhances the process of degradation of organic dye.

$$Material + ultrasonic\ sound \rightarrow\ e^- + h^+ \tag{1.3}$$

$$H_2O + h^+ \rightarrow H^+ + \bullet OH \tag{1.4}$$

$$O_2 + e^- \rightarrow \bullet O_2^- \tag{1.5}$$

$$e^- / h^+ / \bullet OH / \bullet O_2^- + organic\ dye \rightarrow degradation\ of\ dye \tag{1.6}$$
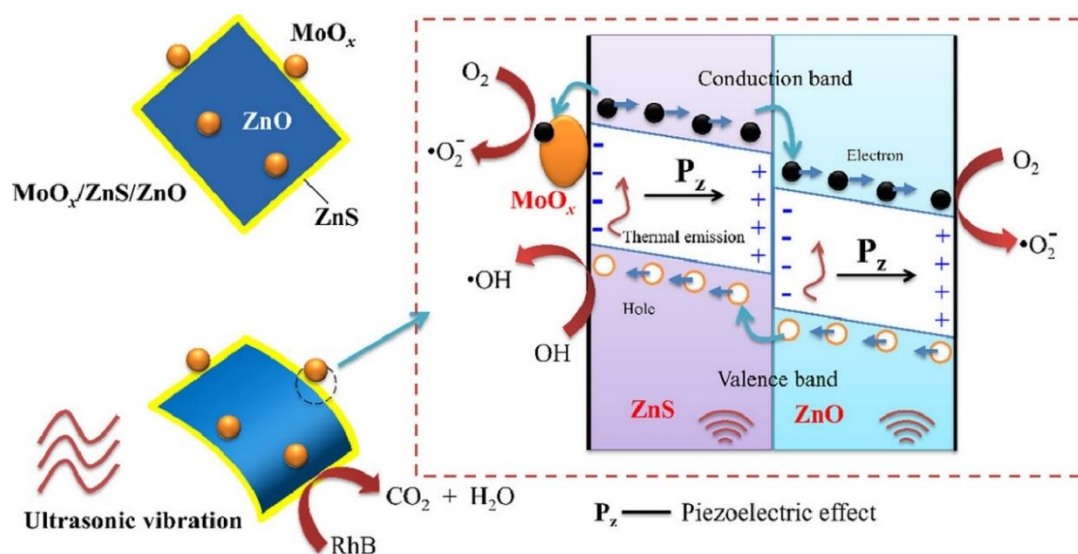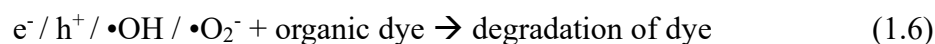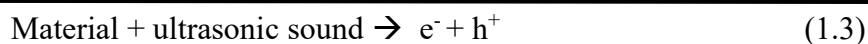
Figure 1.7 *Schematic representation of reactive oxygen species (ROS) production under ultrasound using MoOx/ZnS/ZnO composite.[110] Reprinted from Elsevier, Copyright 2024.*

The formation of reactive oxygen species (ROS) has been confirmed through an experiment known as the scavengers experiment. In this experiment, various materials are used to selectively remove or "scavenge" different types of ROS. Ethylenediaminetetraacetic acid (EDTA), tertbutanol (TBA), silver nitrate ($AgNO_3$), and p-benzoquinone (BQ) are utilized as scavengers for ROS formation like hole (h^+), electron (e^-), hydroxyl radicals and superoxides radicals respectively [111]. During ultrasonic vibration, the degradation process is slowed for the ROS associated with the particular scavenger supplied. For example, if the addition of BQ causes the most significant delay in dye degradation compared to the other scavengers, it suggests that superoxide radicals are the dominant reactive species responsible for dye decomposition in that particular system [Figure 1.8].
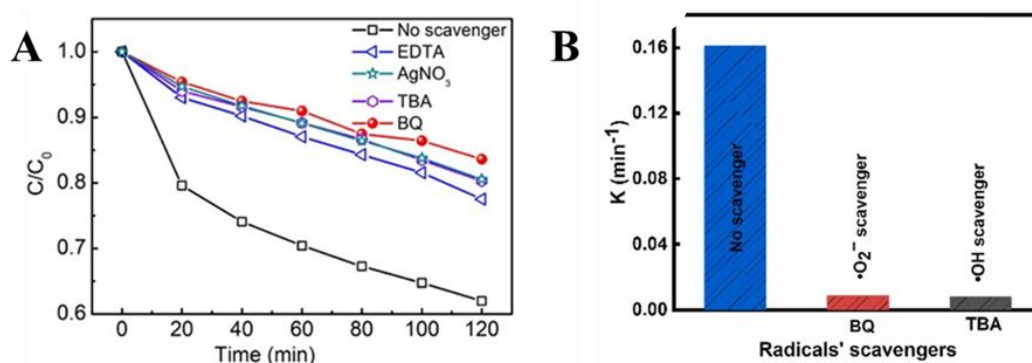
***Figure 1.8** (A) The degradation of MB dye by piezocatalysis using ZnO nanorods in the presence of electrons, holes, hydroxyl radicals, and superoxide radicals, (B) Rate constants for reactions using various radical scavengers, [112,113] Copyright 2020, Publisher Elsevier. Copyright 2024, Publisher Elsevier*

There can be two theories behind the mechanisms of piezocatalysis, as suggested by Wang et al. (2022) [114]. These are energy band theory and screening charge effect.

Energy Band Theory originates from photocatalysis [115]. Nonetheless, there are major distinctions among them, such as variances in excitation techniques and charge carriers. In piezocatalysis, mechanical stimuli are used to generate charge carriers. Mechanical stimulation, such as ultrasonic vibration, causes electrons to be elevated from the valence band (VB) to the conduction band (CB). Ultrasonic stimulation generates high pressure, roughly 108 Pa, at the interface of water and catalyst due to bubble collapse induced by ultrasonication [116]. Figure 1.8 shows another technique of indirectly creating electron-hole pairs: vibration-induced thermal excitation. The collapse and subsequent release of energy during ultrasonic activity create localized "hot spots" around the piezoelectric material, and the associated high temperatures frequently play a critical role in electron excitation [117,118].

Free charges are also generated from defects, with electrons migrating to the surface due to the piezo-potential, facilitating the formation of reactive oxygen species (ROS) responsible for degrading organic pollutants like MO dye, RhB dye, etc [119]. This migration tilts the conduction and valence bands in the space-charge layer towards the subsurface, resulting in an electric potential gradient due to discontinuities in the electronic state at the interface and facilitating carrier transfer. The piezoelectric potential is vital in modulating the band

structure since the degree of band bending is proportional to the piezo-potential. The ability to separate charge carriers through polarization-driven forces is also significant in piezocatalysis. The piezo-potential effectively affects charge separation and transportation behaviour by acting as the driving force that separates charge carriers, such as electron-hole pairs [Figure 1.7] [114]. Electron-hole pairs, whether generated by mechanical force or defects, migrate towards opposite surfaces of the piezoelectric material due to electrostatic interaction. The piezo-potential is a critical tool for charge separation and band structure alteration, which are required for piezocatalysis. By regulating the band levels, the piezo-potential creates thermodynamically favorable circumstances for initiating redox reactions, allowing charge to migrate to both catalyst surfaces. Faradic and capacitive routes contribute to the depletion of charges towards the surface [114]. Energized charges transported from the surface to the electrolyte cause chemical processes that produce Faradaic current. Alternatively, for piezopotential screening, double layers form at the catalyst surface due to capacitive current. Even within a single straining cycle, atom migration can occur through both Faradic and capacitive currents. Thus, periodic mechanical energy is required for piezocatalysis processes [120], as it ensures the continual generation of piezoelectric potential to energize charge carriers and trigger chemical reactions. The reaction rate may also depend on the frequency of transonic vibration, providing a consistent mechanical force source. Additionally, the duration of force application can significantly impact the catalysis process; insufficient time between consecutive strains may hinder electron-hole pair creation or movement to the opposite surface, thereby impeding catalytic activity [121]. Hence, the development of piezo-potential holds significant importance, facilitating charge carrier movement to initiate redox reactions and stimulate the piezocatalysis process.

Wu et al. [122] proposed that inherent charges inside piezoelectric materials have a major impact on charge transfer during piezocatalysis by altering charge carrier concentrations. Mechanical stimulation, or pressure, increases piezoelectric polarisation inside these materials, causing free electrons and holes to flow in opposing directions along the crystal surface. This instantaneous movement bends the valence and conduction bands due to the piezoelectric potential, with the slope proportional to the potential magnitude. As a result, increased piezoelectric potential promotes quicker electron and hole reactions with dissolved oxygen, resulting in the aforementioned redox states. Polarisation charges reduce the driving force for charge transfer, but the buildup of screen charges creates an electrical field strong enough to offset the polarisation field, resulting in a potential equilibrium that

inhibits redox processes. Reduced polarisation with decreasing pressure disrupts the equilibrium, resulting in additional redox processes via reverse charge transfer. As the surface charge decreases, redox processes at the liquid-solid interface become unsustainable. Thermal emission from absorbed ultrasonic vibrations can replenish expended free charges, hence continuing the redox process. Ultrasonic vibrations provide high-frequency stress-strain, which allows for the fast buildup of redox reaction products even at low free charge concentrations.

In the case of the screening charge effect, surface screening behavior in piezo materials plays a significant role, which is related to piezo potential. The polarization of the piezo material affects the surface electrical characteristics.

Zhang et al. [123] have shown that both piezoelectric and pyroelectric polarisation contribute to the dynamic screening of surface charges. However, the commencement of this dynamic process varies across piezoelectric and pyroelectric polarisations. External mechanical forces induce stress in piezoelectric materials, causing space screening charges to migrate to the opposite pole. The polarisation amplitude decreases with stress release, resulting in the release of space screening charges. These released charges can flow across an external circuit, resulting in potential differences or voltage in open circuits and current in short circuits. Figure 1.9 depicts the working principle of the screening charge effect, portraying the interaction between a piezoelectric material and external screening charges during polarization and depolarization processes. In its electrically neutral state (State 1), bound charges of materials caused by polarisation are balanced by external screening charges on its polar surfaces. External stress, such as ultrasonication, disrupts this equilibrium, decreasing polarisation and allowing extra screening charges to be released from the surface (State 2). These free charges encourage redox reactions with numerous substrates at the surface of the material, resulting in a new electrical equilibrium (State 3). Once the tension is eliminated, polarization is restored, and polarization-bound charges are formed. Space charges in the electrolyte are adsorbed on the surface, allowing the opposite polar charges of electrolytes to participate in the process (State 4). Thus, screening charge phenomena are facilitated by the change in piezoelectric and pyroelectric polarization effects [124,125]. In this type, piezo-potential directly triggers the reaction to start by energizing the carrier, and the magnitude of piezo-potential is to be equal to or more than the potential of a redox reaction to begin the chemical process and degrade the organic contaminants. Hence, piezo-potential acts as the key factor in the theory of screening charge

effects. Here, the released screening charges are the source of the charge carriers starting the redox reactions.
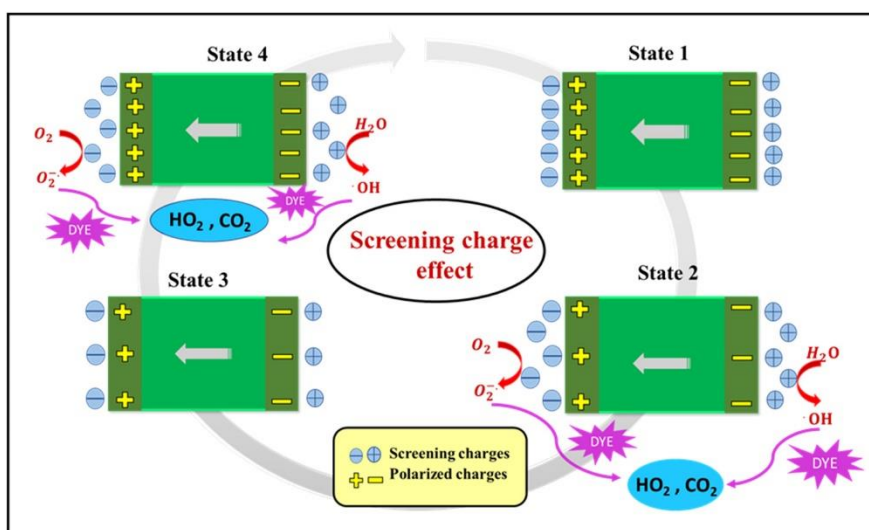
Figure 1.9 *Schematic illustration of the mechanism of piezocatalysis based on the screening charge effect [124].*

1.9 Outline of the present work

1.9.1 Origin of the problem

Summertime power outages are a problem that many people frequently experience. These interruptions are caused by several factors. High temperatures lead to increased demand for electricity as people use air conditioners and cooling systems to combat the heat. This surge in demand can strain the power grid, especially if the infrastructure is not equipped to handle the peak load. Furthermore, high temperatures can reduce the effectiveness of electricity transmission and generating systems, which might result in malfunctions and blackouts.

Along with this, water pollution is another great concern nowadays. An increase in industrial activity throughout the world contributes to the issue by releasing contaminants into water bodies. Water quality problems are further exacerbated by fertilizer and pesticide-filled agricultural runoff and increased surface runoff brought on by urbanization. In addition, untreated household water is another cause of contamination in waterways. Inadequate wastewater treatment infrastructure, population growth, and the insufficient development of treatment facilities result in untreated sewage entering water bodies.

From that point on, the goal was to address both problems simultaneously with cost-effective and widely available multifunctional materials easily and economically.

1.9.2 Aims and objectives

Addressing the two burning global issues, such as the energy crisis and water pollution, that are continuously faced by the entire world, nanotechnology has paved various paths to get rid of these problems among these piezo-responsive energy generation and wastewater treatment gained interest in the last few decades which has been illustrated in section 1.6. Over time various piezo-responsive materials developed by the researchers. Initially, chemically derived nanomaterials show higher efficiency. But their low biocompatibility and secondary toxicity effect push them back. Thus, researchers are focusing their interest on natural nanomaterial-based polymeric systems for these dual problems but that are in their infancy. This work involves the fabrication of a device with a low-cost, abundant, reusable, flexible natural hematite-mediated membrane capable of harvesting energy using several mechanical sources like finger tapping, water flow, wind flow, and so on. The membrane can also degrade the carcinogenic dye like RhB by piezocatalysis mechanism. The efficiency and performance have been enhanced by introducing and varying dopants like rare-earth material, MWCNT into the hematite. This is how the hematite-membrane-based device can be a cost-effective inventive solution to both energy problems and water pollution.

 Therefore, the plan of the research work to eliminate the energy crisis problem as well as remediation of wastewater with a lucrative solution is elaborately described in the points below:

- The selection of material that is abundant in nature and has good surface properties, electrical properties, etc.
- Nanonization of the natural material to gain a high aspect ratio and surface properties by a simple one-step top-down mechanism.
- Complete Characterization and analysis of the synthesized materials for further progress.
- Study of the physicochemical properties and use it for further application
- Synthesis of polymer (PVDF-HFP) nanocomposite films in a simple solution casting method.

- Incorporation of various foreign materials (such as rare earth material, MWCNT) into natural hematite (α-Fe_2O_3) for optimization of surface properties and incorporate them into the polymer (PVDF-HFP) to fabricate nanocomposite film for enhancing the piezo-properties of the material.

- Details study of the properties of the PVDF composite film and also determine the modification of the β phase of composite by varying the filler materials.

- Composite membrane-based device fabrication to harvest electrical energy from several sources like finger/hand tapping, flow of water, wind flow, etc.

- Use the piezoresponsive composite film for the decomposition of contaminants like organic dye from water by piezocatalysis.

1.9.3 Selection of nanomaterials

Recently, the synthesis of nanoparticles has drawn the interest of many researchers. Studies and explorations about nanoparticles unveil a vast domain of scientific and technological innovation. Producing nanoparticles and examining their characteristics include a wide range of applications to succeed in many domains. Researchers are interested in investigating the features of these nanoparticles because of their exceptional physicochemical properties, which explain many applications ranging from the realm of biology to electronics.

Various types of materials are used for the development of piezoelectric materials. Materials can be divided into piezoelectric nanoparticles, piezoelectric polymers, and piezoelectric fibers. Xue-Qian Fang et. al. classified piezoelectric nano particles in 0D, 1D, 2D, and 3D materials [107]. $BiFeO_3$, $BaTiO_3$ as 0D, ZnO nanowires as 1D, $BaTiO_3$ nanofilms as 2D, and $BaTiO_3$ as 3D materials have been used as piezoelectric materials [107]. There are lots of piezo-electric polymers like PVDF, PVC, poly-L-lactic acid (PLLA), cellulose, collagen, etc. All of these polymers are used for piezoelectric energy harvesting purposes. Despite their increasing significance, chemically produced nanoparticles may have drawbacks in terms of cost-effectiveness and toxicity that harm the biota. Henceforth, scientists are concentrating on employing natural materials since they are biocompatible, environmentally benign, and abundant in our surroundings. Therefore, selecting a substance with minimal toxicity and abundance in nature is convenient. The development of inexpensive, widely available electronics and solid-state devices that have the potential to be future technologies is also prioritized. One of these ubiquitous minerals that is found in the environment is α-

hematite (α-Fe$_2$O$_3$). Nature has large levels of hematite, which is both biocompatible and nontoxic. Its magnetic, optical, and electrical qualities are superb. These characteristics can be applied in several fields. Numerous domains, including biological, electrical, and sensing applications, are potential uses for hematite nanoparticles. In short, the following characteristics of α-Fe$_2$O$_3$ have been used to employ it in this work

- biocompatibility
- non-toxicity
- high surface area (21.69 m^2/g)
- porosity (3.681 nm)
- thermal stability (up to 400 ºC)
- cost-effectiveness
- widely available in nature.

Despite the well-established structure of the material and numerous production methods, the use of the naturally available α-Fe$_2$O$_3$ in energy harvesting as well as wastewater treatment is still unexplored. It would undoubtedly open up new possibilities to modify α-Fe$_2$O$_3$ with rare earth materials, carbon nanotubes, polymers, etc. to increase its efficacy towards multifunctional wastewater remediation and energy harvesting strategy.

1.9.4 Organization of the Thesis
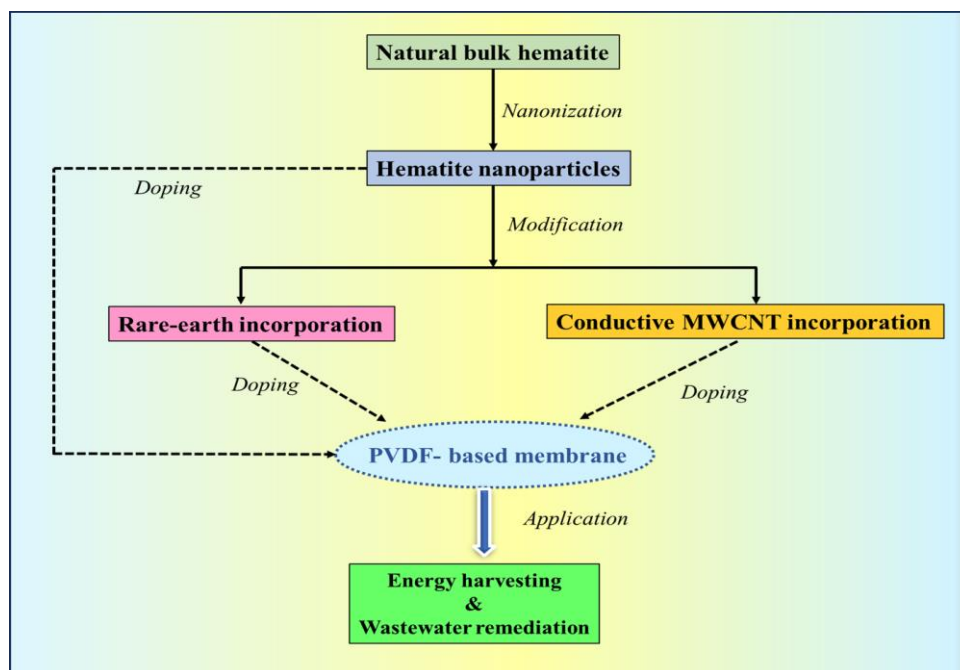
Figure 1.10 *Flowchart of the thesis organization*

Chapter 1:

Introduction and methodology

Chapter 2:

Study of physicochemical properties of α-hematite due to size fractionation

Chapter 3:

Dye degradation and piezoelectric energy harvesting from hand tapping and water droplets using natural hematite-based self-poled piezo-responsive membrane

Chapter 4:

Water flow and finger-tapping mediated piezoelectric energy generation and carcinogenic dye degradation using a Gd-incorporated natural hematite-based flexible PVDF-HFP membrane

Chapter 5:

MWCNT Intercalated Natural Hematite-based Activable Nanocomposite for Piezoelectric Energy Generation and ROS-Mediated Carcinogenic Dye Degradation

Chapter 6:

Conclusion & Outlooks

1.10 Methodology

1.10.1 Synthesis procedure of natural α-hematite nanocrystal

The natural hematite rock was first cleaned with water to get rid of any waste and contaminants before physically disintegrating into a finer fraction. By using a Fritz Planetary Mono Mill Pulverisette 6 and grinding hematite for 12 hours at 100 rpm, nano-sized hematite was produced. Ball-milling is usually carried out with tungsten carbide balls sampled at a mass ratio of 20:1.10 balls with a diameter of 9.99 mm and a weight of 7.5 gm, and in this instance, 25 balls with a diameter of 4.88 mm and a weight of 1 gm were used to maintain the ball-to-sample ratio. To get the final hematite nanoparticles for the studies, acetone was used for washing and then manually crushed in an agate mortar. The characteristics of the material can be improved by doping the hematite into the polymer or incorporating foreign components into the hematite during the production process. Nonetheless, even a little fluctuation in the concentration % might alter the physicochemical characteristics.

1.11 Characterization procedure

The nanoparticles of natural hematite (α-Fe_2O_3) have been characterized for studying the physical, chemical, thermal, etc. properties of materials by several techniques described below:

1.11.1 Morphological, structural, and elemental characterizations

One of the most used analytical methods is X-ray diffraction (XRD), which is particularly useful for identifying crystalline materials and yielding certain unit cell dimensions [126]. The substance under analysis is crushed to a fine consistency, then the bulk composition is averaged out. These days, XRD is a widely used method for analyzing crystal structure and atomic spacing. Bragg's law forms the basis of the operation of X-ray diffractometers. XRD has been employed in our study to identify the microstructural parameters, crystallite size, peak purity, etc. X-ray diffraction (XRD) was performed by using a D8, Bruker AXS X-ray diffractometer [Figure 1.11] to identify the phase and microstructure of the materials with a Cu-Kα target by varying the angle of incidence, the range of 2θ being 20˚ to 70˚.

The diffraction maxima for α-Fe_2O_3 obtained from X-ray diffraction (XRD) are matched with the JCPDS (Joint Committee on Powder Diffraction Standards) card number to verify

the purity of the sample. The size of the crystallite can be determined using the Debye-Scherer equation

$$<D>_{121} = 0.9\lambda/(\beta_{1/2}\cos\Theta) \qquad (1.7)$$

Where D is the size of the crystallite, λ is the wavelength of the incident X-ray beam, Θ denotes the Bragg's angle, and $\beta_{1/2}$ is the full width of the peak at half maximum. However, additional microstructural characteristics cannot be estimated using this equation. As a result, Rietveld refinement has been used to thoroughly analyse the microstructural characteristics. Using the MAUD (Material Analysis Diffraction) v2.94 software programme, Rietveld refinement has been carried out to look at the physicochemical characteristics and the microstructural. The experimental diffractograms have been refined using a standard cif file (crystallographic information file. The Caglioti PV function and Gaussian broadening are mostly used for calibration, along with background parameter optimization. It is found that several microstructural parameters, including as cell dimension, crystal size, and microstrain, are improved and that the experimental diffractogram is well-fitted with promising fitting coefficients over the theoretical data. The VESTA (Visualisation for Electronic and Structural Analysis) program v3.5.2 has been used to visualize the bonding networks and microstructures of the unit cell. Hence the unit cell parameters, structure, bond length, bond angle have been explored in this thesis through refinement. Hence, the XRD and refinement technique has been employed in our research work to investigate purity, crystallinity, lattice parameters etc.

Figure 1.11 *X-ray diffractometer (XRD) facility of the Department of Physics,*
Jadavpur University

To reveal the morphological and structural parameters field emission scanning electron microscope (FESEM)/ transmission electron microscope (TEM) has been employed. In FESEM, Carbon grids were covered with small quantities of the samples to analyze the microstructures at accelerating voltage ranges of 10 kV to 20 kV [127]. Then the sample was gold-coated by sputtering to resist the accumulation charges throughout the experiment. Then it was examined by Field emission scanning electron microscopy (FESEM) Inspect50 (FEI, Netherlands) to understand the morphology of the materials [Figure 1.12]. A JEM-2100 Plus transmission electron microscope (TEM) was used, running at 200 kV, to get a closer look [128]. Prior to the experiment, the samples on the carbon-coated copper grids were put straight into the device while it was operating at a high vacuum. The ImageJ program (v1.52p) was utilized for further analysis of both FESEM and TEM micrographs to determine the particle sizes. Thus, SEM and TEM were used in this study to determine the form, size, morphological characteristics, and microstructural parameters.

Figure 1.12 *Field Emission Scanning Electron Microscope (FESEM) facility of the Department of Physics, Jadavpur University*

To verify the purity of the sample by identifying its elemental components, energy dispersive X-ray spectroscopy (EDS) using a Supra 55 (ZEISS) connected to the FESEM was carried out [127]. Elements mapping was carried out similarly in some of our research, demonstrating greater agreement with other properties of the as-prepared samples.

Fourier transforms infrared (FTIR) spectroscopy was used to analyze the materials' bonding networks, purity, and β-phase nucleation in the required wavenumber range [129]. Samples are analyzed using FTIR specotroscopy (IR Affinity, Shimadzu) [Figure 1.13]. The primary goal of employing FTIR is to find the functional groups in the sample, as well as the bond type, structure, and bonding network of the testing sample. The purity, bonding network, and β-phase nucleation of the material have been studied using FTIR by varying the frequency from 400 and 4000 cm^{-1}. The fraction of electroactive β-phase has been calculated from the Lambert-Beer law [130],

$$F(\beta) = \frac{A_\beta \times 100}{\left\{ \left(\frac{K_\beta}{K_\alpha} \right) A_\alpha + A_\beta \right\}} \qquad (1.8)$$

Where, A_α, and A_β are intensities of absorbance at 765 cm^{-1} and 840 cm^{-1} respectively, absorption coefficients $K_\beta = 7.7 \times 10^4$ cm^2 mol^{-1} at 845 cm^{-1} and $K_\alpha = 6.1 \times 10^4$ cm^2 mol^{-1} at 765 cm^{-1}.
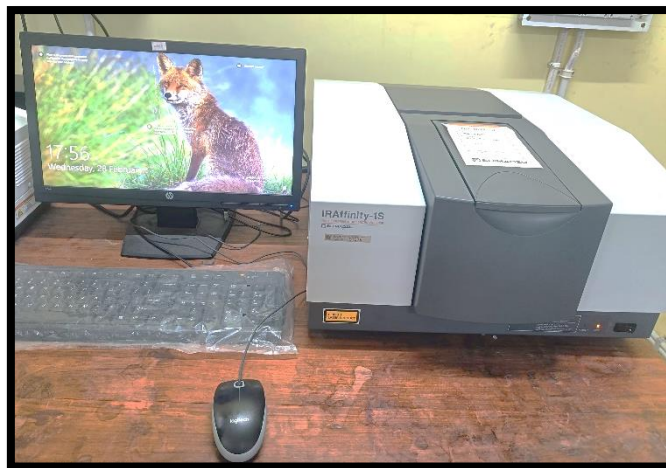
Figure 1.13 *Fourier Transform Infrared Spectroscopy (FTIR) facility of the Department of Physics, Jadavpur University*

One method often used to ascertain the elemental composition of any material is X-ray fluorescence (XRF) [131]. To ascertain the elemental composition and purity of the synthesized materials, the X-ray fluorescence (XRF) spectra were examined using an Axios, PANalytical X-ray Fluorescence Spectrometer [Figure 1.14]. In our study, the XRF data illustrates the elemental composition and also validates whether the natural Fe_2O_3 is mixed with undesirable impurities such as Na_2O, MgO, Al_2O_3, SiO_2, etc.

Another vital tool used in colloid and nanoparticle research is the zeta analyzer which measures the zeta potential and electrophoretic mobility of particles floating in a liquid [132]. The Zeta analyzer offers information on the stability and surface charge of colloidal systems by introducing an electric field into the solution and tracking the motion of the particles. This knowledge is essential for optimizing formulations, evaluating product stability, and comprehending particle interactions in a variety of sectors, including food, cosmetics, and medicines. To investigate the surface charge of the hematite nanoparticles zeta potential has been measured in our study using a Zetasizer, 167 Malvern, the hematite powder was well-dispersed in distilled water (1 mg mL^{-1}) with the use of an ultrasonic bath.

Figure 1.14 *X-ray Fluorescence (XRF) facility of the Materials Characterization and Instrumentation Division, CSIR-Central Glass & Ceramic Research Institute*

1.11.2 Study of surface area and pore distribution

The pore size distribution and surface area of nanoparticles were investigated using the Brunauer–Emmett–Teller (BET) and Barrer–Joyner–Halenda (BJH) procedures (using a Twin Surface Area Analyzer from Quanta-chrome Instruments, USA) utilizing N_2 gas adsorption-desorption [133]. This has been introduced in our study to know the types of porosity, nature of isotherm, and pore size of the hematite nanoparticles.

1.11.3 Thermal stability

The thermal stability of the samples was estimated by using thermogravimetric analysis (TGA), which measures the percentage of mass loss as a function of temperature [134]. A consistent heating rate of 10°C/min was applied to the synthesized samples while they were subjected to temperature variations ranging from 30°C to 400°C.

Differential thermal analysis (DTA) has been employed to determine the heat transfer phenomena [135]. The results of the TGA data are in good agreement with the thermographs

produced by the samples' differential thermal analysis (DTA), which demonstrates whether the

Figure 1.15 *Differential Thermal Analysis (DTA) facility of the Department of Physics, Jadavpur University*

Both the thermogravimetric (TGA) analysis and differential thermal analysis (DTA) are carried out between 10 and 150 ◦C in a nitrogen environment at a heating rate of 10 ◦C min^{-1}, with the samples placed in platinum crucibles, using a DTG-60H, Shimadzu [Figure 1.15]. Thus, DTA and TGA analysis is performed to determine the thermal stability of the hematite nanoparticles as well as the hematite-based membrane.

1.11.4 Optical properties analysis

The advanced technique known as absorption spectroscopy or reflectance spectroscopy in the ultraviolet-visible spectral range is called ultraviolet-visible spectroscopy, or UV-Vis [136]. It is used to determine the absorbance wavelength of the sample and may also be used to calculate the band gap using the beer-Lambert equation. A Lambda 25 PerkinElmer UV-visible spectrophotometer was used to record the absorbance spectra of the sample [Figure 1.16].. The way the device works is by passing a light beam through a sample and measuring the wavelength of light that reaches a detector. The wavelength provides important details on the chemical structure, whereas the intensity is a measure of the amount or concentration

that is correlated with the number of molecules. Analytical data can be presented in terms of absorbance and transmittance.

Figure 1.16 *UV-Visible Spectrophotometer facility of the Department of Physics,*
Jadavpur University

Furthermore, the fluorescence spectra of the samples have been examined using an Agilent Cary Single Cell Peltier Accessory fitted with a fluorescence spectrometer [Figure 1.17]. An effective optical technique for examining the electrical structure of materials is photoluminescence spectroscopy [137], which is contactless, adaptable, nondestructive, and strong. In a process known as photo-excitation, light is focused onto a sample, where it is absorbed and transfers extra energy into the substance. Luminescence, or the emission of light, is one method the sample might release this extra energy. This luminescence under photo-excitation conditions is referred to as photoluminescence. Photoluminescence, then, is the spontaneous release of light from a substance when it is optically excited. It is possible to gather and analyze this light in terms of spectrum, spatial, and temporal dimensions.

Figure 1.17 *Photoluminescence Spectroscopy (PL) facility of the Department of Physics, Jadavpur University*

1.11.5 Electrical properties analysis

The ability of a sample to retain charge carriers is determined by its dielectric characteristics. The combined dielectric constant and tangent loss represent the ability of the material to store energy [138].

Examining the temperature-dependent dielectric property of a sample is crucial to determining the efficacy of material in energy storage devices operating within the required temperature range. The dielectric permittivity of a material is dependent on several variables, including temperature, structure of the material, and the frequency of the applied electric field. The frequency of the applied electric field, temperature, and the structure of the material are some of the variables that affect the dielectric permittivity of the material. The equation stated below represents the dielectric constant or permittivity of a sample [139],

$$\varepsilon = \varepsilon' + j\varepsilon'' \tag{1.9}$$

Where the real (ε') and imaginary (ε'') components of the relative dielectric constant, correspond to the ability of material to dissipate energy inside itself and retain energy as a result of polarisation, respectively. The relation used for calculating the real part of the dielectric constant is shown below,

$$\varepsilon' = (C \cdot d)/(\varepsilon_0 A) \tag{1.10}$$

where, C, d, and A are the capacitance, thickness, and area of the capacitor made with the sample and ε_0 is the permittivity of the free space (8.85×10^{-12} F/m). From Jonscher's universal power law, the relation between ac conductivity (σ_{ac}) and frequency can be written as [139],

$$\sigma_{ac} = B\omega^n \tag{1.11}$$

where B and n are constants. B has the unit of conductivity and n is dimensionless. The value of 'n', was obtained by plotting $\ln\sigma$ vs $\ln\omega$ curve for each sample. The electrical characteristics of a material are determined by its grain and grain boundaries, particularly in terms of tangent loss and dielectric permittivity.

An Agilent 4294A Precision Impedance Analyzer operating in the 40 MHz to 10 MHz frequency range and with an external bias voltage of 0.5 V was used to investigate the electrical characteristics and dielectric properties [Figure 1.18]. The dielectric characteristics and ac conductivities at various temperature settings were investigated using powder samples in the form of pellets with a diameter of 1 mm whereas in the case of membrane or film, it has been cut into 2x2 cm^2 and then electrical contacts are made with aluminum tape.

Figure 1.18 LCR meter facility of the Department of Physics, Jadavpur University

A digital oscilloscope is a multipurpose electronic device that is extensively utilized in engineering, electronics, and telecommunications to observe and evaluate electrical waveforms [140]. It is an essential tool for signal analysis, including features like voltage variation, frequency measurement, waveform visualization, time domain analysis, etc. A

multimeter system, the Keithley DAQ6510, was used to measure the short circuit currents of the same device [Figure 1.20]. The digital oscilloscope Agilent (N2862B 10: 1 passive probe) has been used to measure the open circuit voltage of the device constructed with the sample incorporated membrane [Figure 1.21].

Figure 1.19 *Digital Storage Oscilloscope (DSO) facility of the Department of Physics, Jadavpur University*

Figure 1.20 *Data Acquisition/ Multimeter System facility of the Department of Physics, Jadavpur University*

1.12 Summary

This thesis explores the process of modification of natural α-hematite (bulk) to nano form and the formation of the nanocomposite by incorporating rare earth elements as well as conducting MWCNT. The α-hematite NPs as well as their nanocomposite have gone through several characterization procedures such as XRD, SEM, TEM, FTIR, DTA-TGA, etc. By analyzing their physicochemical, surface, and electrical properties, these NPs and nanocomposites are utilized to construct free-standing, flexible polymeric membranes by using PVDF-HFP which have also been characterized with the characterization techniques mentioned previously to know the structural, electrical, and piezo-responsive properties to select the best membrane to harvest energy from waste mechanical energy sources and also to degrade carcinogenic organic dye like RhB. Therefore, this thesis has the potential to have a substantial influence on water technology as well as energy management by proving the feasibility of employing biocompatible nanocomposite materials for both wastewater purification and energy generation.

References

[1] Smith, D.A., 2017. Globalizing social problems: An agenda for the twenty-first century. *Social Problems*, *64*(1), pp.1-13.

[2] Karri, R.R., Ravindran, G. and Dehghani, M.H., 2021. Wastewater—sources, toxicity, and their consequences to human health. In *Soft computing techniques in solid waste and wastewater management* (pp. 3-33). Elsevier.

[3] Zoungrana, A. and Çakmakci, M., 2021. From non-renewable energy to renewable by harvesting salinity gradient power by reverse electrodialysis: A review. *International Journal of Energy Research*, *45*(3), pp.3495-3522.

[4] Burns, M.G., 2019. *Managing energy security: an all hazards approach to critical infrastructure*. Routledge.

[5] Kabeyi, M.J.B. and Olanrewaju, O.A., 2022. Sustainable energy transition for renewable and low carbon grid electricity generation and supply. Frontiers in Energy research, 9.

[6] Madhav, S., Ahamad, A., Singh, A.K., Kushawaha, J., Chauhan, J.S., Sharma, S. and Singh, P., 2020. Water pollutants: sources and impact on the environment and human health. *Sensors in water pollutants monitoring: Role of material*, pp.43-62.

[7] Ogidi, O.I. and Akpan, U.M., 2022. Aquatic biodiversity loss: impacts of pollution and anthropogenic activities and strategies for conservation. In *Biodiversity in Africa: potentials, threats and conservation* (pp. 421-448). Singapore: Springer Nature Singapore.

[8] Kapoor, D. and Singh, M.P., 2021. Heavy metal contamination in water and its possible sources. In *Heavy metals in the environment* (pp. 179-189). Elsevier.

[9] Jawad, L.A., 2021. The effects of thermal pollution on the aquatic life in the southern marshes of Iraq. In *Southern Iraq's Marshes: Their Environment and Conservation* (pp. 559-571). Cham: Springer International Publishing.

[10] Oelkers, E.H., Hering, J.G. and Zhu, C., 2011. Water: is there a global crisis?. Elements, 7(3), pp.157-162.

[11] Cosgrove, W.J. and Loucks, D.P., 2015. Water management: Current and future challenges and research directions. *Water Resources Research*, *51*(6), pp.4823-4839.

[12] Mathur, R., Chand, S. and Tezuka, T., 2003. Optimal use of coal for power generation in India. *Energy policy*, *31*(4), pp.319-331.

[13] Sen, S., Ganguly, S., Das, A., Sen, J. and Dey, S., 2016. Renewable energy scenario in India: Opportunities and challenges. *Journal of African Earth Sciences*, *122*, pp.25-31.

[14] Gould, C.F. and Urpelainen, J., 2018. LPG as a clean cooking fuel: Adoption, use, and impact in rural India. *Energy Policy*, *122*, pp.395-408.

[15] Majid, M., 2020. Renewable energy for sustainable development in India: current status, future prospects, challenges, employment, and investment opportunities. *Energy, Sustainability and Society*, *10*(1), pp.1-36.

[16] Khan, Ahmed Shabbir, Ankur Anavkar, Ahmad Ali, Nimisha Patel, and Hina Alim. "A review on current status of riverine pollution in India." *Biosciences Biotechnology Research Asia* 18, no. 1 (2021): 9-22.

[17] Khatri, N. and Tyagi, S., 2015. Influences of natural and anthropogenic factors on surface and groundwater quality in rural and urban areas. *Frontiers in life science*, *8*(1), pp.23-39.

[18] Sangamnere, R., Misra, T., Bherwani, H., Kapley, A. and Kumar, R., 2023. A critical review of conventional and emerging wastewater treatment technologies. *Sustainable Water Resources Management*, *9*(2), p.58.

[19] Schellenberg, T., Subramanian, V., Ganeshan, G., Tompkins, D. and Pradeep, R., 2020. Wastewater discharge standards in the evolving context of urban sustainability–The case of India. *Frontiers in Environmental Science*, *8*, p.30.

[20] Wate, S.R., 2012. An overview of policies impacting water quality and governance in India. *International journal of water resources development*, *28*(2), pp.265-279.

[21] Srinivas, R., Singh, A.P. and Shankar, D., 2020. Understanding the threats and challenges concerning Ganges River basin for effective policy recommendations towards sustainable development. *Environment, Development and Sustainability*, *22*, pp.3655-3690.

[22] Murugaiah, V., Shashidhar, R. and Ramakrishna, V., 2018. Smart Cities Mission and AMRUT scheme: Analysis in the context of Sustainable Development. *OIDA International Journal of Sustainable Development*, *11*(10), pp.49-60.

[23] Maxmut O'g'li, X.F., 2023. Renewable energy sources: advancements, challenges, and prospects. *International Journal of Advance Scientific Research*, *3*(08), pp.14-25.

[24] Sen, S. and Ganguly, S., 2017. Opportunities, barriers and issues with renewable energy development–A discussion. *Renewable and sustainable energy reviews*, *69*, pp.1170-1181.

[25] Quaschning, V., 2014. *Understanding renewable energy systems*. Routledge.

[26] Rahman, A., Farrok, O. and Haque, M.M., 2022. Environmental impact of renewable energy source based electrical power plants: Solar, wind, hydroelectric, biomass, geothermal, tidal, ocean, and osmotic. *Renewable and Sustainable Energy Reviews*, *161*, p.112279.

[27] Dada, M. and Popoola, P., 2023. Recent advances in solar photovoltaic materials and systems for energy storage applications: a review. *Beni-Suef University Journal of Basic and Applied Sciences*, *12*(1), pp.1-15.

[28] ALI, L.M., Ali, Q.A., Klačková, I., Issa, H.A., Yakimovich, B.A. and Kuvshimov, V.V., 2021. Developing a thermal design for steam power plants by using concentrating solar power technologies for a clean environment. *Acta Montanistica Slovaca*, *26*(4).

[29] Pan, L. and Shao, C., 2020. Wind energy conversion systems analysis of PMSG on offshore wind turbine using improved SMC and Extended State Observer. *Renewable Energy*, *161*, pp.149-161.

[30] Siri, R., Mondal, S.R. and Das, S., 2021. Hydropower: A renewable energy resource for sustainability in terms of climate change and environmental protection. *Alternative Energy Resources: The Way to a Sustainable Modern Society*, pp.93-113.

[31] El Haj Assad, M., Ahmadi, M.H., Sadeghzadeh, M., Yassin, A. and Issakhov, A., 2021. Renewable hybrid energy systems using geothermal energy: hybrid solar thermal–geothermal power plant. *International Journal of Low-Carbon Technologies*, *16*(2), pp.518-530.

[32] Makul, N., Fediuk, R., Amran, M., Al-Akwaa, M.S., Pralat, K., Nemova, D., Petropavlovskii, K., Novichenkova, T., Petropavlovskaya, V. and Sulman, M., 2021. Utilization of biomass to ash: An overview of the potential resources for alternative energy. *Materials*, *14*(21), p.6482.

[33] Chowdhury, M.S., Rahman, K.S., Selvanathan, V., Nuthammachot, N., Suklueng, M., Mostafaeipour, A., Habib, A., Akhtaruzzaman, M., Amin, N. and Techato, K., 2021. Current trends and prospects of tidal energy technology. *Environment, development and sustainability*, *23*, pp.8179-8194.

[34] Rodrigues, C., Nunes, D., Clemente, D., Mathias, N., Correia, J.M., Rosa-Santos, P., Taveira-Pinto, F., Morais, T., Pereira, A. and Ventura, J., 2020. Emerging triboelectric nanogenerators for ocean wave energy harvesting: state of the art and future perspectives. *Energy & Environmental Science*, *13*(9), pp.2657-2683.

[35] Zamora-Ledezma, C., Negrete-Bolagay, D., Figueroa, F., Zamora-Ledezma, E., Ni, M., Alexis, F. and Guerrero, V.H., 2021. Heavy metal water pollution: A fresh look about hazards, novel and conventional remediation methods. *Environmental Technology & Innovation*, *22*, p.101504.

[36] Rafiq, A., Ikram, M., Ali, S., Niaz, F., Khan, M., Khan, Q. and Maqbool, M., 2021. Photocatalytic degradation of dyes using semiconductor photocatalysts to clean industrial water pollution. *Journal of Industrial and Engineering Chemistry*, *97*, pp.111-128.

[37] Badawi, A.K. and Zaher, K., 2021. Hybrid treatment system for real textile wastewater remediation based on coagulation/flocculation, adsorption and filtration processes: performance and economic evaluation. *Journal of Water Process Engineering*, *40*, p.101963.

[38] Ukhurebor, K.E., Hossain, I., Pal, K., Jokthan, G., Osang, F., Ebrima, F. and Katal, D., 2024. Applications and contemporary issues with adsorption for water monitoring and remediation: a facile review. *Topics in Catalysis*, *67*(1), pp.140-155.

[39] Yang, Y., Ye, S., Zhang, C., Zeng, G., Tan, X., Song, B., Zhang, P., Yang, H., Li, M. and Chen, Q., 2021. Application of biochar for the remediation of polluted sediments. *Journal of Hazardous Materials*, *404*, p.124052.

[40] Badawi, A.K. and Zaher, K., 2021. Hybrid treatment system for real textile wastewater remediation based on coagulation/flocculation, adsorption and filtration processes: performance and economic evaluation. *Journal of Water Process Engineering*, *40*, p.101963.

[41] Liu, Y., Ali, A., Su, J.F., Li, K., Hu, R.Z. and Wang, Z., 2023. Microbial-induced calcium carbonate precipitation: Influencing factors, nucleation pathways, and application in waste water remediation. *Science of the Total Environment*, *860*, p.160439.

[42] Xiao, Z., Li, D., Zhu, Q. and Sun, Z., 2020. Simultaneous removal of NO and SO2 through a new wet recycling oxidation–reduction process utilizing micro-nano bubble gas–liquid dispersion system based on Na2SO3. *Fuel*, *263*, p.116682.

[43] Buaisha, M., Balku, S. and Özalp-Yaman, S., 2020. Heavy metal removal investigation in conventional activated sludge systems. *Civil Engineering Journal*, *6*(3), pp.470-477.

[44] Rout, P.R., Shahid, M.K., Dash, R.R., Bhunia, P., Liu, D., Varjani, S., Zhang, T.C. and Surampalli, R.Y., 2021. Nutrient removal from domestic wastewater: A comprehensive review on conventional and advanced technologies. *Journal of Environmental Management*, *296*, p.113246.

[45] Zhao, C., Xu, J., Shang, D., Zhang, Y., Zhang, J., Xie, H., Kong, Q. and Wang, Q., 2021. Application of constructed wetlands in the PAH remediation of surface water: A review. *Science of The Total Environment*, *780*, p.146605.

[46] Xiang, H., Min, X., Tang, C.J., Sillanpää, M. and Zhao, F., 2022. Recent advances in membrane filtration for heavy metal removal from wastewater: A mini review. *Journal of Water Process Engineering*, *49*, p.103023.

[47] Ebrahimzadeh, S., Wols, B., Azzellino, A., Martijn, B.J. and van der Hoek, J.P., 2021. Quantification and modelling of organic micropollutant removal by reverse osmosis (RO) drinking water treatment. *Journal of Water Process Engineering*, *42*, p.102164.

[48] Joseph, J., Radhakrishnan, R.C., Johnson, J.K., Joy, S.P. and Thomas, J., 2020. Ion-exchange mediated removal of cationic dye-stuffs from water using ammonium phosphomolybdate. *Materials Chemistry and Physics*, *242*, p.122488.

[49] Hashim, K.S., AlKhaddar, R., Shaw, A., Kot, P., Al-Jumeily, D., Alwash, R. and Aljefery, M.H., 2020. Electrocoagulation as an eco-friendly River water treatment method. In *Advances in Water Resources Engineering and Management: Select Proceedings of TRACE 2018* (pp. 219-235). Springer Singapore.

[50] Yang, Y., 2020. Recent advances in the electrochemical oxidation water treatment: Spotlight on byproduct control. *Frontiers of Environmental Science & Engineering*, *14*(5), p.85.

[51] Wang, L., Zhu, Z., Wang, F., Qi, Y., Zhang, W. and Wang, C., 2021. State-of-the-art and prospects of Zn-containing layered double hydroxides (Zn-LDH)-based materials for photocatalytic water remediation. *Chemosphere*, *278*, p.130367.

[52] Mondal, D., Bardhan, S., Das, N., Roy, J., Ghosh, S., Maity, A., Roy, S., Basu, R. and Das, S., 2022. Natural clay-based reusable piezo-responsive membrane for water droplet mediated energy harvesting, degradation of organic dye and pathogenic bacteria. *Nano Energy*, *104*, p.107893.

[53] Covaci, C. and Gontean, A., 2020. Piezoelectric energy harvesting solutions: A review. *Sensors*, *20*(12), p.3512.

[54] Liang, Z., Yan, C.F., Rtimi, S. and Bandara, J., 2019. Piezoelectric materials for catalytic/photocatalytic removal of pollutants: Recent advances and outlook. *Applied Catalysis B: Environmental*, *241*, pp.256-269.

[55] Karan, S.K., Maiti, S., Lee, J.H., Mishra, Y.K., Khatua, B.B. and Kim, J.K., 2020. Recent advances in self-powered tribo-/piezoelectric energy harvesters: all-in-one package for future smart technologies. *Advanced Functional Materials*, *30*(48), p.2004446.

[56] Sodano, H.A., Inman, D.J. and Park, G., 2004. A review of power harvesting from vibration using piezoelectric materials. *Shock and Vibration Digest*, *36*(3), pp.197-206.

[57] Wakshume, D.G. and Płaczek, M.Ł., 2024. Optimizing Piezoelectric Energy Harvesting from Mechanical Vibration for Electrical Efficiency: A Comprehensive Review. *Electronics*, *13*(5), p.987.

[58] Shaukat, H., Ali, A., Ali, S., Altabey, W.A., Noori, M. and Kouritem, S.A., 2023. Applications of sustainable hybrid energy harvesting: a review. *Journal of Low Power Electronics and Applications*, *13*(4), p.62.

[59] Heywang, W. and Thomann, H., 1984. Tailoring of piezoelectric ceramics. *Annual Review of Materials Science*, *14*(1), pp.27-47.

[60] Manbachi, A. and Cobbold, R.S., 2011. Development and application of piezoelectric materials for ultrasound generation and detection. *Ultrasound*, *19*(4), pp.187-196.

[61] Safaei, M., Sodano, H.A. and Anton, S.R., 2019. A review of energy harvesting using piezoelectric materials: state-of-the-art a decade later (2008–2018). *Smart materials and structures*, *28*(11), p.113001.

[62] Guo, L. and Lu, Q., 2017. Potentials of piezoelectric and thermoelectric technologies for harvesting energy from pavements. *Renewable and Sustainable Energy Reviews*, *72*, pp.761-773.

[63] Anton, S.R. and Sodano, H.A., 2007. A review of power harvesting using piezoelectric materials (2003–2006). *Smart materials and Structures*, *16*(3), p.R1.

[64] Uchino, K., 2018. Piezoelectric energy harvesting systems—essentials to successful developments. *Energy Technology*, *6*(5), pp.829-848.

[65] Bosso, N., Magelli, M. and Zampieri, N., 2021. Application of low-power energy harvesting solutions in the railway field: a review. *Vehicle System Dynamics*, *59*(6), pp.841-871.

[66] Chen, Y. and Xue, X., 2018. Advances in the structural health monitoring of bridges using piezoelectric transducers. *Sensors*, *18*(12), p.4312.

[67] Abbasipour, M., Khajavi, R. and Akbarzadeh, A.H., 2022. A comprehensive review on piezoelectric polymeric and ceramic nanogenerators. *Advanced Engineering Materials*, *24*(6), p.2101312.

[68] Fang, X.Q., Liu, J.X. and Gupta, V., 2013. Fundamental formulations and recent achievements in piezoelectric nano-structures: a review. *Nanoscale*, *5*(5), pp.1716-1726.

[69] Tian, Y., Jia, Y., Bao, Y. and Chen, Y., 2007. Macro-quantity synthesis of AlN nanowires via combined technique of arc plasma jet and thermal treatment. *Diamond and related materials*, *16*(2), pp.302-305.

[70] Wang, Y., Guo, X., Li, L.H., Zhang, J., Li, G.K., Zavabeti, A. and Li, Y., 2022. Enhanced piezoelectric properties enabled by engineered low-dimensional nanomaterials. *ACS Applied Nano Materials*, *5*(9), pp.12126-12142.

[71] Kaur, J. and Singh, H., 2020. Fabrication and analysis of piezoelectricity in 0D, 1D and 2D Zinc Oxide nanostructures. *Ceramics International*, *46*(11), pp.19401-19407.

[72] Gong, C., Sun, S., Zhang, Y., Sun, L., Su, Z., Wu, A. and Wei, G., 2019. Hierarchical nanomaterials via biomolecular self-assembly and bioinspiration for energy and environmental applications. *Nanoscale*, *11*(10), pp.4147-4182.

[73] Li, X., Sun, M., Wei, X., Shan, C. and Chen, Q., 2018. 1D piezoelectric material based nanogenerators: methods, materials and property optimization. *Nanomaterials*, *8*(4), p.188.

[74] Hasan, M.A.M., Wang, Y., Bowen, C.R. and Yang, Y., 2021. 2D nanomaterials for effective energy scavenging. *Nano-Micro Letters*, *13*, pp.1-41.

[75] Okhay, O. and Tkach, A., 2023. Current Achievements in Flexible Piezoelectric Nanogenerators Based on Barium Titanate. *Nanomaterials*, *13*(6), p.988.

[76] Lyu, Z., Ding, S., Du, D., Qiu, K., Liu, J., Hayashi, K., Zhang, X. and Lin, Y., 2022. Recent advances in biomedical applications of 2D nanomaterials with peroxidase-like properties. *Advanced Drug Delivery Reviews*, *185*, p.114269.

[77] Li, J., Long, Y. and Wang, X., 2020. Polymer-based nanogenerator for biomedical applications. *Chemical Research in Chinese Universities*, *36*, pp.41-54.

[78] Minary-Jolandan, M., Bernal, R.A., Kuljanishvili, I., Parpoil, V. and Espinosa, H.D., 2012. Individual GaN nanowires exhibit strong piezoelectricity in 3D. *Nano letters*, *12*(2), pp.970-976.

[79] Sun, Y., Li, X., Vijayakumar, A., Liu, H., Wang, C., Zhang, S., Fu, Z., Lu, Y. and Cheng, Z., 2021. Hydrogen generation and degradation of organic dyes by new piezocatalytic 0.7 BiFeO3–0.3 BaTiO3 nanoparticles with proper band alignment. *ACS Applied Materials & Interfaces*, *13*(9), pp.11050-11057.

[80] M. Smith, S. Kar-Narayan, Piezoelectric polymers: theory, challenges and opportunities, Https://Doi.Org/10.1080/09506608.2021.1915935. 67 (2021) 65–88. https://doi.org/10.1080/09506608.2021.1915935.

[81] Ramadan, K.S., Sameoto, D. and Evoy, S., 2014. A review of piezoelectric polymers as functional materials for electromechanical transducers. *Smart Materials and Structures*, *23*(3), p.033001.

[82] Turner, B.L., Senevirathne, S., Kilgour, K., McArt, D., Biggs, M., Menegatti, S. and Daniele, M.A., 2021. Ultrasound-powered implants: a critical review of piezoelectric material selection and applications. *Advanced healthcare materials*, *10*(17), p.2100986.

[83] Smith, M. and Kar-Narayan, S., 2022. Piezoelectric polymers: theory, challenges and opportunities. *International Materials Reviews*, *67*(1), pp.65-88.

[84] Kapat, K., Shubhra, Q.T., Zhou, M. and Leeuwenburgh, S., 2020. Piezoelectric nano-biomaterials for biomedicine and tissue regeneration. *Advanced Functional Materials*, *30*(44), p.1909045.

[85] Mondal, D., Roy, S., Bardhan, S., Roy, J., Kanungo, I., Basu, R. and Das, S., 2022. Recent advances in piezocatalytic polymer nanocomposites for wastewater remediation. *Dalton Transactions*, *51*(2), pp.451-462.

[86] Eltouby, P., Shyha, I., Li, C. and Khaliq, J., 2021. Factors affecting the piezoelectric performance of ceramic-polymer composites: A comprehensive review. *Ceramics International*, *47*(13), pp.17813-17825.

[87] Riccucci, G., Pezzana, L., Lantean, S., Tori, A., Spriano, S. and Sangermano, M., 2021. Investigation of the thermal conductivity of silicon-base composites: The effect of filler materials and characteristic on thermo-mechanical response of silicon composite. *Applied Sciences*, *11*(12), p.5663.

[88] Pradhan, S.S., Unnikrishnan, L., Mohanty, S. and Nayak, S.K., 2020. Thermally conducting polymer composites with EMI shielding: a review. *Journal of Electronic Materials*, *49*, pp.1749-1764.

[89] Mishra, S., Unnikrishnan, L., Nayak, S.K. and Mohanty, S., 2019. Advances in piezoelectric polymer composites for energy harvesting applications: a systematic review. *Macromolecular Materials and Engineering*, *304*(1), p.1800463.

[90] Panda, P.K. and Sahoo, B., 2015. PZT to lead free piezo ceramics: a review. *Ferroelectrics*, *474*(1), pp.128-143.

[91] Xu, H., Hao, Z., Wang, C., Deng, J., Wang, T. and Zhang, J., 2023. In situ emulsion polymerization to multifunctional polymer nanocomposites: a review. *Macromolecular Chemistry and Physics*, *224*(20), p.2300185.

[92] Yibowei, M.E., Adekoya, J.G., Adediran, A.A. and Adekomaya, O., 2021. Carbon-based nano-filler in polymeric composites for supercapacitor electrode materials: a review. *Environmental Science and Pollution Research*, *28*, pp.26269-26279.

[93] Mariello, M., Fachechi, L., Guido, F. and De Vittorio, M., 2021. Multifunctional sub-100 μm thickness flexible piezo/triboelectric hybrid water energy harvester based on biocompatible AlN and soft parylene C-PDMS-Ecoflex™. *Nano Energy*, *83*, p.105811.

[94] Jayaraman, K., Kotaki, M., Zhang, Y., Mo, X. and Ramakrishna, S., 2004. Recent advances in polymer nanofibers. *Journal of Nanoscience and Nanotechnology*, *4*(1-2), pp.52-65.

[95] Chen, S., Chen, Y., Zhao, Y., Zhang, L., Zhu, C., Zhang, Y., Liu, S., Xia, S., Yu, J., Ding, B. and Yan, J., 2022. Status and strategies for fabricating flexible oxide ceramic micro-nanofiber materials. *Materials Today*, *61*, pp.139-168.

[96] Bhadra, J., Ponnamma, D., Alkareem, A., Parangusan, H., Ahmad, Z., Al-Thani, N., Daifalla, A.K., Al-Sanari, N.A. and Mohamed, R., 2022. Development of a piezoelectric nanogenerator based on mesoporous silica/zinc oxide hybrid nanocomposite fibres. *International Journal of Energy Research*, *46*(6), pp.8503-8515.

[97] Yu, X., Pan, J., Zhang, J., Sun, H., He, S., Qiu, L., Lou, H., Sun, X. and Peng, H., 2017. A coaxial triboelectric nanogenerator fiber for energy harvesting and sensing under deformation. *Journal of materials chemistry A*, *5*(13), pp.6032-6037.

[98] Xu, S. and Shi, Y., 2009, January. Mechanical and piezoelectric properties of PZT nanofibers. In *International Design Engineering Technical Conferences and Computers and Information in Engineering Conference* (Vol. 49033, pp. 363-366).

[99] Lee, J.T., Lin, M.C. and Wu, J.M., 2022. High-efficiency cycling piezo-degradation of organic pollutants over three liters using MoS2/carbon fiber piezocatalytic filter. *Nano Energy*, *98*, p.107280.

[100] Fan, N., Wang, Y., Liu, B., Yang, H. and Liu, S., 2023. Origin and Mechanism of Piezoelectric and Photovoltaic Effects in (111) Polar Orientated NiO Films. *Advanced Science*, *10*(32), p.2304637.

[101] Zhang, Q., Zheng, Z., Gao, R., Xiao, X., Jiao, M., Wang, B., Zhou, G. and Cheng, H.M., 2024. Constructing Bipolar Dual-Active Sites through High-Entropy-Induced Electric Dipole Transition for Decoupling Oxygen Redox. *Advanced Materials*, p.2401018.

[102] Kumar, R. and Kumar, K., 2023. Piezoelectric Smart Material-Based Self-Charging Supercapacitor.

[103] Li, Z., Lan, S. and Zhu, M., 2024. Piezoelectricity activates persulfate for water treatment: A perspective. *Environmental Science and Ecotechnology*, *18*, p.100329.

[104] Bößl, F. and Tudela, I., 2021. Piezocatalysis: Can catalysts really dance?. *Current Opinion in Green and Sustainable Chemistry*, *32*, p.100537.

[105] Tu, S., Guo, Y., Zhang, Y., Hu, C., Zhang, T., Ma, T. and Huang, H., 2020. Piezocatalysis and piezo-photocatalysis: catalysts classification and modification strategy, reaction mechanism, and practical application. *Advanced Functional Materials*, *30*(48), p.2005158.

[106] Lei, H., Wu, M., Mo, F., Ji, S., Dong, X., Wu, Z., Gao, J., Yang, Y. and Jia, Y., 2020. Tribo-catalytic degradation of organic pollutants through bismuth oxyiodate triboelectrically harvesting mechanical energy. *Nano Energy*, *78*, p.105290.

[107] Jin, C., Liu, D., Hu, J., Wang, Y., Zhang, Q., Lv, L. and Zhuge, F., 2019. The role of microstructure in piezocatalytic degradation of organic dye pollutants in wastewater. *Nano Energy*, *59*, pp.372-379.

[108] Orudzhev, F., Ramazanov, S., Sobola, D., Kaspar, P., Trčka, T., Částková, K., Kastyl, J., Zvereva, I., Wang, C., Selimov, D. and Gulakhmedov, R., 2021. Ultrasound and water flow driven piezophototronic effect in self-polarized flexible α-Fe2O3 containing PVDF nanofibers film for enhanced catalytic oxidation. *Nano Energy*, *90*, p.106586.

[109] Liang, Z., Yan, C.F., Rtimi, S. and Bandara, J., 2019. Piezoelectric materials for catalytic/photocatalytic removal of pollutants: Recent advances and outlook. *Applied Catalysis B: Environmental*, *241*, pp.256-269.

[110] Zheng, S., Li, X., Zhang, J., Wang, J., Zhao, C., Hu, X., Wu, Y. and He, Y., 2023. One-step preparation of MoOx/ZnS/ZnO composite and its excellent performance in piezocatalytic degradation of Rhodamine B under ultrasonic vibration. *Journal of Environmental Sciences*, *125*, pp.1-13.

[111] Lin, E., Wu, J., Qin, N., Yuan, B. and Bao, D., 2018. Silver modified barium titanate as a highly efficient piezocatalyst. *Catalysis Science & Technology*, *8*(18), pp.4788-4796.

[112] Ning, X., Hao, A., Cao, Y., Hu, J., Xie, J. and Jia, D., 2020. Effective promoting piezocatalytic property of zinc oxide for degradation of organic pollutants and insight into piezocatalytic mechanism. *Journal of Colloid and Interface Science*, *577*, pp.290-299.

[113] Ma, W., Lv, M., Cao, F., Fang, Z., Feng, Y., Zhang, G., Yang, Y. and Liu, H., 2022. Synthesis and characterization of ZnO-GO composites with their piezoelectric catalytic and antibacterial properties. *Journal of Environmental Chemical Engineering*, *10*(3), p.107840.

[114] Wang, K., Han, C., Li, J., Qiu, J., Sunarso, J. and Liu, S., 2022. The mechanism of piezocatalysis: energy band theory or screening charge effect?. *Angewandte Chemie*, *134*(6), p.e202110429.

[115] Banerjee, S., Benjwal, P., Singh, M. and Kar, K.K., 2018. Graphene oxide (rGO)-metal oxide (TiO2/Fe3O4) based nanocomposites for the removal of methylene blue. *Applied surface science*, *439*, pp.560-568.

[116] Cheng, X., Liu, Z., Jing, Q., Mao, P., Guo, K., Lu, J., Xie, B. and Fan, H., 2023. Porous (K0. 5Na0. 5) 0.94 Li0. 06NbO3-polydimethylsiloxane piezoelectric composites harvesting mechanical energy for efficient decomposition of dye wastewater. *Journal of Colloid and Interface Science*, *629*, pp.11-21.

[117] Tian, W., Qiu, J., Li, N., Chen, D., Xu, Q., Li, H., He, J. and Lu, J., 2021. Efficient piezocatalytic removal of BPA and Cr (VI) with SnS2/CNFs membrane by harvesting vibration energy. *Nano Energy*, *86*, p.106036.

[118] Wu, J., Qin, N. and Bao, D., 2018. Effective enhancement of piezocatalytic activity of BaTiO3 nanowires under ultrasonic vibration. *Nano Energy*, *45*, pp.44-51.

[119] Bao, Y., Xiao, K., Yue, S., Zhang, M., Du, X., Wang, J., Oh, W.D., Zhou, Y. and Zhan, S., 2023. Wastewater decontamination via piezoelectric based technologies: Materials design, applications and prospects. *Surfaces and Interfaces*, *40*, p.103107.

[120] Li, X., Wang, J., Zhang, J., Zhao, C., Wu, Y. and He, Y., 2022. Cadmium sulfide modified zinc oxide heterojunction harvesting ultrasonic mechanical energy for efficient decomposition of dye wastewater. *Journal of Colloid and Interface Science*, *607*, pp.412-422.

[121] Ning, X., Hao, A., Cao, Y. and Jia, D., 2021. Boosting piezocatalytic performance of Ag decorated ZnO by piezo-electrochemical synergistic coupling strategy. *Applied Surface Science*, *566*, p.150730.

[122] Wu, J., Qin, N. and Bao, D., 2018. Effective enhancement of piezocatalytic activity of BaTiO3 nanowires under ultrasonic vibration. *Nano Energy*, *45*, pp.44-51.

[123] Zhang, Y., Bowen, C.R., Ghosh, S.K., Mandal, D., Khanbareh, H., Arafa, M. and Wan, C., 2019. Ferroelectret materials and devices for energy harvesting applications. *Nano Energy*, *57*, pp.118-140.

[124] Roy, J., Roy, S., Mondal, D., Bag, N., Chowdhury, J.R., Ghosh, S., Bardhan, S., Mondal, R., Basu, R. and Das, S., 2024. Gd-doped bismuth ferrite nanocomposite: A promising candidate for piezocatalytic degradation of organic dyes and pathogenic E. coli. *Surfaces and Interfaces*, *44*, p.103579.

[125] Wang, Y., Wen, X., Jia, Y., Huang, M., Wang, F., Zhang, X., Bai, Y., Yuan, G. and Wang, Y., 2020. Piezo-catalysis for nondestructive tooth whitening. *Nature communications*, *11*(1), p.1328.

[126] Ali, A., Chiang, Y.W. and Santos, R.M., 2022. X-ray diffraction techniques for mineral characterization: A review for engineers of the fundamentals, applications, and research directions. *Minerals*, *12*(2), p.205.

[127] Wuhrer, R. and Moran, K., 2016. Low voltage imaging and X-ray microanalysis in the SEM: challenges and opportunities. In *IOP Conference Series: Materials Science and Engineering* (Vol. 109, No. 1, p. 012019). IOP Publishing.

[128] Khan, I., Saeed, K. and Khan, I., 2019. Nanoparticles: Properties, applications and toxicities. *Arabian journal of chemistry*, *12*(7), pp.908-931.

[129] Bharatiya, D., Parhi, B., Sahu, H. and Swain, S.K., 2023. Factors influencing the dielectric properties of GO/MO nanocomposites. *Journal of Materials Science: Materials in Electronics*, *34*(5), p.452.

[130] Martins, P., Lopes, A.C. and Lanceros-Mendez, S., 2014. Electroactive phases of poly (vinylidene fluoride): Determination, processing and applications. *Progress in polymer science*, *39*(4), pp.683-706.

[131] Oyedotun, T.D.T., 2018. X-ray fluorescence (XRF) in the investigation of the composition of earth materials: a review and an overview. *Geology, Ecology, and Landscapes*, *2*(2), pp.148-154.

[132] Kamble, S., Agrawal, S., Cherumukkil, S., Sharma, V., Jasra, R.V. and Munshi, P., 2022. Revisiting zeta potential, the key feature of interfacial phenomena, with applications and recent advancements. *ChemistrySelect*, *7*(1), p.e202103084.

[133] Bardestani, R., Patience, G.S. and Kaliaguine, S., 2019. Experimental methods in chemical engineering: specific surface area and pore size distribution measurements—BET, BJH, and DFT. *The Canadian Journal of Chemical Engineering*, *97*(11), pp.2781-2791.

[134] Saadatkhah, N., Carillo Garcia, A., Ackermann, S., Leclerc, P., Latifi, M., Samih, S., Patience, G.S. and Chaouki, J., 2020. Experimental methods in chemical engineering: Thermogravimetric analysis—TGA. *The Canadian Journal of Chemical Engineering*, *98*(1), pp.34-43.

[135] Coleman, N.J. and Craig, D.Q., 1996. Modulated temperature differential scanning calorimetry: a novel approach to pharmaceutical thermal analysis. *International journal of pharmaceutics*, *135*(1-2), pp.13-29.

[136] Jentoft, F.C., 2009. Ultraviolet–visible–near infrared spectroscopy in catalysis: theory, experiment, analysis, and application under reaction conditions. *Advances in catalysis*, *52*, pp.129-211.

[137] Aoki, T., 2019. Photoluminescence. *Optical Properties of Materials and Their Applications*, pp.157-202.

[138] Zhu, L., 2014. Exploring strategies for high dielectric constant and low loss polymer dielectrics. *The journal of physical chemistry letters*, *5*(21), pp.3677-3687.

[139] Saha, S., Nandy, A., Meikap, A.K. and Pradhan, S.K., 2015. Electric modulus formalism and electrical transport property of ball mill synthesized nanocrystalline Mn doped ZrO2 solid solution. *Physica B: Condensed Matter*, *479*, pp.67-73.

[140] Maini, A.K., 2007. *Digital electronics: principles, devices and applications*. John Wiley & Sons.

Chapter 2

Study of physicochemical properties of α-hematite due to size fractionation

Chapter 2

Study of physicochemical properties of α-hematite due to size fractionation

2.1 Introduction

Nanomaterials have become essential in cutting-edge technologies, owing to unique mechanical, electrical, optical, and magnetic properties [1]. Their applications include tailored supercapacitive materials, nano-sensors, green batteries, and piezoelectric nanogenerators [2]. While chemical precipitation is the conventional method for nanoparticle synthesis, recent research focuses on environmentally friendly techniques like high-energy ball milling [3]. In the realm of energy harvesting, chemically synthesized nanoparticles are gaining attraction, but concerns over high costs and environmental toxicity drive the search for cost-effective, non-toxic, and biocompatible materials. Natural resources, prized for their eco-friendly performance and low cost, are being explored for industrial applications nowadays [4].

Hematite (α-Fe_2O_3), a common environmental mineral with a rhombohedral phase, is well-suited for various ferromagnetic applications [5]. In its nanoform, hematite exhibits excellent ferromagnetic behavior, influenced by morphology and particle size. However, widely used in magnetic, optical, and mechanical devices, nanonized hematite is typically synthesized through chemical precipitation methods [6].

The chapter presents a detailed top-down approach for synthesizing finer samples of hematite from its naturally available bulk counterpart. Size fractioning by high energy ball milling technique produced three distinct size ranges, which were subsequently characterized by basic characterization techniques. Augmentation of electrical property, especially the dielectric permittivity of the nano-sized samples was found along with a very low tangent loss. High-temperature stability was an added asset of the material. These important observations indicated that the synthesized nano-hematite might be efficiently used in energy harvesting applications.

2.2 Experimental details

2.2.1 Material synthesis

Natural hematite was purchased from Bharat Engineering, Kolkata, India. Acetone and Potassium bromide (KBr) were purchased from Merck, India. Millipore water of ~18.2 MΩ.cm resistivity was used throughout the experiment.

Initially, natural hematite was crushed in a diamond mortar manually to reduce its size and further, it was grounded in an agate mortar to get finer substance. Size fraction (S1) was obtained by sieving the mortared sample through 100 meshes. Then a portion of the coarse fraction (S1) was mechanically ball-milled by Fritsch Planetary Mono Mill Pulverisette 6 using tungsten carbide vials and balls, maintaining a ball-to-sample mass ratio of 20:1 at 300 rpm. A fraction of the sample was collected from the ball mill after 3 h and was marked as S2. To get the finer sample, ball milling was performed for another 9 h and the end product was named as S3. After each milling cycle, acetone was used to wash the samples.

2.3. Results and discussion

2.3.1 Structural and Morphological Analysis

X-ray diffraction (XRD) is one of the useful techniques for evaluating the phase and microstructure of a material [7-9]. It also provides information on the crystallographic structure, size, growth, and purity of the material [10-12]. The XRD patterns of the samples (S1, S2, S3) are shown in Figure 2.1. Diffraction maxima, at 2θ values 24.36˚, 33.37˚, 35.89˚, 49.77˚, 54.32˚, 57.83˚, 62.71˚ and 64.26˚, found for all three samples, were in good agreement with the JCPDS (Joint Committee on Powder Diffraction Standards) card no. 85-0599, which indicated that the samples were pure hematite. Gradual peak broadening was observed for smaller sizes (S2 and S3). The value of Full Width at Half Maxima (FWHM) corresponding to the (121) plane was around 0.0045815 for S1, with a gradual increase in the case of S2 (0.004642) and S3 (0.00846) respectively.
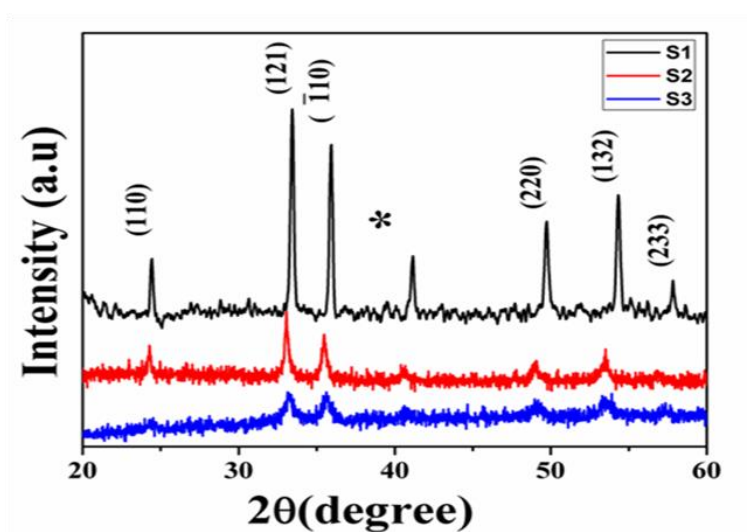
Figure 2.1. XRD pattern for S1(Bulk), S2 (Intermediate), S3 (Nano) α-hematite

The average crystallite sizes of S1, S2, and S3 were calculated for the peak (121) using the Debye-Scherrer equation (equation 1.7, Chapter 1) [13-14]. The mean crystallite sizes of the samples progressively decreased with ball milling duration, indicating the reduction of particle size due to the high energy mechanical attrition approach (Table 2.1). The characteristic peak heights related to S2 and S3 decreased with the period of ball milling, which eventually specified the decline in the crystallinity of the samples. A small diffraction plane is present at around $2\theta \approx 42.1°$ in sample S1, due to impurity i.e., alumino-silicate (marked with an asterisk in Figure 2.1), largely reduced in S3. This may be due to the simultaneous effect of the high-energy grinding process and subsequent acetone wash, which finally pulled out the impure alumino-silicate phase from the natural hematite sample [15].

Table 2.1. Structural and morphological parameters of the three different samples S1 (Bulk), S2 (Intermediate), and S3 (Nano) calculated from XRD and FESEM data

Sample	FWHM (rad)	D(nm)	Average grain size (nm) [from FESEM]
S1 (Bulk)	0.0045815	31.53	723
S2 (Intermediate)	0.004642	31.188	131
S3 (Nano)	0.00846	17.12	75

To ascertain the bonding networks and bond structures of the samples, Fourier-transform infrared spectroscopy (FTIR) was employed [16]. FTIR spectra of S1, S2, and S3 are shown in Figure 2.2. Absorption bands observed at 469 and 541 cm^{-1} matched well with literature supporting the presence of metal-oxygen stretching vibrations [17]. A small vibration located at 2362 cm^{-1} was due to the adsorption of atmospheric CO_2 [18]. Few broad stretching modes situated between 3600-3800 cm^{-1} can be attributed to asymmetric and symmetric vibration of -OH due to the absorption of atmospheric moisture [19]. These types of simultaneous adsorption of atmospheric CO_2 and moisture by the surfaces of the samples were due to the high porosity of the samples, which was further justified herein with the help of BET-BJH analysis. Vibration maxima located at around 910, 1014, and 1115 cm^{-1} (in the S1 sample) were caused by to deformation of Al-OH and stretching of Si-O respectively, which suggested the existence of some impure phases of alumino-silicates in

S1 [20-21]. Additionally, two separate bands were observed at 2851 and 2924 cm^{-1} (in S1) and can be assigned to symmetric and anti-symmetric stretching of C-H bonds respectively, indicating the presence of organic carbon in the starting material i.e., natural hematite [22-23]. These bands associated with the impurities in the sample decreased gradually in S2 and S3, implying the reduction of impure phases owing to enhancement in ball milling duration and subsequent washing of the samples with acetone. Therefore, the analysis from the FTIR study was in good agreement with the XRD results indicating the formation of pure hematite in the nano regime.
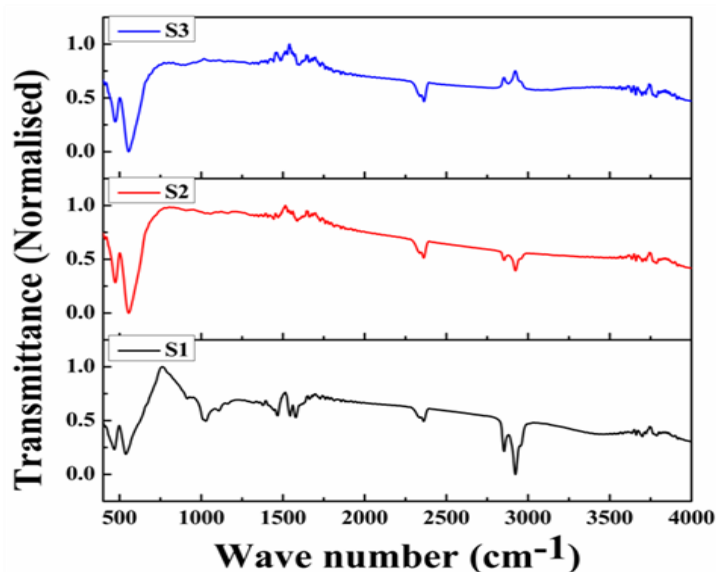
Figure 2.2. FTIR spectra for S1(Bulk), S2 (Intermediate), S3 (Nano) α-hematite

Field Emission Scanning Electron Microscopy (FESEM) was employed to study the morphology and associated characteristics of the experimental samples [Figure 2.3]. The FESEM micrographs of natural bulk material (S1) showed a plate-like structure with a mean size of 723 nm. With the increase in ball milling duration gradual decrease in mean particle size of 131nm and 75nm for S2 and S3 respectively was observed. Moreover, a distinct change in morphology was detected, where S2 showed an admixture of platy and irregular shape and S3 possessed a nearly spherical particle-like configuration. Thus, the course of high-energy ball-milling not only changed the particle size but also altered the morphologies of the samples significantly.
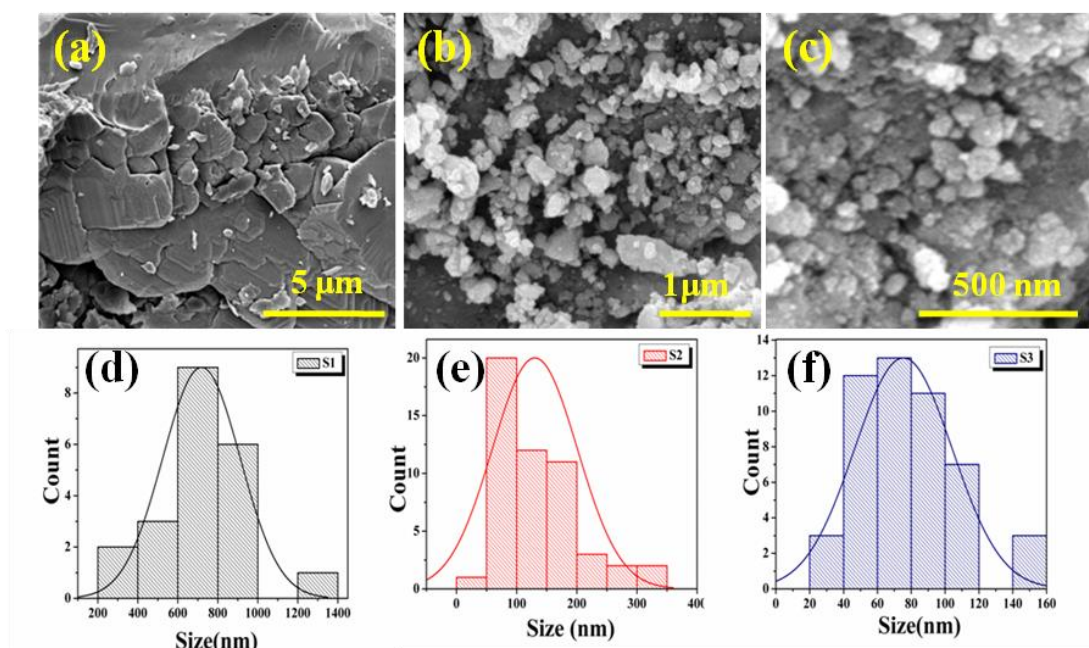
Figure 2.3. *FESEM images for S1(Bulk) (a), S2 (Intermediate) (b), and S3 (Nano)(c) with their corresponding size distribution curve (d-f)*

2.3.2 Elemental analysis

The study of X-ray fluorescence (XRF) is one of the common techniques to determine the elemental compositions of a material [24]. The XRF data (Table 2.2) designated that unwanted impurities like Na_2O, MgO, Al_2O_3, SiO_2, P_2O_5, K_2O, CaO, and TiO_2 assorted with Fe_2O_3 in the natural sample (S1) were largely reduced in S2 and S3. The concentration of Fe_2O_3 was 99.07% in S2 and 99.21% in S3, again in conformity with the fact that the ball milling duration with subsequent acetone wash gradually reduced the impure phases in natural hematite.

***Table 2.2.** Elemental composition of samples S1 (Bulk), S2 (Intermediate), S3 (Nano)*

analyzed from XRF

Sample Name	Compound Name	Concentration (%)
S1 (Bulk)	Na_2O	0.09
	MgO	0.28
	Al_2O_3	4.11
	SiO_2	4.55
	P_2O_5	0.08
	K_2O	0.07
	CaO	0.06
	TiO_2	0.09
	Fe_2O_3	90.67
S2 (Intermediate)	Al_2O_3	0.34
	SiO_2	0.46
	P_2O_5	0.08
	K_2O	0.01
	CaO	0.02
	TiO_2	0.03
	Fe_2O_3	99.07
S3 (Nano)	Al_2O_3	0.28
	SiO_2	0.38
	P_2O_5	0.06
	K_2O	0.01
	CaO	0.03
	TiO_2	0.03
	Fe_2O_3	99.21

2.3.3 Surface area and pore distribution analysis

Brunauer-Emmett-Teller (BET) and Barrer-Joyner-Halenda (BJH) techniques using N_2 gas adsorption-desorption, were employed to study the pore size distribution and surface area of nanoparticles. The Figures for nitrogen (N_2) adsorption-desorption isotherms and pore size distributions for the samples are represented in Figure 2.4(a). The volumes of absorbed and desorbed nitrogen were nearly the same [Figure 2.4(a)]. This type of data refers to a type-IV isotherm which assures the existence of mesopores and is the signature of a good quality industrial absorbent material [25]. The data signified (Table 2.3) that with a decrease in particle size, the surface area increased while the pore size decreased, indicating an overall increase in the aspect ratio. Furthermore, the H4-type hysteresis loops were observed in all three samples indicating the existence of slit-like pores [26-27].

Table 2.3. *Sample area, pore size, and pore volume distribution of samples S1 (Bulk), S2 (Intermediate), and S3 (Nano) from BET*

Sample name	Surface area (m^2/g)	Pore size (nm)	Pore volume (mL/g)
S1 (Bulk)	19.51	3.908	0.068
S2 (Intermediate)	19.80	3.903	0.057
S3 (Nano)	21.69	3.681	0.151
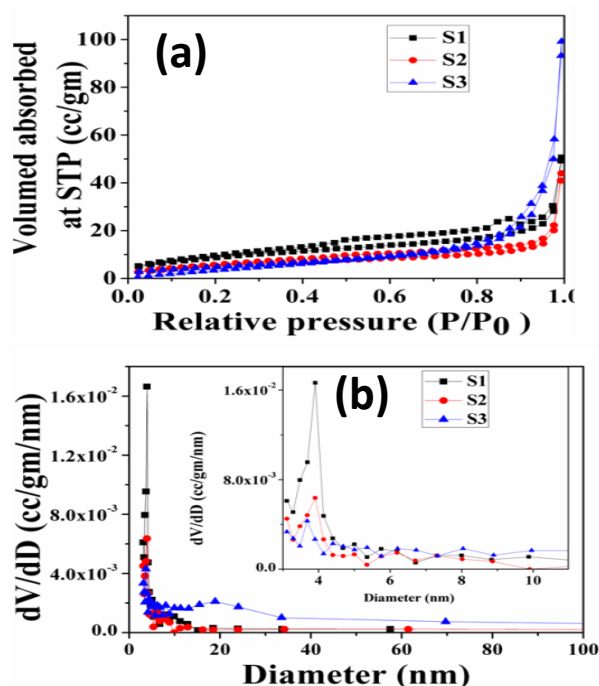
Figure 2.4. *Nitrogen (N₂) adsorption-desorption isotherms (a) and pore size distributions (b) for S1 (Bulk), S2 (Intermediate), S3 (Nano)*

2.3.4 Thermal characteristics of the synthesized samples

Thermo-gravimetric analysis (TGA) was employed to determine the percentage of mass loss as a function of varying temperatures to estimate the thermal stability of the samples. The behavior of synthesized samples was examined under varying temperatures (ranges from 30º- 400 ºC) at a constant heating rate of 10 ºC/min and the corresponding TGA graphs are depicted in Figure 2.5(a).

Mass losses for the samples S1, S2, and S3 were negligible (0.5%- 1%), primarily due to the release of surface adsorbed moisture within the pores of the hematite samples, indicating a sustainable stability of the sample up to 400 ˚C.

The thermographs obtained from differential thermal analysis (DTA) of the samples [Figure 2.5(b)] indicated mere endothermic heat transport phenomenon pointing the slope near 70 ºC, which agrees well with the outcome of the TGA data. Hence, it can be concluded that these materials are capable of retaining their physicochemical properties including electrical properties up to temperatures as high as 400 ºC.
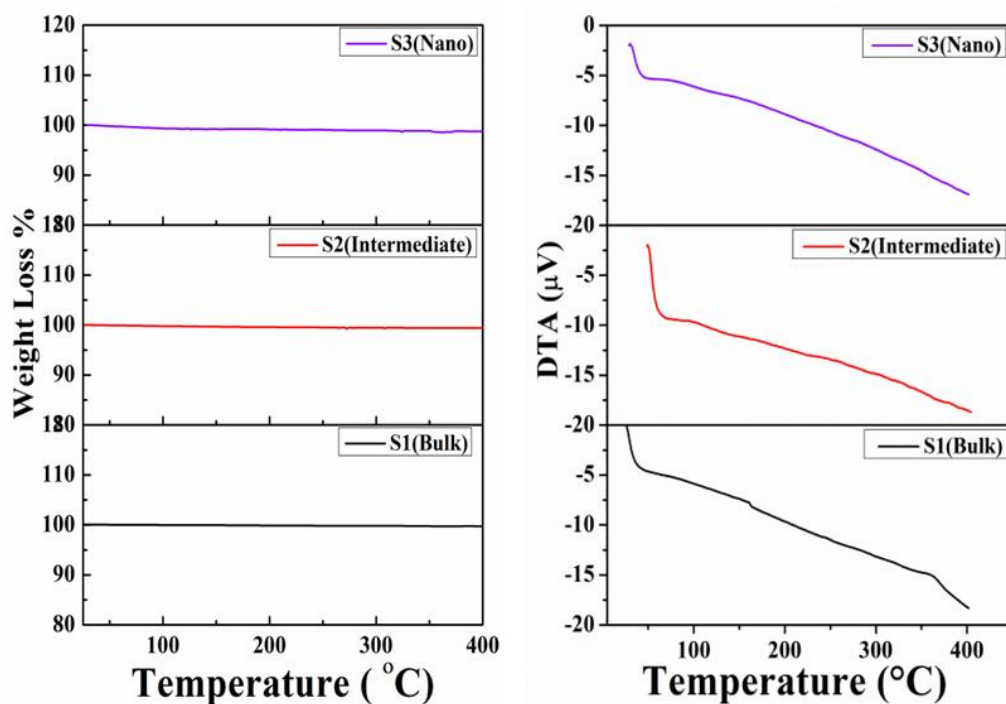
Figure 2.5. *Percentage mass losses (a) and heat transport phenomenon (b) for three different size fractions of natural hematite samples*

2.3.5 Studies of electrical properties

The dielectric property of a sample determines its competence to store charge carriers. Dielectric constant and tangent loss collectively depict the energy storage capacity of a material [28]. The temperature-dependent dielectric property of a sample needs to be studied in order to assess the proficiency of the material when used in an energy storage device within the necessary temperature range. The dielectric permittivity of a material depends on various factors like frequency of the applied electric field, temperature, and the structure of the material [25,29].
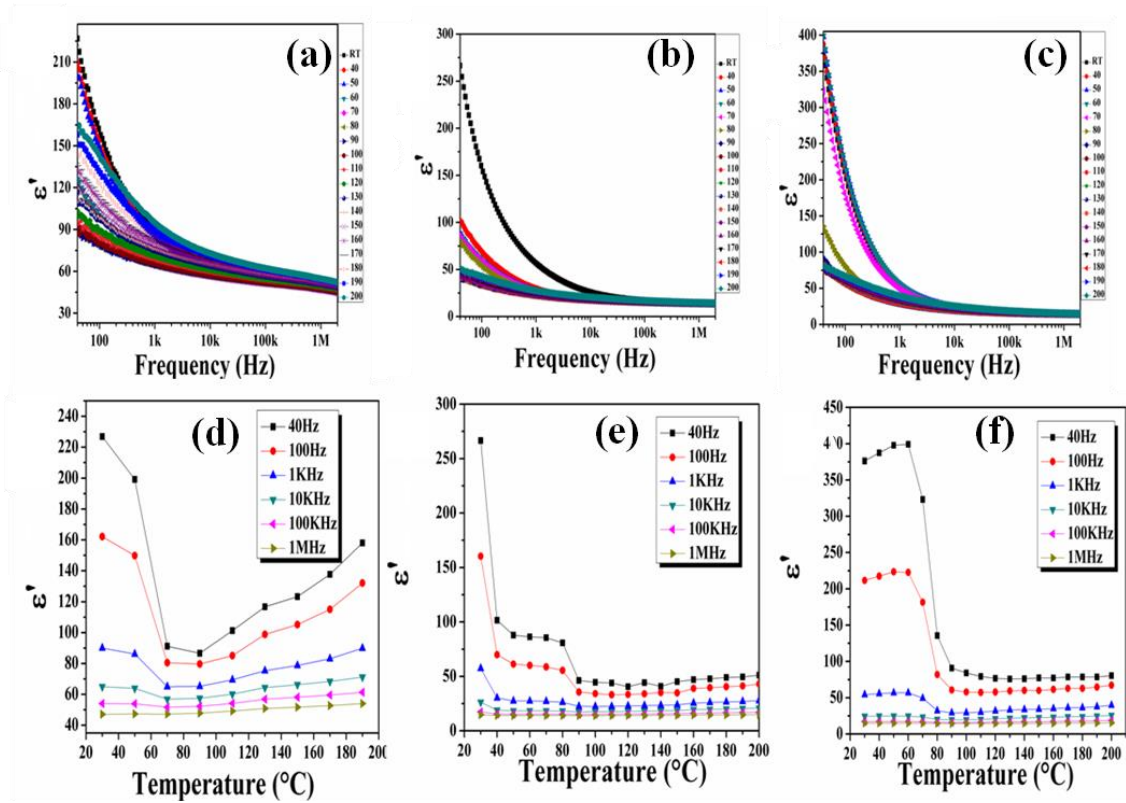
Figure 2.6. *Variation of dielectric constants for S1(Bulk), S2 (Intermediate), S3 (Nano) (a-c) with frequency, and (d-f) with temperature*

The samples in the form of pellets of 1 mm diameter were used to study the dielectric properties and ac conductivities under varying temperature conditions using the relation in equations 1.9 and 1.10 in Chapter 1. The values of the real part of the dielectric constant increased with a decrease in particle size, i.e., ε' for $S_1 < \varepsilon'$ for $S_2 < \varepsilon'$ for S_3. The nano-sized sample S3 acquired the highest permittivity value (~ 400), whereas its bulk counterpart S1 possessed the lowest permittivity (~ 225) at room temperature [30]. As suggested by the BET-BJH data the aspect ratio was highest for S3, which caused the creation of a larger number of nano-dipoles, the rationale behind the increase in electrical permittivity of S3.

The variation of ε' with the frequency (40Hz to 10MHz) of the applied field was studied for all samples [Figure 2.6(a-c)] at different temperatures (30- 200˚C). The dielectric constant of the samples decreased rapidly with the increasing field frequencies for all temperatures. Such behavior can be explained in terms of the Maxwell-Wagner interfacial polarization effect [31]. This type of polarization also has a good agreement with Koop's theory [28]. According to this theory, conductive grains are separated by non-conductive grain

boundaries, which is the key to dipole creation. These dipoles are responsible for low-frequency dielectric relaxation [25].

The variation of the dielectric constant with the temperature was studied in Figure 2.6(d-f). The dielectric constant generally decreased with an increase in temperature for low-frequency regions. The dielectric constant for S3 at a high temperature is nearly 8.5 which becomes lower (value nearly 3) at low temperature low frequency area. An increase in the number of dipoles, generated due to the separation between conductive grains and insulated grain boundaries, caused high dielectric values of the samples. With an increase in temperature, thermal agitation stimulated the charges to take part in the charge-hopping progression. The charge hopping mechanism eventually hindered the process of dipole production [32], resulting in the lowering of the permittivity values of the samples. However, at high frequencies of the applied field, the dipole creation temporally lagged behind the changes in the direction of the field.
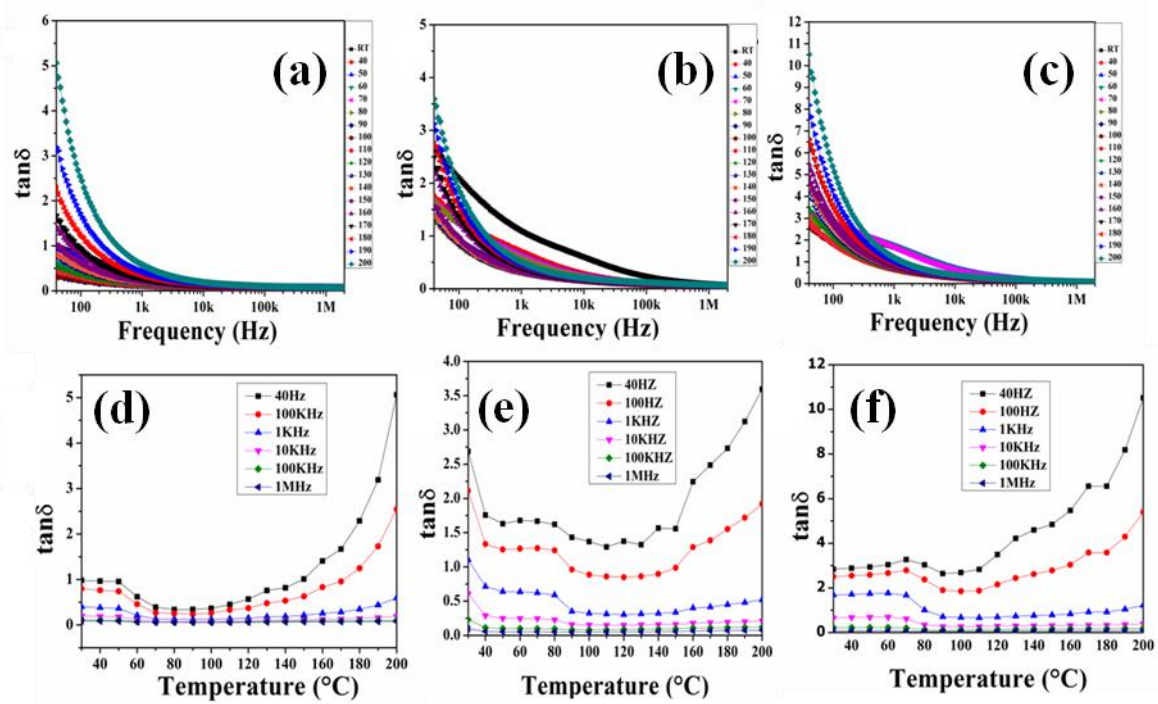
Figure 2.7. *Variation of tangent losses for S1 (Bulk), S2 (Intermediate), S3 (Nano) α-hematite (a-c) with frequency and (d-f) with temperature*

In the case of S1, ε' value further increased after 100 ^{0}C due to possible intervention of the impurities present in the sample [28]. On the other hand, for the nano-sized material S3, the value of ε' remained constant nearly up to 70 ^{0}C, and then decreased with further increase

in temperature which indicated appreciable stability of the sample S3. Due to nanonization, the quality of the material (sample S3) was boosted for its use as a storage material. The variation in tangent loss with frequency and temperature is plotted in Figure 2.7. At high frequencies, tangent loss was comparatively lower than that at low frequencies for the entire sample set. The high value of the tangent loss at the low-frequency region might be due to the charge lattice defect of space charge polarization [33]. Decrement of tangent loss with an increase in frequency can be explained by the Maxwell-Wagner-Sillars polarization effect [34]. The value of tangent loss became high as temperature increased, due to thermally activated charges, which were also responsible for a reduction in dielectric constant at high temperatures as mentioned above [35]. Thus, the variations in tangent loss for all the samples are in good agreement with high permittivity data.

To get a comprehensible idea of the conduction mechanism, the change in ac conductivity with frequency for all three samples was investigated. The graphical representation of ac conductivity in varying frequency ranges has been depicted in Figure 2.8(a-c). The ac conductivity was amplified with an increase in frequency which is a good agreement with Jonscher's universal power law [Figure 2.8(d)] [36]. The relation between ac conductivity (σ_{ac}) and frequency can be obtained from Jonscher's universal (equation 1.11) eqn. The value of 'n', obtained by plotting the $\ln\sigma$ vs $\ln\omega$ curve for each sample, was not exactly constant but varied within a small range of 0.3541 to 0.3677, which indicated that the samples were not perfectly Debye type [37]. At high frequencies, electrons became more energetic, and hence the mobility of electrons increased. The high mobility of electrons was the key to raising ac conductivity at higher frequencies for all samples [35].
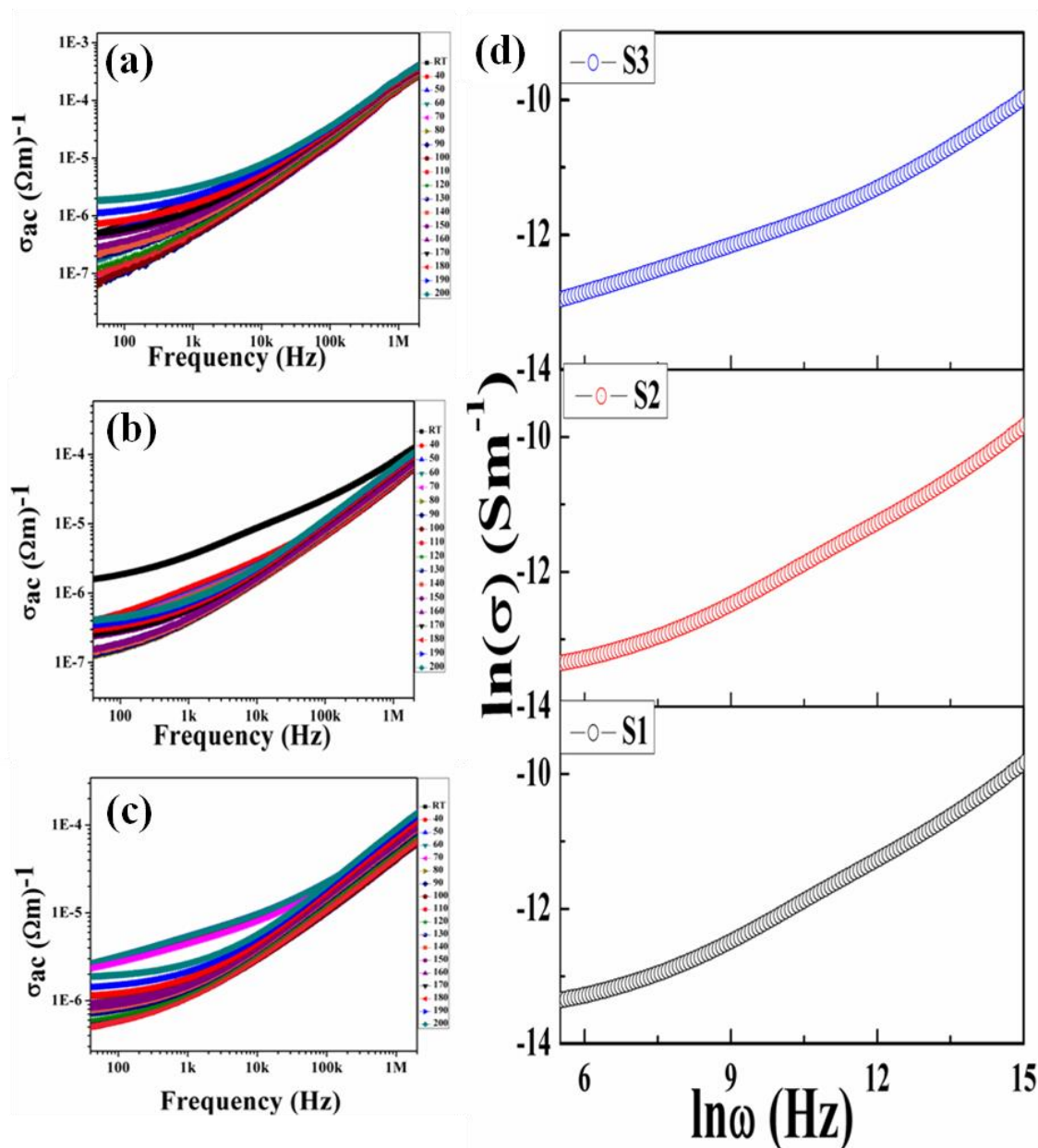
Figure 2.8. *Variation of ac conductivities with frequency(a-c) and corresponding Joncher's plot for S1 (Bulk), S2 (Intermediate), S3 (Nano) (d) Jonscher's plot*

2.4 Summary

This chapter describes a study on the synthesis of nanoparticles from an easily available natural hematite mineral α-Fe_2O_3 by adopting a facile top-down approach, without using toxic chemicals. The study revealed how a mere mechanical crushing and grinding process, which was not only environment friendly but also of low cost, could alter the morphology and particle size of the material at ambient temperatures. During the process of nanonization dielectric property was upgraded radically along with the purification of the material.

Enhanced surface-to-volume ratio played a pivotal role in amending the dielectric permittivity and AC conductivity of the material. Temperature dependence of dielectric property and ac conductivity indicated that the interfacial polarization was the predominant reason for upgrading these two imperative parameters in nano-sized samples. Moreover, high thermal stability and phase purity accompanied by a nominal tangent loss, specified that the nano-sized samples (S3) might be a potential candidate for fabricating low-cost, energy harvesting devices as they achieve excellent physicochemical properties after ball milling. As a result, natural hematite with a relatively high dielectric value confirms the increase in polarisation, which may be employed for piezoelectric energy harvesting by doping the S3 sample into the piezo-active membrane. Hence this might be a novel strategy for harvesting energy from natural materials in a cost-effective manner.

References

1. Harish, V., Ansari, M.M., Tewari, D., Yadav, A.B., Sharma, N., Bawarig, S., García-Betancourt, M.L., Karatutlu, A., Bechelany, M. and Barhoum, A., 2023. Cutting-edge advances in tailoring size, shape, and functionality of nanoparticles and nanostructures: A review. Journal of the Taiwan Institute of Chemical Engineers, 149, p.105010.

2. Song, J.H., Min, S.H., Kim, S.G., Cho, Y. and Ahn, S.H., 2022. Multi-functionalization strategies using nanomaterials: A review and case study in sensing applications. International Journal of Precision Engineering and Manufacturing-Green Technology, 9(1), pp.323-347.

3. Rane, A.V., Kanny, K., Abitha, V.K. and Thomas, S., 2018. Methods for synthesis of nanoparticles and fabrication of nanocomposites. In Synthesis of inorganic nanomaterials (pp. 121-139). Woodhead publishing.

4. Sohni, S., Nidaullah, H., Gul, K., Ahmad, I. and Omar, A.M., 2018. Nanotechnology for Safe and Sustainable Environment: Realm of Wonders. Khan, SB, Asiri, AM and Akhtar, K.(2018), Nanomaterials and their Fascinating Attributes–Development and Prospective Applications of Nanoscience and Nanotechnology, 2, pp.37-117.

5. Morris, R.V., Lauer Jr, H.V., Lawson, C.A., Gibson Jr, E.K., Nace, G.A. and Stewart, C., 1985. Spectral and other physicochemical properties of submicron powders of hematite (α-Fe2O3), maghemite (γ-Fe2O3), magnetite (Fe3O4), goethite (α-FeOOH), and lepidocrocite (γ-FeOOH). Journal of Geophysical Research: Solid Earth, 90(B4), pp.3126-3144.

6. Qureshi, A.A., Javed, S., Javed, H.M.A., Jamshaid, M., Ali, U. and Akram, M.A., 2022. Systematic investigation of structural, morphological, thermal, optoelectronic, and magnetic properties of high-purity hematite/magnetite nanoparticles for optoelectronics. Nanomaterials, 12(10), p.1635.

7. Anupama, A.V., Keune, W. and Sahoo, B., 2017. Thermally induced phase transformation in multi-phase iron oxide nanoparticles on vacuum annealing. Journal of Magnetism and magnetic Materials, 439, pp.156-166.

8. Rodriguez-Navarro, A.B., 2006. XRD2DScan: new software for polycrystalline materials characterization using two-dimensional X-ray diffraction. Journal of Applied Crystallography, 39(6), pp.905-909.

9. Bunaciu, A.A., UdriŞTioiu, E.G. and Aboul-Enein, H.Y., 2015. X-ray diffraction: instrumentation and applications. Critical reviews in analytical chemistry, 45(4), pp.289-299.

10. Chauhan, A. and Chauhan, P., 2014. Powder XRD technique and its applications in science and technology. J Anal Bioanal Tech, 5(5), pp.1-5.

11. Hanawalt, J.D., Rinn, H.W. and Frevel, L.K., 1938. Chemical analysis by X-ray diffraction. Industrial & Engineering Chemistry Analytical Edition, 10(9), pp.457-512.

12. Kril, C.E. and Birringer, R., 1998. Estimating grain-size distributions in nanocrystalline materials from X-ray diffraction profile analysis. Philosophical Magazine A, 77(3), pp.621-640.

13. Klug, H.P. and Alexander, L.E., 1974. X-ray diffraction procedures: for polycrystalline and amorphous materials (p. 992).

14. Hargreaves, J.S.J., 2016. Some considerations related to the use of the Scherrer equation in powder X-ray diffraction as applied to heterogeneous catalysts. Catalysis, Structure & Reactivity, 2(1-4), pp.33-37.

15. Chen, H., Chen, Y., Yu, J. and Williams, J.S., 2006. Purification of boron nitride nanotubes. Chemical physics letters, 425(4-6), pp.315-319.

16. Singh, S., Aswath, M.U., Biswas, R.D., Ranganath, R.V., Choudhary, H.K., Kumar, R. and Sahoo, B., 2019. Role of iron in the enhanced reactivity of pulverized Red mud: Analysis by Mössbauer spectroscopy and FTIR spectroscopy. Case Studies in Construction Materials, 11, p.e00266.

17. Darezereshki, E., 2011. One-step synthesis of hematite (α-Fe2O3) nano-particles by direct thermal-decomposition of maghemite. Materials Letters, 65(4), pp.642-645.

18. Ramis, G., Busca, G. and Lorenzelli, V., 1991. Low-temperature CO2 adsorption on metal oxides: spectroscopic characterization of some weakly adsorbed species. Materials Chemistry and Physics, 29(1-4), pp.425-435.

19. Brostow, W. and Datashvili, T., 2008. Chemical modification and characterization of boehmite particles. Chem. Chem. Technol, 2(6).

20. Saikia, B.J., Parthasarathy, G., Borah, R.R. and Borthakur, R., 2016. Raman and FTIR spectroscopic evaluation of clay minerals and estimation of metal contaminations in natural deposition of surface sediments from Brahmaputra river. International Journal of Geosciences, 7(7), pp.873-883.

21. Farmer, V.C., 1974. The infrared spectra of minerals. Mineralogical society monograph, 4, pp.331-363.

22. Saikia, B.J., Parthasarathy, G. and Sarmah, N.C., 2009. Fourier transform infrared spectroscopic characterization of Dergaon H5 chondrite: Evidence of aliphatic organic compound. *Nature and Science*, *7*(4), pp.45-51.

23. Saikia, B.J., Parthasarathy, G., Sarmah, N.C. and Baruah, G.D., 2008. Fourier-transform infrared spectroscopic characterization of naturally occurring glassy fulgurites. Bulletin of Materials Science, 31, pp.155-158.

24. Yeung, Z.L.L., Kwok, R.C.W. and Yu, K.N., 2003. Determination of multi-element profiles of street dust using energy dispersive X-ray fluorescence (EDXRF). Applied radiation and isotopes, 58(3), pp.339-346.

25. Roy, S., Maity, A., Mandal, P., Chanda, D.K., Pal, K., Bardhan, S. and Das, S., 2018. Effects of various morphologies on the optical and electrical properties of boehmite nanostructures. CrystEngComm, 20(40), pp.6338-6350.

26. Chanda, D.K., Das, P.S., Samanta, A., Dey, A., Mandal, A.K., Gupta, K.D., Maity, T. and Mukhopadhyay, A.K., 2014. Intertwined nanopetal assembly of Mg (OH) 2 powders. Ceramics International, 40(7), pp.11411-11417.

27. Chanda, D.K., Samanta, A., Dey, A., Das, P.S. and Mukhopadhyay, A.K., 2017. Nanoflower, nanoplatelet and nanocapsule Mg (OH) 2 powders for adsorption of CO 2 gas. Journal of Materials Science, 52, pp.4910-4922.

28. Roy, S., Bardhan, S., Pal, K., Ghosh, S., Mandal, P., Das, S. and Das, S., 2018. Crystallinity mediated variation in optical and electrical properties of hydrothermally synthesized boehmite (γ-AlOOH) nanoparticles. Journal of Alloys and Compounds, 763, pp.749-758.

29. Roy, S., Bardhan, S., Chanda, D.K., Maity, A., Ghosh, S., Mondal, D., Singh, S. and Das, S., 2020. Cu (II) and Gd (III) doped boehmite nanostructures: a comparative study of electrical property and thermal stability. Materials Research Express, 7(2), p.025020.

30. Chuprinko, D. and Titov, K., 2017. Influence of mineral composition on spectral induced polarization in sediments. Geophysical Journal International, 209(1), pp.186-191.

31. Koops, C.G., 1951. On the dispersion of resistivity and dielectric constant of some semiconductors at audiofrequencies. Physical review, 83(1), p.121.

32. Bardhan, S., Roy, S., Chanda, D.K., Das, S., Pal, K., Chakraborty, A., Basu, R. and Das, S., 2019. Microstructure and dielectric properties of naturally formed microcline and kyanite: a size-dependent study. Crystal Growth & Design, 19(8), pp.4588-4601.

33. Ganguly, S., Halder, K., Haque, N.A., Das, S. and Dastidar, S.G., 2015. A comparative study between electrical properties of bulk and synthesized nano material of zinc sulphide. American Journal of Research Communication, 3(3), pp.3-6.

34. Thakur, P., Kool, A., Bagchi, B., Hoque, N.A., Das, S. and Nandy, P., 2015. Improvement of electroactive β phase nucleation and dielectric properties of WO 3· H 2 O nanoparticle loaded poly (vinylidene fluoride) thin films. RSC advances, 5(77), pp.62819-62827.

35. Das, S., Das, S., Roychowdhury, A., Das, D. and Sutradhar, S., 2017. Effect of Gd doping concentration and sintering temperature on structural, optical, dielectric and magnetic properties of hydrothermally synthesized ZnO nanostructure. Journal of Alloys and Compounds, 708, pp.231-246.

36. Jonscher, A.K., 1981. A new understanding of the dielectric relaxation of solids. Journal of materials science, 16, pp.2037-2060.

37. Sudha, L.K., Sukumar, R. and Uma Rao, K., 2014. Evaluation of activation energy (Ea) profiles of nanostructured alumina polycarbonate composite insulation materials. Int. J. Mater. Mech. Manuf, 2(1), pp.96-100.

Chapter 3

Dye degradation and piezoelectric energy harvesting from hand tapping and water droplets using natural hematite-based self-poled piezo-responsive membrane

Chapter 3

Dye degradation and piezoelectric energy harvesting from hand tapping and water droplets using natural hematite-based self-poled piezo-responsive membrane

3.1 Introduction

The increasing global demand for energy, driven by population growth, economic expansion, and industrialization, has raised an impending energy crisis and thus serious concerns about associated environmental pollution [1]. Traditional energy sources are depleting rapidly, prompting a shift towards renewable alternatives like solar and wind energy. However, present renewable technologies confront difficulties such as inconsistency and inefficiency [2].

Another urgent issue caused due to industrialization and urbanization is wastewater which necessitates immediate attention. Solving the problems of toxicant bioaccumulation and biomagnifications in water bodies is the need of the day [3]. A sustainable approach to energy generation and waste management is immediately required, emphasizing reliability, cost-effectiveness, and eco-friendliness.

Piezo-responsive materials are becoming increasingly important for energy harvesting and wastewater treatment [4]. These materials utilize the piezoelectric effect, converting mechanical energy into electrical energy, aligning with current green technology trends. Various piezoelectric materials, including quantum dots, perovskite, metal oxide nanoparticles, and polymers, are employed for harvesting energy from mechanical stress [5]. Hence, this work focuses on developing a piezoelectric material, namely hematite (α-Fe_2O_3) doped polyvinylidene fluoride-hexafluoropropylene (PVDF-HFP-HFP). Hematite used herein has been collected directly from nature making this sample cost-effective, reusable, industrially feasible, and flexible. The role of this polymer nanocomposite material as a piezoelectric energy harvester and a piezocatalyst has been analyzed in this study.

Initially, the characteristics of this polymer nanocomposite (PVF5) have been studied by using X-ray diffraction (XRD), Field-Effect Scanning Electron Microscope (FESEM), Fourier transform infrared (FTIR) spectroscopy, etc. The nanocomposite exhibits significant piezoelectric polarisation, making it a suitable material for energy production by finger tapping and water flow. It also uses ultrasonic energy to generate reactive oxidant species, which are helpful in removing water pollutants such as Rhodamine B. The device's cost-

effectiveness and reusability make it a viable option for industrial and commercial applications that solve energy and environmental issues.
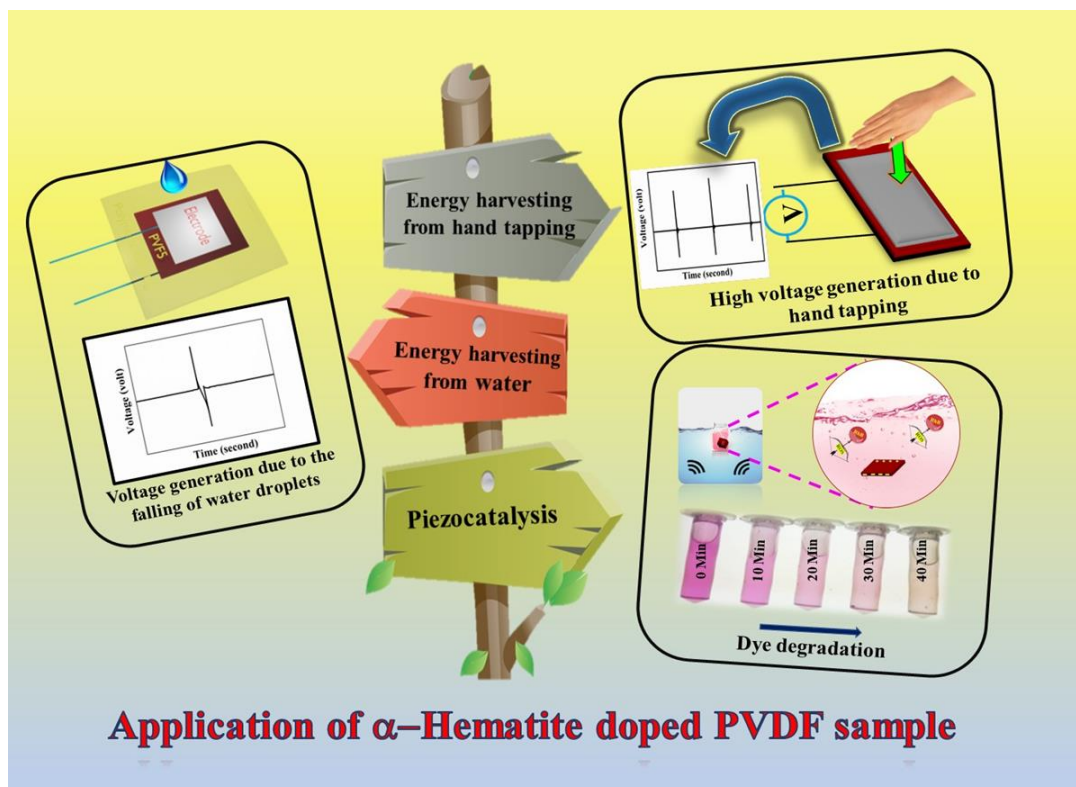
Figure 3.1 *Application of α-hematite doped PVDF-HFP membrane*

3.2 Experimental details

3.2.1 Material

The naturally formed hematite (α-hematite) was purchased from Bharat Engineering, Kolkata, India. Terephthalic acid, ethylenediaminetetraacetic acid disodium salt dihydrate (EDTA), polyvinylidene fluoride-hexafluoropropylene (PVDF-HFP-HFP), and p-benzoquinone (BQ) were purchased from Sigma-Aldrich. All the reagents used were of analytical grade. Rhodamine B (RhB) was purchased from Loba Chemie Pvt. Ltd and dimethylformamide (DMF) (HPLC grade) were purchased from Merck, India. Millipore water of 18.2 MΩ-cm resistivities has been used throughout the experiments.

3.2.2 Synthesis of flexible natural α-hematite mediated PVDF-HFP nanocomposite films

The nano form of natural α-hematite(rock mineral) was synthesized from natural hematite rock which has been mentioned elaborately in section 1.10.1 (Chapter 1). To prepare the polymer nanocomposite (PVDF-HFP-HFP/hematite), 0.5 mg PVDF-HFP-HFP was taken into a glass vial with 10 ml of DMF before the addition of 2.5 and 5 weight % of nano hematite to achieve a homogeneous mixture of the rock mineral-PVDF-HFP nanocomposite under 600 rpm for 3 h at 60^0C. A bare PVDF-HFP-HFP solution was also prepared without adding the hematite powder, maintaining similar experimental conditions. The solutions were then poured into clean Petri dishes and were dried at 70^0C to obtain the free-standing nanocomposite films (PVF0, PVF2.5, and PVF5).

3.3 Results and discussions

3.3.1 Physical characteristics of the natural rock and nanocomposite membrane

The structural aspects and the phase purity of the synthesized membranes along with the nano-sized natural hematite have been investigated using the X-ray diffraction (XRD) technique [6]. Since a naturally formed mineral sample has been used, purity determination is of utmost importance. Figure 3.2(a) shows well-matched experimental maxima over the theoretical maxima of natural hematite with the JCPDS card no 72-0469. The presence of any undesirable maxima [Figure 3.2(a)] validates the purity of the natural rock sample. The Rietveld refinement reveals that the unit cell dimensions are a=b= 5.03 Å and c= 13.75 Å respectively. Figure 3.2 (b) depicts the refined diffractograms along with the experimental one of the natural hematite and also shows the unit cell visualized from Vesta 3.4.4.

The XRD patterns of the hematite/PVDF-HFP-HFP nanocomposite films are shown in Figure 3.2 (c) and show characteristic peaks at 18.1° (020) and 39.3° (002), which corresponds to the non-polar α-phase and the prominent diffraction maximum at 20.7° (110) represents the polar β-phase of the samples. With the increase in hematite loading in PVDF-HFP-, the α-phase gradually diminishes, while the β-phase peak increases and becomes maximum for the PVF5 membrane [7]. Such enhancement of the electroactive β-phase is one of the significant parameters for the amplification of piezoelectric properties in the doped film
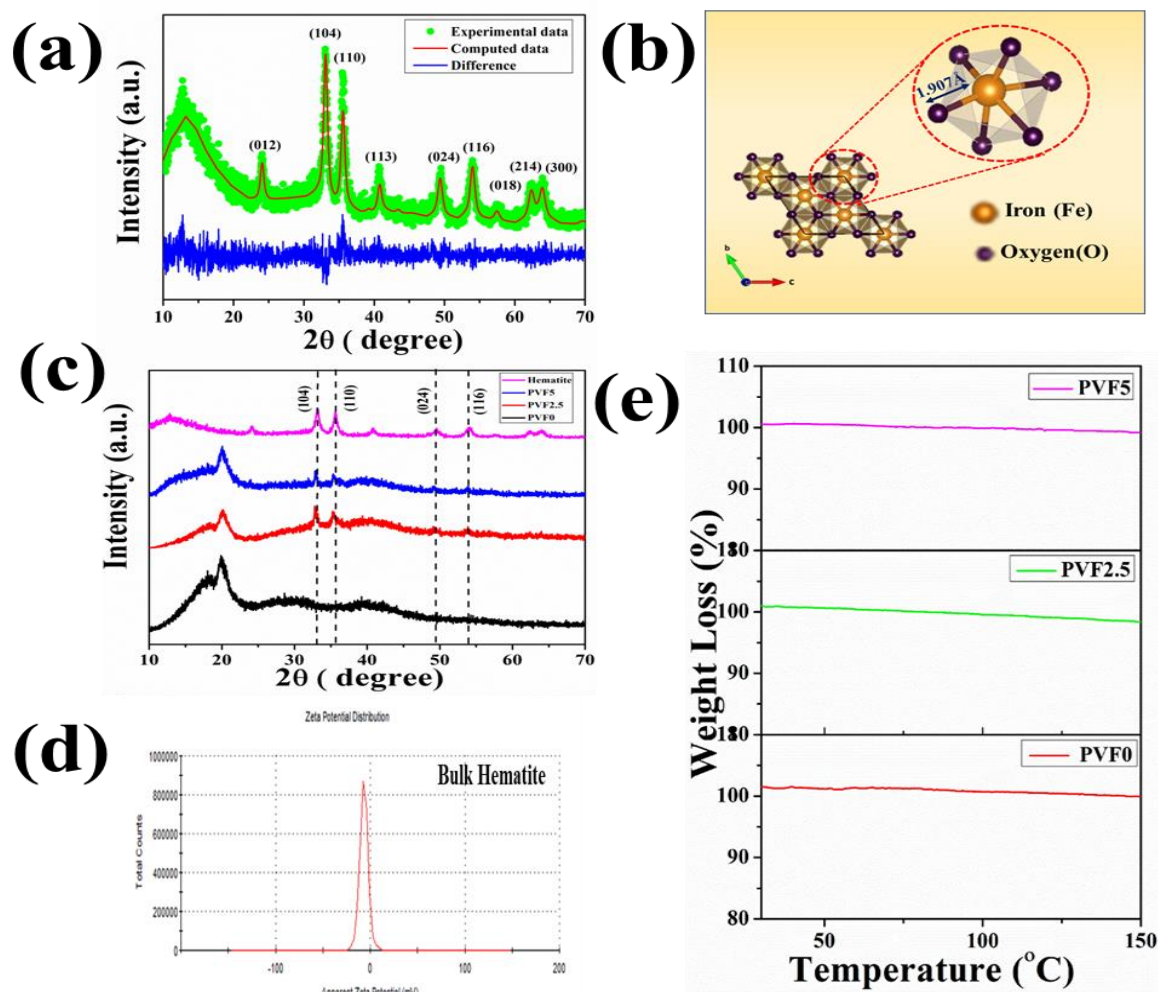
Figure 3.2(a) Computed and experimental XRD pattern of natural a-hematite (b) Unit cells of a-hematite along with bond lengths (c) XRD pattern of natural a-hematite, PVF0, PVF2.5, PVF5, (d) zeta potential of natural a-hematite, (e) Thermo-gravimetric analysis of PVF0, PVF2.5, PVF5

The morphological investigation from TEM micrographs [Figure 3.3(a)] reveals that the structure of natural hematite nanoparticles is relatively hexagonal, with an average particle size of around 50 nm. The particle size distribution of the hematite has been carried out by the ImageJ (V 1.8.0) software and is depicted in Figure 3.3(a). HRTEM [Figure 3.3 (b)] illustrates the d-spacing lines and the grains. From the d spacing line, the value of d space can be calculated. The d spacing value is 2.77 Å for the plane (1 0 4) and that for the plane (1 1 6) is 1.68 Å. Thus, these planes are clearly visible in the TEM images. The peak for the

plane (1 0 4) is visible in the X-ray diffractogram at $2\theta = 33^0$ and the peak at $2\theta = 54^0$ represents the plane (1 1 6) Figure 3.3 (b).

The detailed elemental constitution of the natural hematite nanoparticles has been determined from the EDAXS spectra, which confirms the presence of iron (77.73 %) and oxygen (22.27 %) shown in Figure 3.3(c) This further confirms the high purity of the hematite nanoparticles. The morphological features of the nanocomposite membranes have also been studied by using FESEM. As shown in Figure 3.3 (d), pure PVDF-HFP membrane has a smooth and uniform spherical texture, while hematite doping causes a rough and slightly wrinkled surface, especially in PVF5 [Figure 3.3 (f)]. The β-phase nucleation increases in PVF5 due to more doping of hematite. The particles in the PVDF-HFP matrix showed nearly well and uniform distributions [Figure 3.3 (e-f)] of hematite in the films which triggered the initiation of the process of β-phase formation through electrostatic interaction between CH_2-CF_2 and hematite.
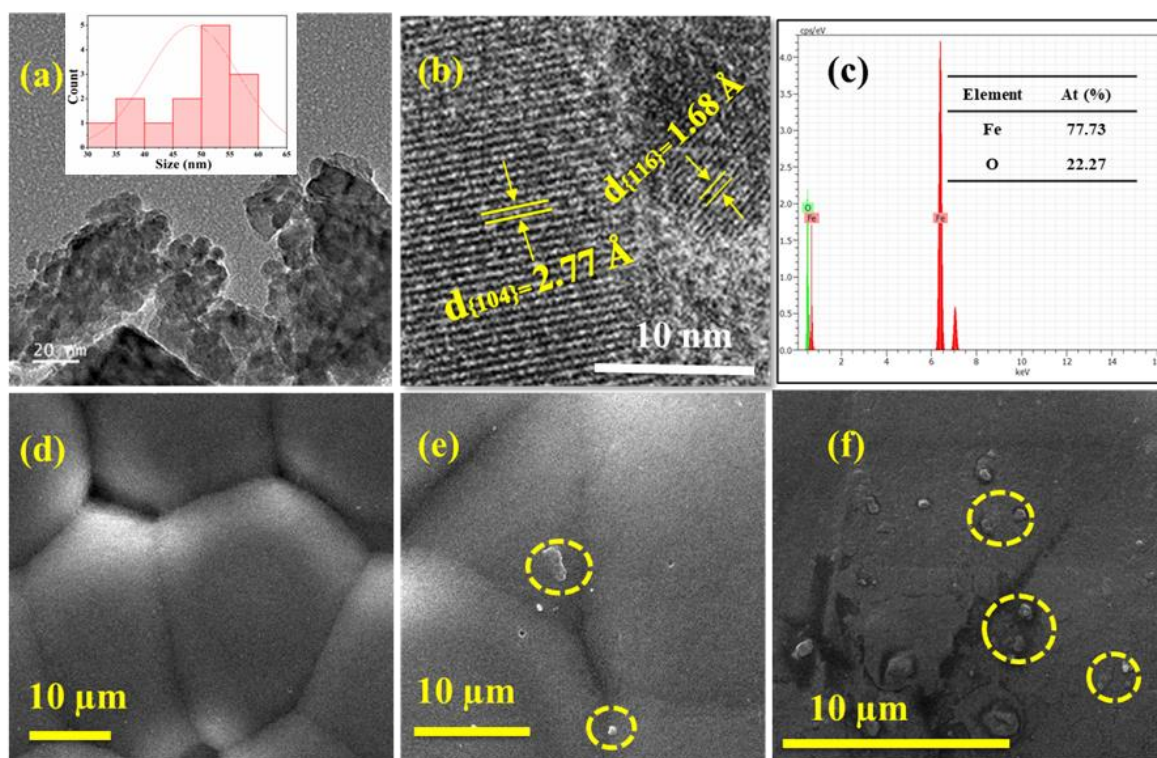
Figure 3.3 *(a) TEM image of hematite nanoparticles and their size distribution, (b) HRTEM micrographs of natural a -hematite, (c) EDX images showing verifying the purity of a -hematite, (d-f) SEM micrographs of PVF0, PVF2.5, PVF5 respectively*

The bonding networks of the nanocomposite films were obtained from FTIR spectra, [Figure 3.4(a)] Sharp absorption peaks at 488 cm^{-1} (CF$_2$ waging), 533 cm^{-1} (-CF$_2$bending), 616 cm^{-1}, and 765 cm^{-1} (-CF$_2$ bending and skeletal bending), 794 cm^{-1} and 975 cm^{-1} (-CH$_2$ rocking) were observed in pure PVDF-HFP film due to the α-phase of the film. These peaks decreased gradually in PVF2.5 and PVF5, which confirms the decrement of the α-phase of pure PVDF-HFP [8]. The peaks at 481 cm^{-1} (-CF$_2$ deformation), 510 cm^{-1} (-CF$_2$ stretching), 602 cm^{-1} (-CF$_2$ waging), and 840 cm^{-1} (CH$_2$) were found in all of the three films but increased in PVF2.5 and PVF5 successively which verify the formation of electroactive nucleation of β-phase in PVF2.5 and PVF5. The presence of a prominent absorption band at 1274 cm^{-1} in PVF5 confirmed significant enhancement of β-phase. The presence of a peak at 1234 cm^{-1} in pure PVDF-HFP was due to the γ phase, which diminished in PVF5, thus validating the reduction of the γ phase in PVF5. Hence, the presence of absorbance peaks at 510 cm^{-1}, 840 cm^{-1}, and 1274 cm^{-1} corroborated the formation of β polymorph in PVF5 [9].

The β-phase for PVF5 calculated from the relation (equation 1.8, Chapter 1) was found to be 80.2 % while in the case of pure PVDF-HFP, it was 60.8 % as shown in Figure 3.4 (b). The possible design after incorporation of 5% α-hematite i.e. PVF5 is shown in Figure 3.4 (c) signifying the orientation of the H-F bond of pure PVDF-HFP forming the highest β-Phase in PVF5.

Thermal stability is a significant parameter for a device for real-life and commercial applications, hence thermo-gravimetric analysis was performed to evaluate the percentage of mass loss with variation of temperature. Mass losses decreased with the increase in doping of natural hematite. In the case of PVF5, the loss was negligible (~1.36 %) while for PVF0 and PVF2.5 the losses were 2.65 % and 2.56 % respectively [Figure 3.2 (e)]. Therefore, PVF5 can be efficiently used for piezoelectric application even at high temperatures up to 150 ºC.

The zeta-potential value of the natural hematite nanoparticles was found to be -7.23 mV [Figure 3.5 (a)]. The negative surface charge of the hematite increased with the decreasing size and turned out to be maximum in its nano dimension [Figure 3.2 (d)]. This negative potential attracted the electropositive –CH$_2$ moiety of the PVDF-HFP and promoted a better β-phase formation in the nanocomposite membrane by flipping the –CH$_2$ and –CF$_2$ groups in opposite directions with increasing natural rock percentage. It has been observed that up to a critical incorporation limit of hematite, the polar β-phase increased (maximum at 5% doping) and then decreased with further increase in dopant percentage in the composite

matrix (decreased at 7.5% doping in A.1.1) due to the presence of excessive negative surface charge.
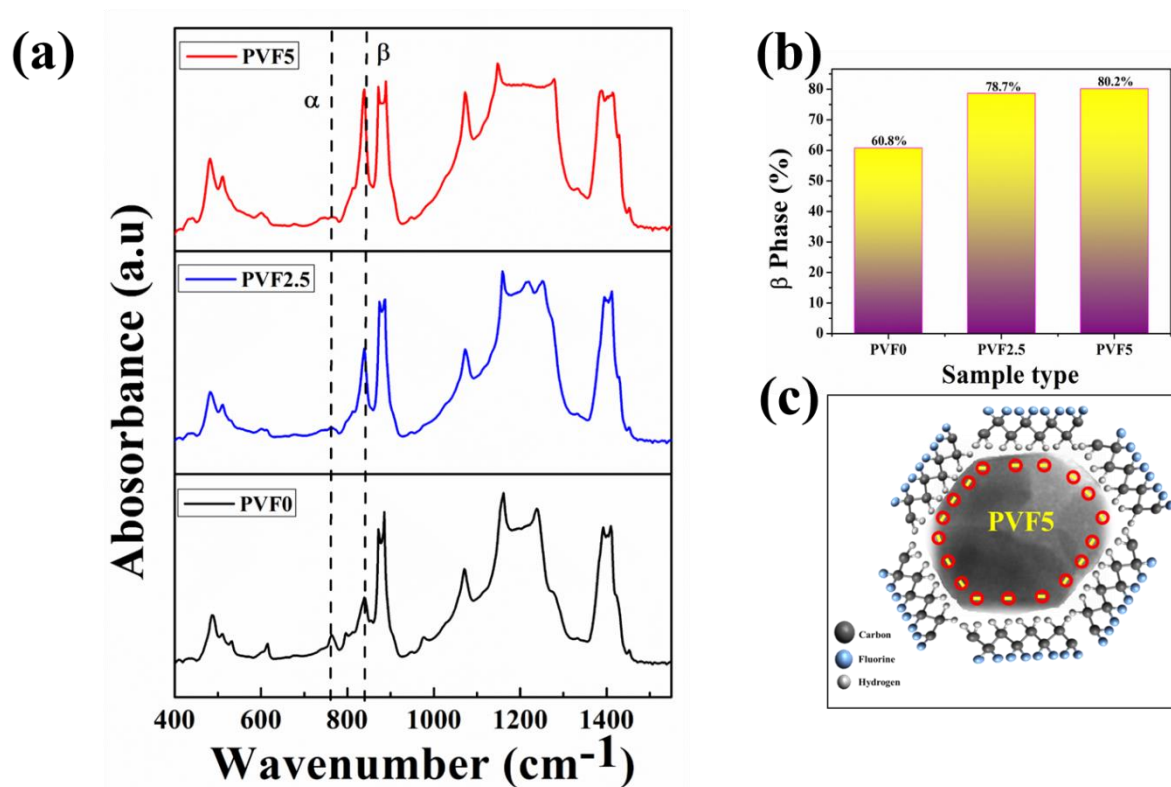
Figure 3.4 (a) FTIR spectra, (b) β-Phase of sample PVF0, PVF2.5, PVF5, (c) Orientation of H-F bond of pure PVDF-HFP forming highest β-Phase in PVF5

3.3.2 Electrical properties, theoretical polarization, piezoelectric coefficient of the membrane

The purpose of this work was to investigate the dielectric permittivity and the tangent loss of the material to estimate the storage capacity of the material [10]. The device was fabricated using a 1×1 cm^2 of the nanocomposite membrane, with aluminum electrodes and copper wires on both sides of the membrane. The electrical properties of the membrane were investigated by using a HIOKI, IM 3536 LCR meter, maintaining a bias voltage of 0.5 V in a varying frequency region of 40Hz to 1 MHz. The dielectric constants were calculated using the formula (equation 1.9, 1.10 in Chapter 1), and the values were 17, 9.1, and 6.7 for samples PVF5, PVF2.5, and   PVF0 respectively [Figure 3.5 (b), 3.5(d)]. The increase in the doping percentage of natural rock material in the PVDF-HFP matrix enhanced the

polarization and polar β-phase which was depicted by FTIR spectroscopy. It was also observed that the dielectric constant decreased with an increase in frequency. The dipoles could not rapidly change their orientations by the change in field direction in case of high frequency and thus the dielectric permittivity reduced with frequency. This can be well explained by the effect of Maxwell-Wagner polarization[11] [27].

The tangent loss was calculated and plotted with varying frequencies in Figure 3.5 (c). The dielectric constant was higher than that of others at the same frequency whereas the value of the tangent loss at 10Hz for PVF5 was lower than in other samples Figure 3.5 (e).

The piezoelectric coefficient (d_{33}) is one of the important properties that play a significant role in piezoelectric property of a substance. It has been calculated from the relation below [12]

$$d_{33} = \left(\frac{V \times C_P}{F}\right) \tag{3.1}$$

where V, C_P, and F are the output voltage, the capacitance of the sample, and the imparting force respectively. The d_{33} values were found to be 37.36 pC/N, 6.45pC/N and 3.27pC/N for PVF5 , PVF2.5 and PVF0 respectively, shown in Figure 3.5(f). Such a high d_{33} value made the PVF5 nanocomposite membrane a potential candidate for piezoelectric energy generation [13].

The density functional theory (DFT) has been employed to explore the theoretical value of polarizability [14]. Avogadro v.1.2.0 software package has been used to design the model of PVF0 and PVF5 membrane and Orca v.4.2 software has been applied for frequency and geometrical optimization [30]. B3LYP with 6-311G* basis set and RIJCOSX auxiliary basis set have been used for the simulation purpose. Analysis of DFT parameters indicated that the PVF0 membrane (i.e. without doping) had electronic energy -1386.073 whereas PVF5 had electronic energy -1386.094 which manifested the piezoelectric nature of the material. The isotropic polarizability also enhanced from 107.423 Cm^2V^{-1} (in PVF0) to 108.107 Cm^2V^{-1} in the case of PVF5. Hence the increased polarization validated the result obtained from FTIR i.e. the enhancement of β-phase in PVF5 than PVF0.
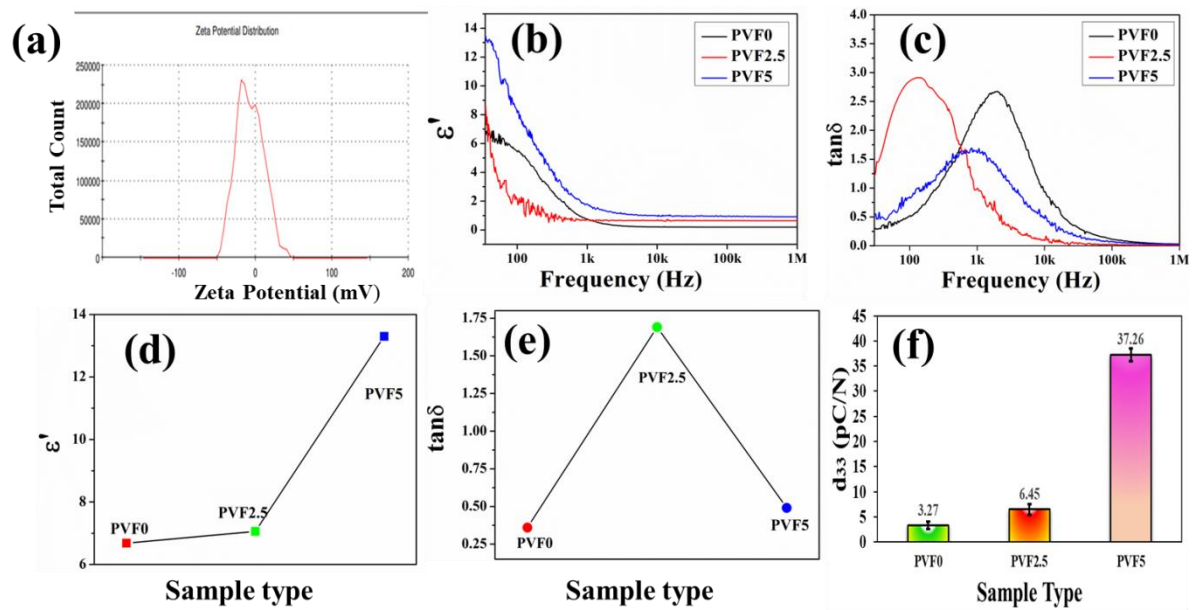
Figure 3.5 *(a) Zeta potential of α-hematite nanoparticles, (b)Variation of dielectric constant, and (c) Tangent losses with frequency (d), (e) Comparison of dielectric constant and tangent losses respectively at 10Hz of sample PVF0, PVF2.5, PVF5, (f) Comparison of the value of piezoelectric constant for sample PVF, PVF2.5, PVF5*

3.3.3 Generation of piezoelectricity by the nanocomposite membrane

3.3.3.1 Fabrication of the energy harvesting device

The piezoelectric energy harvesting device was developed using the PVF5 nanocomposite membrane as it showed the highest polar β- phase, maximum isotropic polarizability, and promising piezo-coefficient (d_{33}). A 2 cm × 2 cm of the PVF5 flexible membrane [Figure 3.6 (a)] was placed between aluminum electrodes attached with copper wires as represented in Figure 3.6 (b) The entire sandwiched structure was covered with a polyethylene terephthalate (PET) jacket to protect the device from any kind of damage.
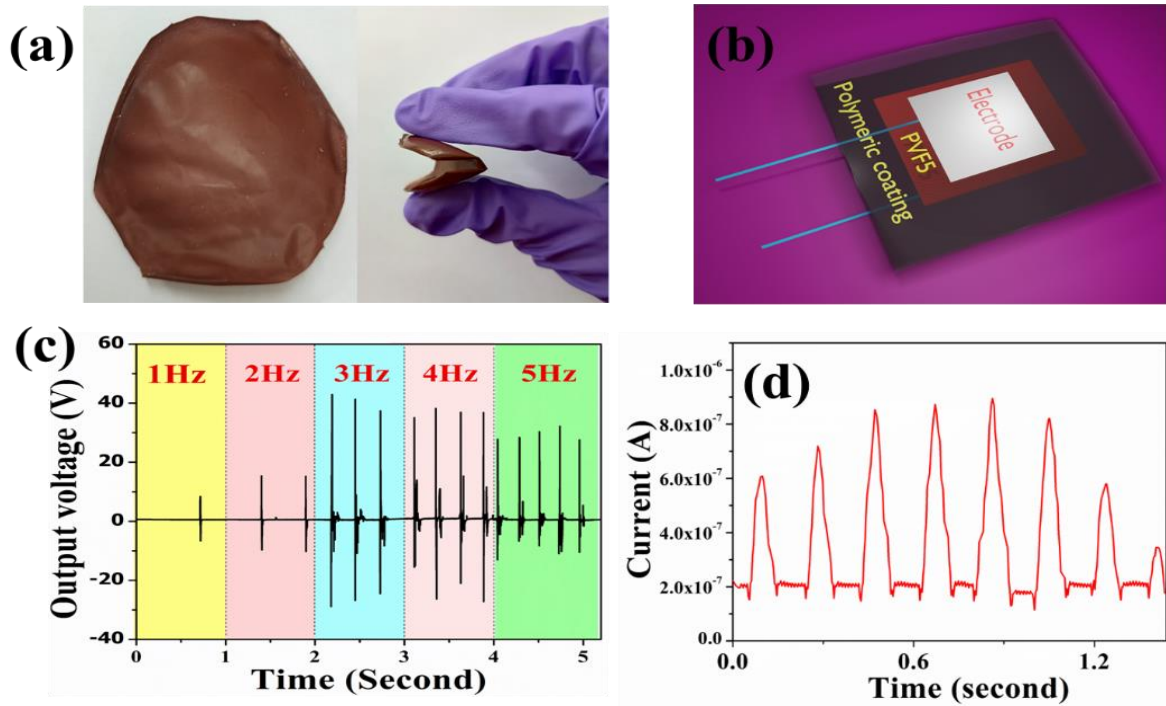
Figure3.6 *(a) PVF5 film along with bending, (b) Formation of the device with PVF5 film, (c) Open circuit voltage at a different frequency, (d) Short circuit current due to hand tapping on PVF5 device*

3.3.3.2 Piezoelectric energy harvesting due to hand tapping

A Keysight digital storage oscilloscope equipped with an Agilent N2862B 10:1 passive probe was used to measure the piezoelectric open circuit voltage. The output voltage was recorded for different frequencies under periodic hand (palm) tapping applying a periodic tapping force of 14.99 N. The output voltage increased gradually with increasing frequency from 1Hz to 5Hz in Figure 3.6 (c). However, at the 5 Hz frequency, the voltage decreased slightly. As the frequency increased the device did not get enough releasing time to go back to the initial stage.

The highest open-circuit voltage was 42V at 3Hz frequency [Figure. 3.6 (c)]. The force calculation has been depicted in Figure 3.7. Moreover, at 3 Hz frequency, the corresponding short circuit current was 0.898μA, shown in Figure 3.6 (d), which was measured by a DAQ6510 multimeter system, Keithley and the instantaneous power density turned out to be approximately 1328 μW/cm^3. This instantaneous power density (P) was calculated from the relation

$$P = \frac{V*I}{v} \tag{3.2}$$

where V, I, and v are the instantaneous voltage, current, and volume (2X2X.0071 cm^3) of the piezoelectric membrane inserted in the device respectively. This is a significantly high value for the natural rock-based piezoresponsive device. The power density was obtained due to the combined effect of strain that changed the polarization in the piezoelectric film, which resulted in the generation of piezoelectric potential due to the transition of electrons and holes to different electrodes and the continuous finger tapping force produced more strain helping in generation of potential differences continuously. These are the reasons for developing piezo-voltage as well as the current [15].

3.3.3.3 Piezoelectric energy harvesting from water flow

Besides finger tapping, water flow-mediated energy generation capabilities of the device were studied herein. It was noticed that falling water drops on the film induced piezo-voltage. The open circuit voltage also increased gradually, as the height increased progressively. The studies showed that values of the piezo-voltages were 0.6 V, 1V, and 1.5V when water drops fell from heights of 18cm, 36cm, and 72cm respectively [Figure 3.8(a)]. Such a phenomenon could be ascribed to the increasing stress on the device due to the falling water, which increased with falling height as the pressure is directly proportional to height. The forces for these three different heights were found to be 6.56 N, 14.6 N, and 20.05 N respectively, which have been calculated from the equation stated below [16]. The imparting pressure was analyzed by combining the pulse term and gravity. From the kinetic energy and momentum conservation theory, the equation can be written as

$$\frac{1}{2}mv^2 = mgh \tag{3.3}$$

$$(F - mg)\Delta t = mv \tag{3.4}$$

$$P = \frac{F}{A} \tag{3.5}$$

Where m is mass, h is height, v is the maximum velocity, A is the area of the electrode, F is contact force of hand palm and water in case of water flow, Δt is the period i.e full-width half maxima from output voltage vs time graph (Figure 3.7), g is gravitational acceleration= 981cm/s^2, h is 11 cm,vis 1.66 m/s, A is 2 cm x 2 cm and Δt is 0.002 sec.
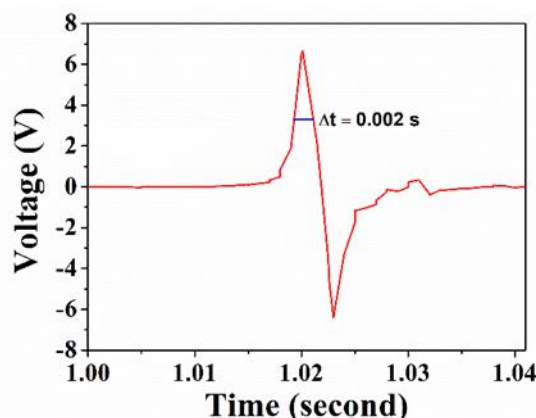
Figure 3.7 *Time vs voltage curve shows full width at half maximum (Δt)*

Also, the short circuit instantaneous currents were measured for heights 18cm, 36 cm, and 72 cm, and the maximum currents were found to be 0.15 µA, 0.19 µA, and 0.28 µA correspondingly [shown in Figure 3.8 (b)]. In the case of water falling from different heights, the device experienced different external forces due to the height variation which developed polarization [17].

Similar experiments were performed for three different types of water such as distilled water, drinking water, and tap water falling from a fixed height of 36 cm to check whether the physical/chemical parameters of water had any contribution to its piezo property. The induced piezoelectric voltages for these three different water types are depicted in Figure 3.8 (c). It was noticed that voltage generation was highest (4.4V) in the case of tap water, which had a high TDS (total dissolved solids) value of around 1867 ppm whereas the TDS values of drinking water and distilled water were 142 ppm and 2 ppm respectively, measured using a Hanna (HI991300). The dissolved solids in the water enhanced the pressure on the device which helped in increasing the voltage. The voltages due to distilled water, drinking water, and tap water were found to be 0.2V, 1V, and 4.4V respectively under a similar experimental setup. It is quite obvious that for different liquids, the TDS value varied which resulted in a change in pressure acting on the device. For that very reason, the polarization effect which creates the piezoelectric voltages was higher in the case of high TDS liquid
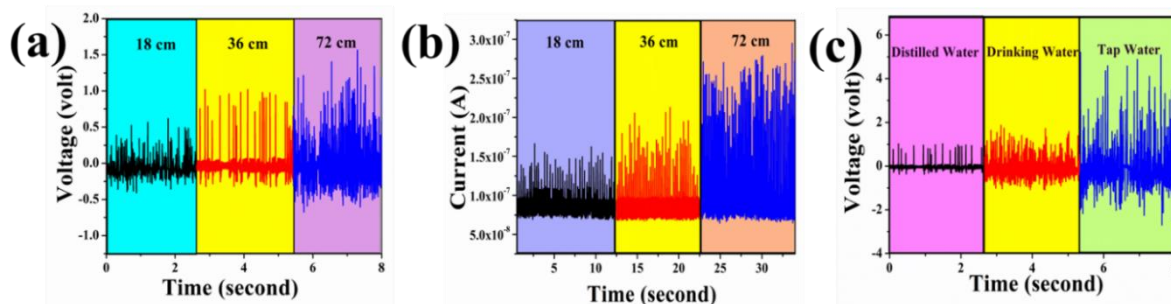
Figure 3.8 *(a-b) Open circuit voltage and short circuit current caused by falling water from three different heights, (c) Open circuit voltage due to three different types of water falling on the device*

3.3.4 Organic dye decomposition using piezocatalysis effect

Piezocatalysi is one of the advanced and convenient methods used for the removal of hazardous materials from wastewater [18]. Since PVF5 possesses the highest β-phase, isotropic polarizability, and piezoelectric coefficient, it was employed for piezocatalytic degradation of toxic dyes. In a typical experiment, a PVF5 membrane of 2cm x 2cm dimension was taken in a glass vial containing 15 mL of 2.5 ppm of Rhodamine-B solution and was exposed to the ultrasound having a frequency of 33 kHz in a bath sonicator (Telsonic Ultrasonic Bath Sonicator). 2 mL of the solution was taken out in every 10-minute interval, to observe the kinetics of the degradation. Before starting ultrasonication, the control absorption experiment was carried out. In this experiment, the PVF5 membrane and other samples were taken in different glass vials containing RhB solution and placed in a dark room for 40 min. The degradation due to adsorption was nearly 7.02% in the case of PVF5 whereas after ultrasonication it increased radically to 94.1% [Figure 3.9(a)]. Several control experiments were performed to confirm the degradation process. The percentage of dye degradation in pure hematite nanoparticles-dye solution, pristine PVDF-HFP-dye solution and only dye were 16.4%, 0.51%, and 0% respectively due to adsorption whereas utilizing ultrasonic vibration the degradation efficacy became 51.8 %, 40.3%, and 16.4% respectively Figure 3.9 (b-c). This suggests that the PVF5 membrane shows a promising piezocatalysic dye degradation efficacy. The percentage of efficiency of piezo degradation (η) is calculated by the following relation

$$\eta = \frac{c_0 - c}{c_0} \times 100\% \tag{3.6}$$

It is observed that the pink dye gradually became colorless under ultrasonic stimulation and almost reached full transparency within 40 minutes of stimulation. The absorbance spectra of the entire set of solutions were recorded using a Lambda 25, Perkin Elmer UV-Visible spectrophotometer, as depicted in Figure 3.9 (a). The characteristic UV absorption peak for RhB at λ=554nm, experienced a drastic quenching with time, elucidating the consequence of external ultrasound treatment in dye degradation efficacy. Herein, the dye degradation efficiency of the piezocatalytic PVF5 membrane has been calculated directly from the degradation kinetics, which suggests almost 94.1% of RhB degradation resulted within 40 minutes of ultrasound treatment. Such a high degradation efficacy by utilizing a natural rock mineral (hematite) is quite significant and unexplored till date.

The reaction rate constant of the piezocatalysis has been calculated from the relation given below [19],

$$\ln(C_0/C) = kt \tag{3.7}$$

Where C_0 and C are the initial and final concentration of RhB, k is the reaction rate constant and t is time. The reaction rate constant is 0.075 min^{-1} for PVF5. Kinetic rate constants for hematite powder, PVF0, PVF5, and Control (only RhB) are 0.01274 min^{-1}, 0.01158 min^{-1}, and 0.07495 min^{-1} respectively [Figure 3.9(i)].

Piezocatalysis can occur in two possible ways that can activate the catalytic chain reaction and degrade dye which has been discussed in section 1.8.1 (Chapter 1). In this work, the screening charge effect played a vital role in the degradation of dye by piezocatalysis. Thus, studies were performed to investigate the dominance of reactive radicals, which initiate the dye degradation process [20]. Herein, a scavenging experiment was also carried out. In a typical experiment, silver nitrate (AgNO$_3$), ethylenediaminetetraacetic acid (EDTA), p-benzoquinone (BQ), and tertbutanol (TBA) were utilized as scavengers of electron (e$^-$), hole (h$^+$), superoxide radicals ($\bullet$O$_2^-$) and hydroxyl radicals ($\bullet$OH) respectively [21-22]. The addition of an electron, hole, superoxides, and hydroxyl radical's scavengers hindered the degradation activity by 26.23 %, 15.53 %, 23.53 %, and 48.8 %, respectively confirming the effectiveness of electron, superoxides, and hydroxyl radicals for decomposition of RhB dye. It was furthermore observed that the degradation of dye reduced significantly due to the addition of TBA which ensures the presence as well as the dominance of hydroxyl

(•OH) radicals among all others. Like BQ, Silver nitrate also suppressed the degradation process, which confirms the presence of other
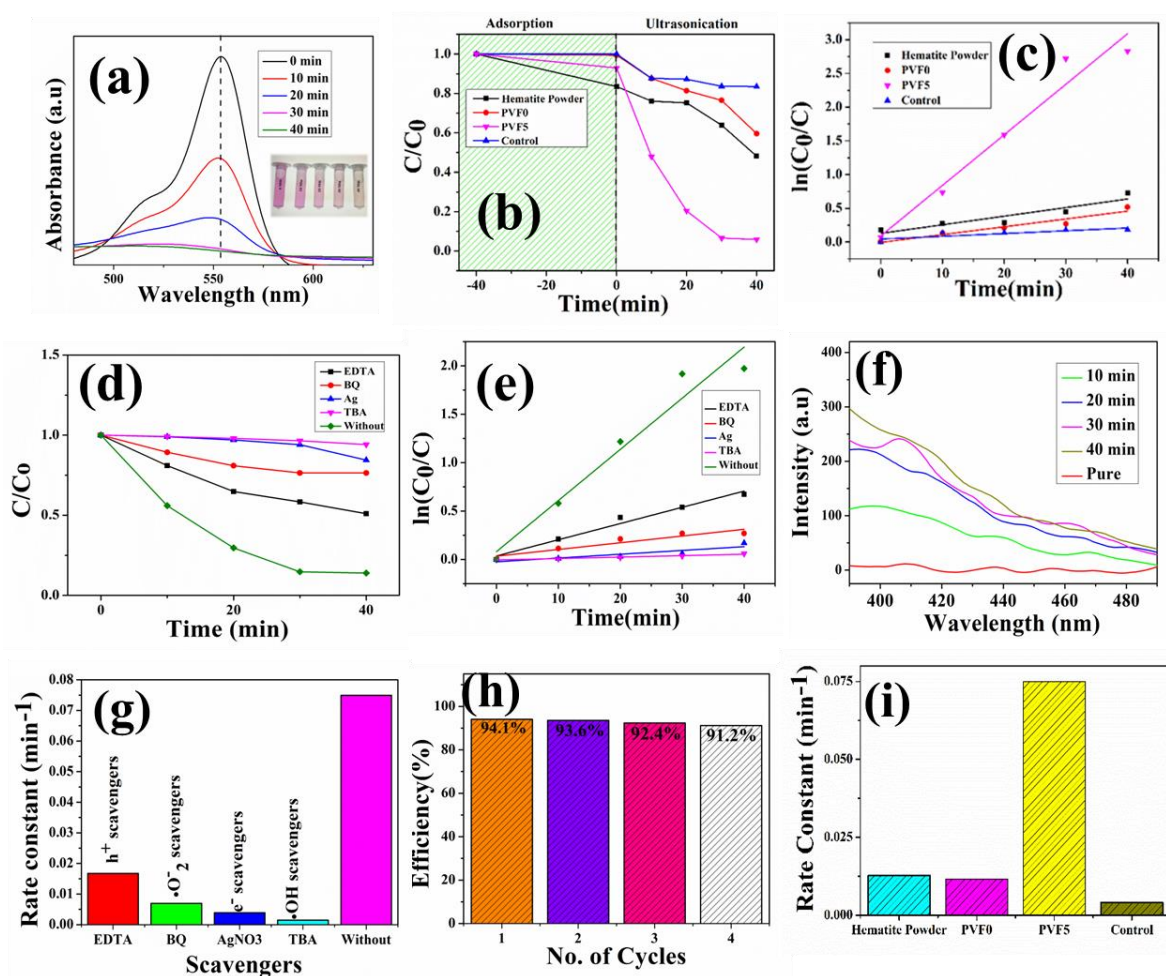
Figure 3.9 *(a) UV-Vis spectra presenting the dye degradation and decoloration of Rhodamine B (RhB) using the piezo catalyst PVF5, (b)Adsorption as well as Ultrasound-assisted degradation of RhB (C/C₀) varying hematite powder, PVF0, PVF5, Control(only RhB) (c) Plots of ln(C₀/C) with treatment time for hematite powder, PVF0, PVF5, Control(only RhB) (d) Ultrasound-assisted degradation of RhB (C/C₀) representing the Scavenging experiments in presence of different oxygen species and showing •OH radicals as one of the main species for piezocatalysis,(e) Plots of ln(C₀/C) with treatment time for the scavenging experiment (f) Demonstration of formation of hydroxyl radical due to piezo-electric effect as supported by an increase in fluorescence intensity of 2-hydroxyterephthalic acid (g) Kinetic rate constant for degradation of RhB due to different scavengers (h) Efficiency of piezo catalytic decomposition after each cycle (i) Kinetic rate constants for hematite powder, PVF0, PVF5 and Control (only RhB)*

radicals such as $\cdot O_2^-$, and e^- which are also effective for dye degradation whereas mixing the scavengers of h^+ i.e. EDTA lowers the reaction rate constant significantly. The rate constant (K) due to the addition of $AgNO_3$, EDTA, BQ, and TBA became 0.0039 min^{-1}, 0.0167 min^{-1}, 0.0069 min^{-1}, and 0.0014 min^{-1} respectively while the rate constant without scavenger was 0.075 min^{-1} which corroborates the inference that the addition of scavengers slows down the rate of catalysis. The rate constant for each scavenger is represented by the bar chart shown in Figure 3.9 (g). The degradation rate of the dye after adding up scavengers is shown in Figure 3.9 (d). Whereas, Figure 3.9 (e) depicts the kinetics of the catalysis under different scavengers.

Moreover, a trapping experiment was performed to confirm the formation of $\cdot OH$ radicals [23] where terephthalic acid was used as a trapping agent of $\cdot OH$ radicals which rapidly reacted with the $\cdot OH$ to form a fluorescent product 2-hydroxy terephthalic acid [24-25]. The formation of the fluorescent product was confirmed by the photoluminescence experiment, which showed the fluorescent peak of the material at 425 nm [Figure 3.9 (f)]. This peak increased gradually and substantiated the formation and increase of $\cdot OH$ radicals with reaction time. Hence, $\cdot OH$ radical is one of the major reactive species in our experiment for dye degradation.

The catalytic recyclability of the membrane (PVF5) was tested rigorously by utilizing the same membrane for four different catalytic cycles. It was found that even after four complete catalytic cycles, the dye degradation efficacy of the membrane remained at nearly 91.2% [Figure. 3.9(h)]. Hence, the consistency, reusability, durability, and stable efficiency indicate that the device may be beneficial for real-life applications.

3.4 Summary

In this chapter, we have explained the process of constructing natural hematite doped PVDF-HFP film with different percentages of doping concentration and propose its application as a piezoelectric energy harvesting equipment and its use for dye degradation using the piezocatalysis property of the material. The performance of the natural NP-based film PVF5 as the piezoelectric generator is outstanding. Even falling the droplets of distilled water onto the device can generate a voltage of up to 1V. In this work, the performance of the fabricated device as a voltage generator has been tested using three different types of droplets distilled

water, drinking water, and tap water. The droplet of tap water has generated the highest voltage which is nearly 5V. We also studied the voltage variation with the change in height of droplets falling and observed that the voltage increased with the height of the droplet falling. Thus, the device possesses the capability to generate voltage from raindrops. The highest obtained output voltage was 42V and the current was 0.898μA due to continuous tapping at frequency 4Hz. The instant power density is 1328 $\mu W/cm^3$ which is an excellent value. The device can also generate voltage due to the sonication. The piezoelectric property of the material has been used for piezo catalysis purposes to degrade dye i.e. RhB solution. The degradation of this dye by piezocatalysis is quite efficient and visible after 40 min. The efficiency of dye degradation is about 94.1% in 40min which is outstanding for any natural-based film. Hence, this chapter depicts the possible use of natural hematite NPs doped biodegradable PVDF-HFP film, as a nanocomposite-based piezoelectric energy harvester, and dye degradation agent using piezocatalysis.

References

1. Coyle, E.D. and Simmons, R.A., 2014. Understanding the global energy crisis. Purdue University Press.

2. Ayres, R.U. and Ayres, E.H., 2009. Crossing the energy divide: moving from fossil fuel dependence to a clean-energy future. Pearson Prentice Hall.

3. Walker, D.B., Baumgartner, D.J., Gerba, C.P. and Fitzsimmons, K., 2019. Surface water pollution. In Environmental and pollution science (pp. 261-292). Academic Press.

4. Ali, M., Bathaei, M.J., Istif, E., Karimi, S.N.H. and Beker, L., 2023. Biodegradable piezoelectric polymers: recent advancements in materials and applications. Advanced Healthcare Materials, 12(23), p.2300318.

5. Vijayakanth, T., Liptrot, D.J., Gazit, E., Boomishankar, R. and Bowen, C.R., 2022. Recent advances in organic and organic–inorganic hybrid materials for piezoelectric mechanical energy harvesting. Advanced Functional Materials, 32(17), p.2109492.

6. Ghosh, S., Roy, S., Bardhan, S., Khatua, N., Bhowal, B., Chanda, D.K., Das, S., Mondal, D., Basu, R. and Das, S., 2021. Effect of size fractionation on purity, thermal stability and electrical properties of natural hematite. Journal of Electronic Materials, 50, pp.3836-3845.

7. Kim, G.H., Hong, S.M. and Seo, Y., 2009. Piezoelectric properties of poly (vinylidene fluoride) and carbon nanotube blends: β-phase development. Physical chemistry chemical physics, 11(44), pp.10506-10512.

8. Roy, S., Thakur, P., Hoque, N.A., Bagchi, B. and Das, S., 2016. Enhanced electroactive β-phase nucleation and dielectric properties of PVDF-HFP-HFP thin films influenced by montmorillonite and Ni (OH) 2 nanoparticle modified montmorillonite. RSC advances, 6(26), pp.21881-21894.

9. Schirokauer, A., 2002. Electrostrictive and ferroelectric properties of poly (vinylidene fluoride-hexafluoropropylene) copolymer and its blends with poly (vinylidene fluoride-trifluoroethylene) copolymer. Rutgers The State University of New Jersey, School of Graduate Studies.

10. Robinson, D.A., Jones, S.B., Wraith, J.M., Or, D. and Friedman, S.P., 2003. A review of advances in dielectric and electrical conductivity measurement in soils using time domain reflectometry. Vadose zone journal, 2(4), pp.444-475.

11. El-Damrawi, G., Abdelghany, A.M. and Madshal, M.A., 2021. AC conductivity and dielectric properties of Cr2O3 doped SrO–P2O5 glasses. Physica B: Condensed Matter, 618, p.413184.

12. Hatziargyriou, N., Milanovic, J., Rahmann, C., Ajjarapu, V., Canizares, C., Erlich, I., Hill, D., Hiskens, I., Kamwa, I., Pal, B. and Pourbeik, P., 2020. Definition and classification of power system stability–revisited & extended. IEEE Transactions on Power Systems, 36(4), pp.3271-3281.

13. Motora, K.G., Wu, C.M., Rani, G.M. and Yen, W.T., 2022. Effect of ZnO particle size on piezoelectric nanogenerators and mechanical energy harvesting. Express Polymer Letters, 16(11), pp.1208-1227.

14. Roy, S., Bardhan, S., Mondal, D., Saha, I., Roy, J., Das, S., Chanda, D.K., Karmakar, P. and Das, S., 2021. Polymeric carbon dot/boehmite nanocomposite made portable sensing device (Kavach) for non-invasive and selective detection of Cr (VI) in wastewater and living cells. Sensors and Actuators B: Chemical, 348, p.130662.

15. Le, A.T., Ahmadipour, M. and Pung, S.Y., 2020. A review on ZnO-based piezoelectric nanogenerators: Synthesis, characterization techniques, performance enhancement and applications. Journal of Alloys and Compounds, 844, p.156172.

16. Kar, E., Bose, N., Dutta, B., Banerjee, S., Mukherjee, N. and Mukherjee, S., 2019. 2D SnO2 nanosheet/PVDF-HFP composite based flexible, self-cleaning

piezoelectric energy harvester. Energy conversion and management, 184, pp.600-608.

17. Wang, Z.L., 2021. From contact electrification to triboelectric nanogenerators. Reports on Progress in Physics, 84(9), p.096502.

18. Wang, L., Wang, J., Ye, C., Wang, K., Zhao, C., Wu, Y. and He, Y., 2021. Photodeposition of CoOx nanoparticles on BiFeO3 nanodisk for efficiently piezocatalytic degradation of rhodamine B by utilizing ultrasonic vibration energy. Ultrasonics Sonochemistry, 80, p.105813.

19. Singh, G., Sharma, M. and Vaish, R., 2020. Transparent ferroelectric glass–ceramics for wastewater treatment by piezocatalysis. Communications Materials, 1(1), p.100.

20. Nie, G., Yao, Y., Duan, X., Xiao, L. and Wang, S., 2021. Advances of piezoelectric nanomaterials for applications in advanced oxidation technologies. Current Opinion in Chemical Engineering, 33, p.100693.

21. Gembo, R.O., Aoyi, O., Majoni, S., Etale, A., Odisitse, S. and King'ondu, C.K., 2021. Synthesis of bismuth oxyhalide (BiOBr zI (1-z)) solid solutions for photodegradation of methylene blue dye. AAS Open Research, 4.

22. Biswas, A., Saha, S. and Jana, N.R., 2020. ZnSnO 3–hBN nanocomposite-based piezocatalyst: ultrasound assisted reactive oxygen species generation for degradation of organic pollutants. New Journal of Chemistry, 44(22), pp.9278-9287.

23. Hwang, J.Y., Moon, G.H., Kim, B., Tachikawa, T., Majima, T., Hong, S., Cho, K., Kim, W. and Choi, W., 2021. Crystal phase-dependent generation of mobile OH radicals on TiO2: Revisiting the photocatalytic oxidation mechanism of anatase and rutile. Applied Catalysis B: Environmental, 286, p.119905.

24. Choudhury, S., Sahoo, U., Pattnayak, S., Padhiari, S., Tripathy, M. and Hota, G., 2022. Hematite nanoparticles decorated nitrogen-doped reduced graphene oxide/graphitic carbon nitride multifunctional heterostructure photocatalyst towards environmental applications. New Journal of Chemistry, 46(27), pp.13100-13116.

25. Nie, G., Hu, K., Ren, W., Zhou, P., Duan, X., Xiao, L. and Wang, S., 2021. Mechanical agitation accelerated ultrasonication for wastewater treatment: Sustainable production of hydroxyl radicals. Water Research, 198, p.117124.

Chapter 4

Water flow and finger-tapping mediated piezoelectric energy generation and carcinogenic dye degradation using a Gd-incorporated natural hematite-based flexible PVDF-HFP membrane

Chapter 4

Water flow and finger-tapping mediated piezoelectric energy generation and carcinogenic dye degradation using a Gd-incorporated natural hematite-based flexible PVDF-HFP membrane

4.1 Introduction

In Chapter 3, natural α-hematite nanoparticles were used to create reusable piezo-responsive polymeric membranes for energy harvesting and wastewater treatment. Varying different percentages of α-hematite NPs in PVDF-HFP membranes revealed that 5% doping showed the highest performance having a power density of 1328 µW/cm^3 and 94.1% efficiency in degrading dye.

This chapter aims to enhance the efficiency of the membrane and thus to develop a highly effective reusable piezoelectric material from Gd-incorporated natural hematite and PVDF-HFP polymer. Incorporating Gd^{3+} into non-piezoelectric hematite natural rock enhances the polarization, dielectric permittivity as well as surface properties. Hence combining it with a PVDF-HFP matrix drastically enhances polarization and improves piezoelectricity due to the resulting high positive surface charge of nanocomposites [1]. Despite the negative surface charge of natural hematite, adding a small amount of rare earth metal creates oxygen vacancies and microstrain, leading to active sites [2]. The positive surface charge attracts the negative moieties of PVDF-HFP, flipping bonds and enhancing the polar phase, making the membranes more piezo-active than hematite-doped polymeric membranes which have been discussed previous chapter. Thus, the Gd-incorporated hematite has been doped into the PVDF-HFP membrane to the betterment of its properties. The polymer nanocomposite (hematite NPs-based PVDF-HFP membrane) was characterized using XRD, FESEM, FTIR, and TGA, providing insights into its structure, morphology, composition, and thermal stability. The material exhibited piezoelectric polarization, making it suitable for harnessing

electrical energy from mechanical perturbation and also the property has been employed for the degradation of organic carcinogenic dye via the piezocatalysis approach. Experimental validation confirmed its efficiency, implying potential applications in future green energy harvesting.
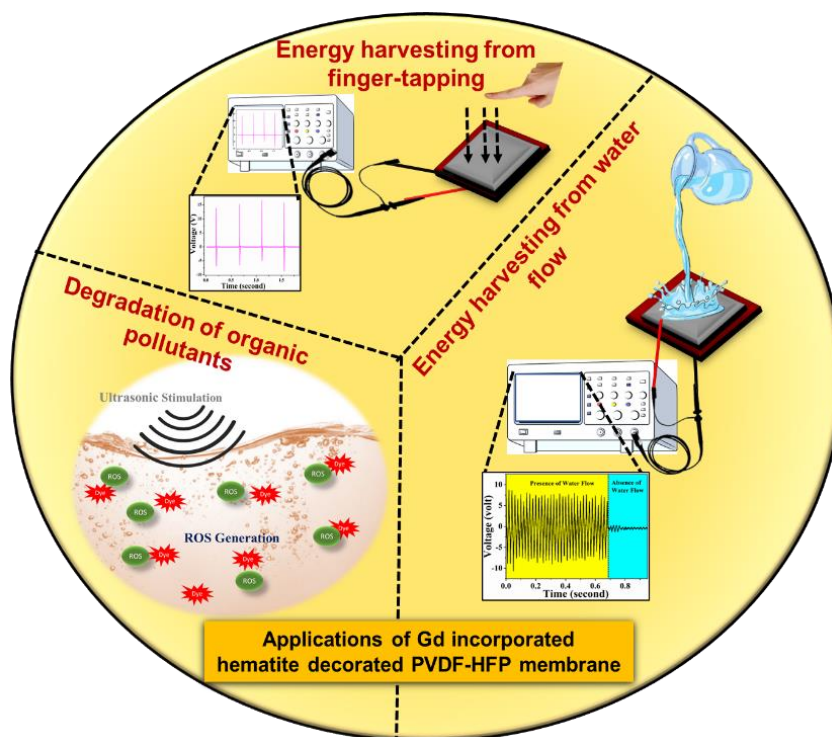
Figure 4.1 The work plan for this Chapter

4.1 Experimental details

4.1.1 Materials

The naturally formed hematite (α-hematite), was obtained from Bharat Engineering, Kolkata. The gadolinium oxide (Gd_2O_3) powder, dimethylformamide (DMF) (HPLC grade), and the aqueous ammonia solution (25 %) were purchased from Merck, India. Poly (vinylidene fluoride-hexafluoropropylene) (PVDF-HFP) pellet, p-benzoquinone (BQ), and tertbutyl alcohol (TBA) were purchased from Sigma-Aldrich, Germany. All the reagents

used were of analytical grade. Millipore water with a resistivity of 18.2 MΩ-cm was used throughout the experiments.

4.2.2 Synthesis of Gd-incorporated hematite nanoparticles

The naturally formed α-hematite was utilized to synthesize hematite nanoparticles followed by the same method mentioned in section 1.10.1 (Chapter 1). The nanoparticles were well dispersed in distilled water (1 mg mL^{-1}) using ultrasonication for 30 min. 5 % (w/w) of gadolinium oxide (Gd_2O_3) was incorporated into the hematite nanoparticles by adding the Gd_2O_3 into hematite solution, followed by vigorous stirring for 3h maintaining a pH of 10. The solution was then transferred into dust-free, clean Teflon-lines stainless steel autoclaves and maintained at 160 °C for 6 h. Afterwards the solution was then centrifuged at 6000 rpm, and the precipitate obtained was then dried in a hot air oven at 80 °C, collected, and stored for further use.
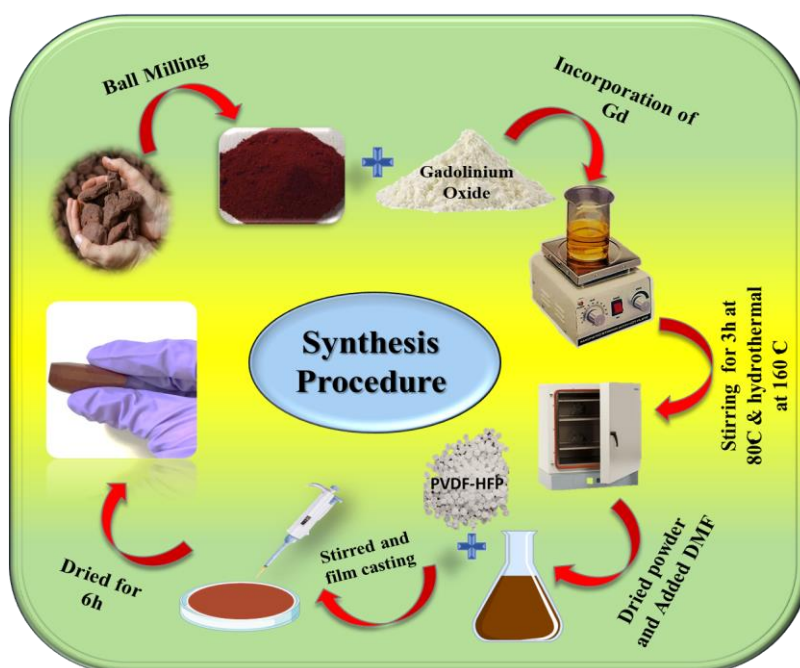
Figure 4.2 *Schematic representation of the synthesis procedure*

4.2.3 Preparation of Gd-doped hematite-based PVDF-HFP nanocomposite membranes

The polymer nanocomposite was fabricated by incorporating 2.5 % and 5 % of Gd-incorporated hematite into PVDF-HFP. 0.5mg PVDF-HFP was taken in a vial and dissolved into 10 mL DMF and the above-said percentage of Gd doped hematite was incorporated into it and the solution was stirred for 6h at 60 °C. The solution was then poured into a clean petri dish and dried for 8hrs at 70°C. The 2.5 wt% and 5 wt% of Gd-incorporated hematite incorporated membrane are named PVGF2.5 and PVGF5 respectively whereas PVGF0 being the pure PVDF-HFP membrane without any incorporation of Gd-incorporated hematite. A schematic representation of the whole synthesis procedure has been depicted in Figure 4.2.

4.3 Result and discussions

4.3.1 Physical Characterisations

X-ray diffraction was employed to analyze the structural as well as microstructural parameters of the synthesized materials [3]. The XRD pattern of the hematite nanoparticles and Gd-incorporated hematite nanoparticles has been illustrated in Figure 4.3(a-b). It was observed that all the diffraction peaks of hematite NPs (nanoparticles) are well-matched with JCPDS card no 72–0469. Thus, the absence of any undesirable maxima in the diffraction pattern confirms the purity of hematite NP. Even after doping of 5 % Gd^{3+} peak positions do not alter, suggesting successful doping of Gd^{3+} ions into the matrix of hematite NPs.

The cell dimensions a and b were both 5.034 Å and c was 13.745 Å found from the Rietveld refinement and the unit cell was visualized by Vesta v3.4.3 (visualization for electronic and structural analysis) software [Figure 4.3(c)]. It was observed that due to the incorporation of Gd^{3+}, the micro-strain has been increased from 1.3 x 10^{-4} to 9.0 x 10^{-4} as the size of the

Gd^{3+} is larger than Fe^{3+} inducing excessive stress during the substitution of host ions, and thus forming the defects in the lattice structure [4-5]. Along with micro-strain, it was also found that oxygen vacancies were created in the doped NPs owing to such cationic substitution. These altered micro-strain and oxygen vacancies enhanced the physicochemical properties of the doped NPs significantly [6-7].
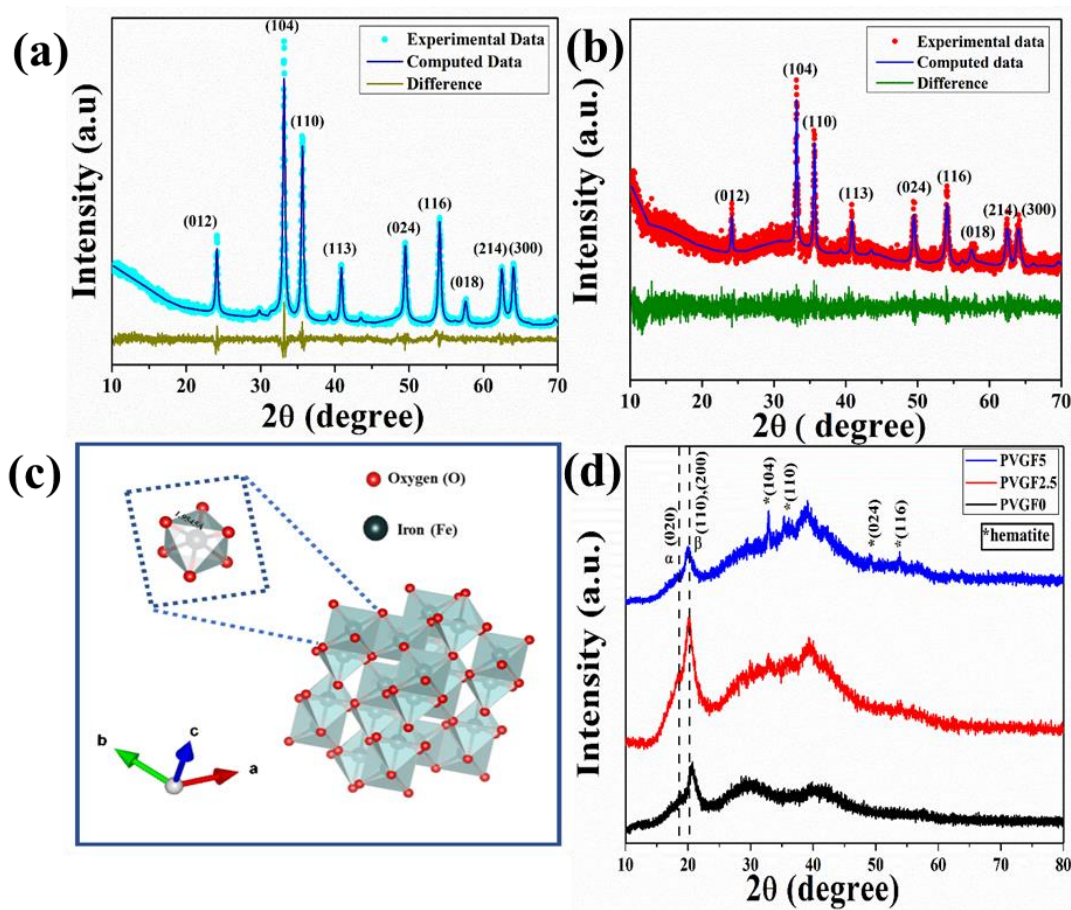
Figure 4.3. *(a-b) Experimental and computed XRD pattern of natural α-hematite and Gd incorporated α-hematite respectively (c) Unit cells of Gd incorporated α-hematite (d) XRD pattern of natural Gd incorporated α-hematite nanocomposite membranes suggesting that incorporation of nanocomposite into polymer matrix enhance the polar phase and found maximum in PVGF2.5.*

The XRD diffractograms of Gd-doped hematite-incorporated PVDF-HFP membranes have been depicted in Figure 4.3(d). The peak at 18.3º and 20.2º represents respectively the non-polar α-phase and polar β-phase of nanocomposite films [8]. The peak at 20.2º enhanced

after the incorporation of nanocomposite in the PVD-HFP matrix and was found to be the maximum for PVGF2.5. This implies that the incorporation of nanocomposite in the PVDF-HFP matrix enhanced its polar beta phase. The enhancement of the polar phase in the PVGF2.5 membrane made it suitable for applications that are modulated by the polarizing effects of membranes like piezoelectricity.

FESEM and TEM were employed to study the morphological parameters, particle size, etc [9]. The structure of the Gd-doped hematite depicted a hexagonal structure as evident from TEM micrographs [Figure 4.4(a)]. The particle size distribution curve was estimated by employing ImageJ software to determine the particle size, which suggested the ranges of NPs from 30 to 6 0 nm, with a median at 40-50 nm [Figure 4.4(b)].

The FESEM of the membrane in Figure 4.4(c) illustrates the smooth and homogeneous surface in the pristine PVDF-HFP (PVGF0) membrane, which becomes rough and spherulite in nature with the doping of the Gd-doped hematite NPs. PVGF5 [Figure 4.4(e)] shows a greater perturbed and rough surface compared to PVGF2.5 [Figure 4.4(d)] due to the enhancement of the dopant in the PVDF-HFP matrix [10-11]. These spherulites nature of the micrographs is evident that the β-phase formation in the PVGF2.5 and PVGF5 due to the interaction between the Gd-doped hematite with CH_2-CF_2 moiety of PVDF-HFP polymer chain [10,12].

The elemental composition analysis was done by EDS which depicted the stoichiometric ratio of Fe, O, and Gd in doped hematite NPs. It was observed that 3.25 wt% Gd was incorporated in the nanocomposite matrix though the doping concentration was 5% this occurred due to improper attachment of some Gd^{3+} ions in hematite NPs which were further washed out by centrifugation [Figure 4.4(f) and A2.1]. The nanocomposite has been incorporated in the PVDF-HFP matrix by 2.5 and 5 wt%. By performing the percentage calculation, it has been found that in the PVGF2.5 membrane, 0.07% Gd was present in
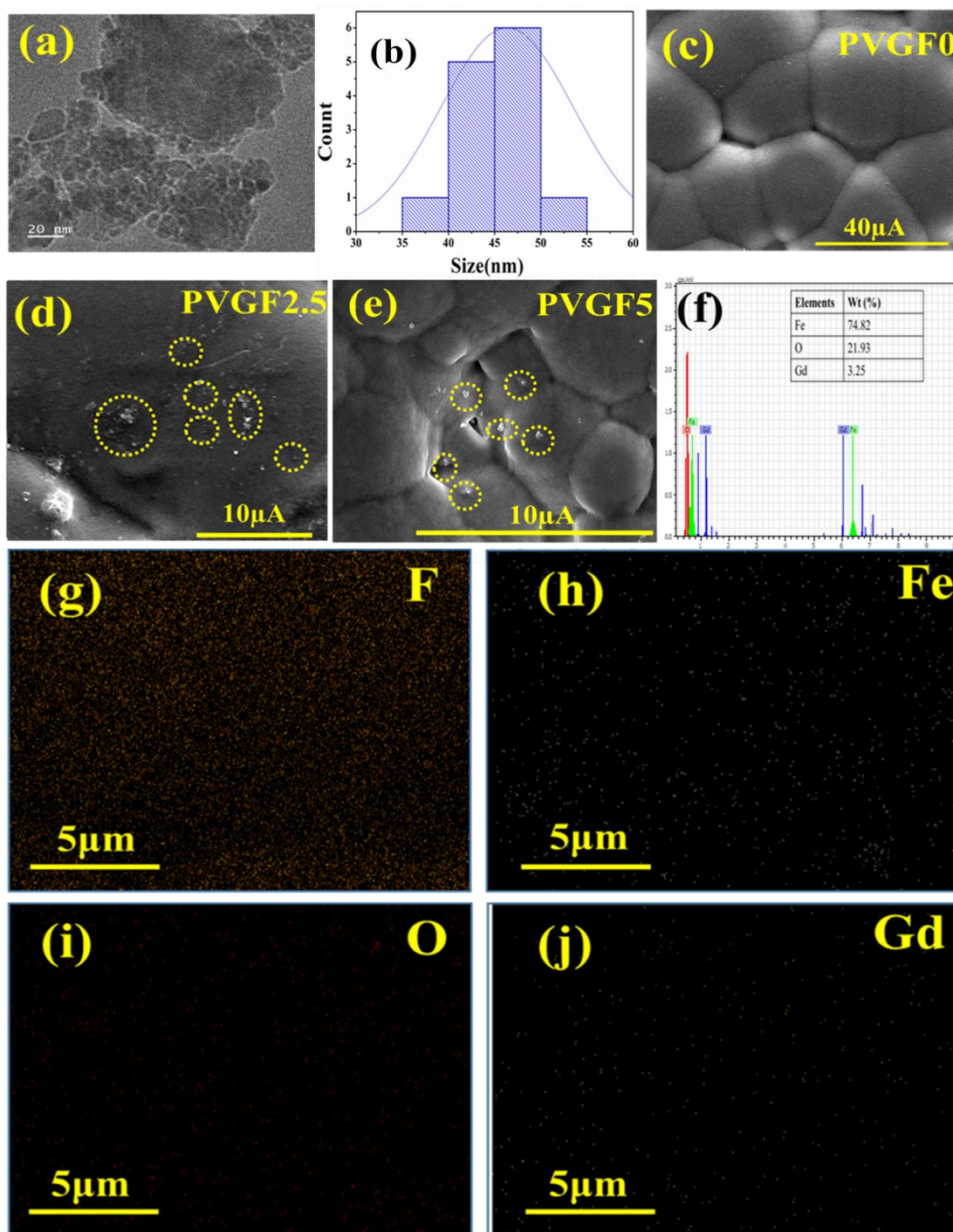
Figure 4.4. (a-b) TEM image and the size distribution curve of Gd incorporated α-hematite, (c-e) FESEM micrographs of PVGF0, PVGF2.5, PVGF5, (f) EDX images Gd incorporated hematite NPs, (g-j) mapping of PVGF2.5 membrane suggesting the homogeneous distribution of doped Gd incorporated hematite in the PVDF-HFP matrix. The carbon distribution of the membrane does not show due to the use of carbon tape during the EDS mapping measurement.

PVGF5 whereas in PVGF5 0.14% Gd was there. The mapping data of PVGF2.5 depicted a homogeneous distribution of Fe, O, and Gd in the PVDF-HFP matrix by the proper stoichiometric ratio [Figure 4.4(g-j)]. The C contained in the PVDF-HFP membrane has not been found in the mapping data because it has been eliminated for the use of carbon tape attached to EDS measurement.

The zeta potential was evaluated for understanding the surface charge of the hematite NPs and their modified counterpart. The naturally formed hematite exhibits a negative surface charge (-7.23 mV) found in Figure 3.5 (Chapter 3). A very small amount of rare earth metal incorporated in its matrix generated stress and micro-strain evident from the crystallographic refinement. Such stress created oxygen vacancies in the hematite matrix and thus generated active sites. The vacancy of electronegative oxygen enhanced the surface charge of the nanocomposite to +12.3mV [Figure 4.5(e)] [13-14].

FTIR was employed for determining bonding networks of the nanocomposite membranes and to confirm the formation of β-phase nucleation due to doping [15] as depicted in Figure 4.5(c). The absorbance bands observed at 532 cm^{-1} (-CF$_2$ bending), 615 cm^{-1} (-CF$_2$ bending), 762 cm^{-1} (skeletal bending), and 794, 976 cm^{-1} (-CH$_2$ rocking) were for α-phase of the PVDF-HFP which was consequently reduced in PVGF2.5 and PVGF5 [16]. The peaks at 484 cm^{-1} (-CF$_2$ deformation), 510 cm^{-1} (-CF$_2$ stretching), 602 cm^{-1} (-CF$_2$ wagging), and 841 cm^{-1} (-CF$_2$ stretching, -CH$_2$ rocking and skeletal C-C stretching) are β-phase absorbance band which was increased with NPs incorporation and found to be maximum in PVGF2.5 calculated with the formula mentioned in equation 1.8 (Chapter 1). In the case of PVGF5, β-phases were slightly reduced than PVGF2.5 but the percentage of β-phases was more than PVGF0 [16-17].

The percentage of β-phase nucleation developed due to the doping of Gd-doped hematite (Gd incorporated hematite) into the PVDF-HFP membrane has been calculated and found

to be highest in the PVGF2.5 (80.3 %). In the case of PVGF0, it has the lowest value i.e. 60.8 %, and the fraction of electroactive β-phase for PVGF5 is 71.2 % [Figure 4.5(d)] which could be due to an excess amount of doping and crossing the critical limit of incorporation of Gd-incorporated hematite into the membrane [10]. The FTIR spectra of 2.5 % pristine hematite incorporated PVDF-HFP have been depicted in Figure 3.4 (b) (Chapter 3) which indicate the percentage β-phase to be 78.7%. In reality, the highly positive surface charge of Gd-incorporated hematite attracts the negative moiety of the PVDF-HFP polymeric chain ($-CF_2$) and subsequently enhanced the polar phase by flipping the $-CF_2$ and $-CH_2$ bond on the opposite side of the carbon chain of PVDF-HFP. After the incorporation of NPs in a certain limit the excess positive surface charge further reduces the polar phase by attracting the negative moiety.

To determine the thermal stability of the nanocomposite membranes, TGA (thermogravimetric analysis) and DTG (derivative thermogravimetric) were performed and the percentage mass loss of the membranes with the varying temperature were calculated [Figure 4.5(a-b)] [18]. It was found that the decomposition of bare PVDF membrane started near about $430^{o}C$ whereas Gd-doped hematite incorporated PVDF membrane the decomposition temperature was $475^{o}C$, indicating the improvement of thermal stability owing to incorporation of nanocomposite in the PVDF matrix. The interaction between the PVDF chain and the Gd-doped hematite enhanced the thermal stability by forming the crosslink as well as the greater adhesion between the well-distributed nanofillers and the PVDF-HFP matrix by restricting the movement of the PVDF-HFP chain and leading towards the enhancement of the thermal stability [19-21]. The mass losses of the synthesized membranes were found to be negligible for PVGF0- 4.1%, PVGF2.5- 3.47%, and PVGF5- 1.8% as depicted in Figure 4.5(a). This phenomenon suggests that the membrane can perform efficiently even at a higher temperature.

4.3.2 Electrical properties and estimation of piezoelectric coefficients of the membrane

Piezoelectric nature is highly dependent on the polarity of the sample; hence it is essential to enhance the polar nature of the sample to achieve better results. For a better understanding of the successful enhancement of polarizability, the electrical properties were explored by evaluating the dielectric permittivity, tangent loss, and storage capacity of the samples [22]. The dielectric constant has been calculated by using equation 1.10 (Chapter 1).
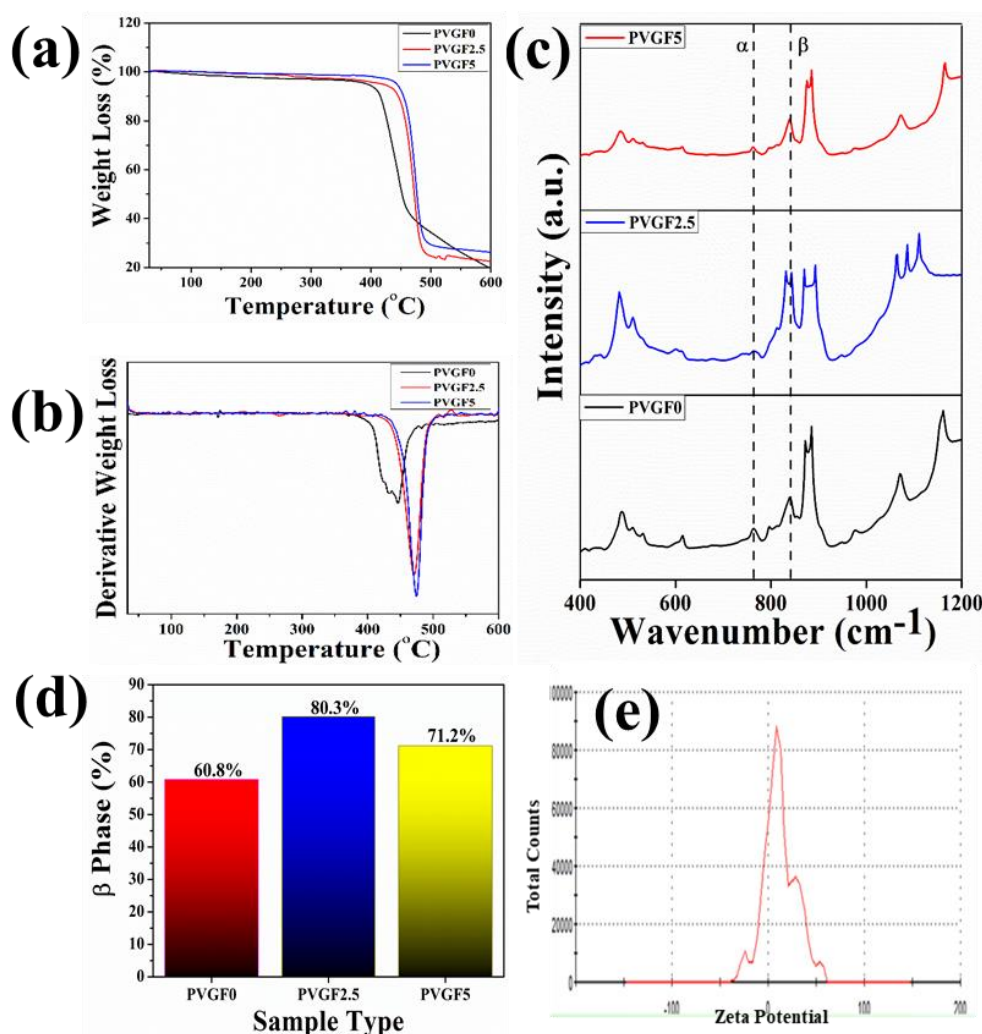
Figure 4.5 *(a) Percentage of weight losses of nanocomposite membranes, (b) Derivatives weight loss of the nanocomposite membranes suggesting better stability in doped membranes, (c) FTIR spectroscopy of PVGF0, PVGF2.5, PVGF5, shown polar phase enhancement after nanocomposite inclusion into the polymer matrix (d) Percentage β-phase of sample PVGF0, PVGF2.5, PVGF5, (e) Zeta potential of Gd incorporated hematite shows a high positive surface charge.*

The powdered hematite NP and Gd-incorporated modified NPs were compressed into pellets of 10 mm × 1.3 mm dimensions using a hydraulic press. The variation of dielectric permittivity and tangent loss of the Gd-incorporated hematite NPs with frequency are depicted in Figure 4.6(a) and Figure 4.6(c). It is evident from the figures that the dielectric constants for both samples are high at low frequency and gradually reduce with the increase in frequency due to Maxwell-Wagner interfacial polarization [23]. It is in a good agreement with Koop's theory [24]. Along with this, Gd-doped hematite NPs were found to have higher values of dielectric constants than hematite NPs. This is due to the doping of Gd^{3+} that could generate crystal defects which induced imperfection in the alignments of crystal as the size of the Gd^{3+} ion is larger than Fe^{3+} creating stress inside the host lattice which has also good agreement with XRD data [4, 6]. The space charge at the interface was formed due to the external field trapped by the interfacial defects at the grain boundaries resulting in the rise of the dielectric constant for the Gd-doped hematite NPs (~500) [6, 25]. Thus, the dielectric constant and polarization capability for the doped NPs was more due to the generation of defects, and oxygen vacancies as well as the stress inside the crystals. The high polarization efficiency of the Gd-incorporated hematite NPs was further utilized by fabricating the nanocomposite membranes.

The dielectric constants of the nanocomposite membranes were also measured. The three films (PVGF0, PVGF2.5, PVGF5) of $1cm^2$ attached with two aluminum electrodes to form a device were taken to measure the electrical properties of the membranes. The graph of dielectric constants of the three nanocomposite membranes with frequency has been shown in Figure 4.6(b). It is noteworthy to record the dielectric constant has been increased due to the doping of Gd-doped hematite NPs. PVGF2.5 shows the highest dielectric value i.e. 19 at 40 Hz and pristine PVDF-HFP membrane has the lowest value of ~6.78 at 40 Hz [Figure 4.6(f)]. The polarization increases due to the doping of NPs which also causes the

enhancement of dielectric phenomena as well as the β-phase of the film PVGF2.5 [26]. It is also noticed that the dielectric constant reduces with the increase in frequency which is the evidence of Maxwell-Wagner polarization which explains that with the high frequency, the dipole cannot change rapidly causing the reduction of dielectric permittivity [27]. Tangent loss and the ac conductivity with varying frequencies were also measured. The doped membrane exhibits the lowest tangent loss (0.05) than the pure one at a frequency of 40 Hz depicted in Figure 4.6(d). The very low tangent loss minimizes the energy dissipation which is very much advantageous for future use [28]. The ac conductivity of the membranes increases with the increase in frequency shown in Figure 4.6(e). In reality, the conducting grains achieve the required amount of activation energy to become free at the higher frequency enhancing the conductivity in the higher range of frequency [29]. The dielectric permittivity data suggest that the maximum polarization occurs in the PVGF2.5. This result is also analogous to the XRD, and FTIR measurements which depicted the maximum polarization achieved in the 2.5% nanocomposite-doped membrane. These high polarizing properties made this self-poled free-standing membrane promising for piezo-responsive applications.

The piezoelectric coefficients (d_{33}) of all the fabricated membranes was also measured to find the piezo effectiveness [30]. The piezoelectric coefficients of the synthesized membranes were calculated by the relation mentioned in equation 3.1 (Chapter 3).

The comparative graph of d_{33} for PVGF0, PVGF2.5, and PVGF5 has been shown in Figure 4.7(a) and it has been found that PVGF2.5 has the highest value of d_{33} (47.32 pC/N) whereas PVGF0 and PVGF5 have 3.27 pC/N and 27.05 pC/N respectively, which validates the enhancement of polarization as well as polar β-phase enhancement in PVGF2.5. Whereas in the case of PVGF5, it slightly decreases which may be due to reaching the critical limit of dopant creating a high concentration of positive surface charge in the PVDF-HFP matrix
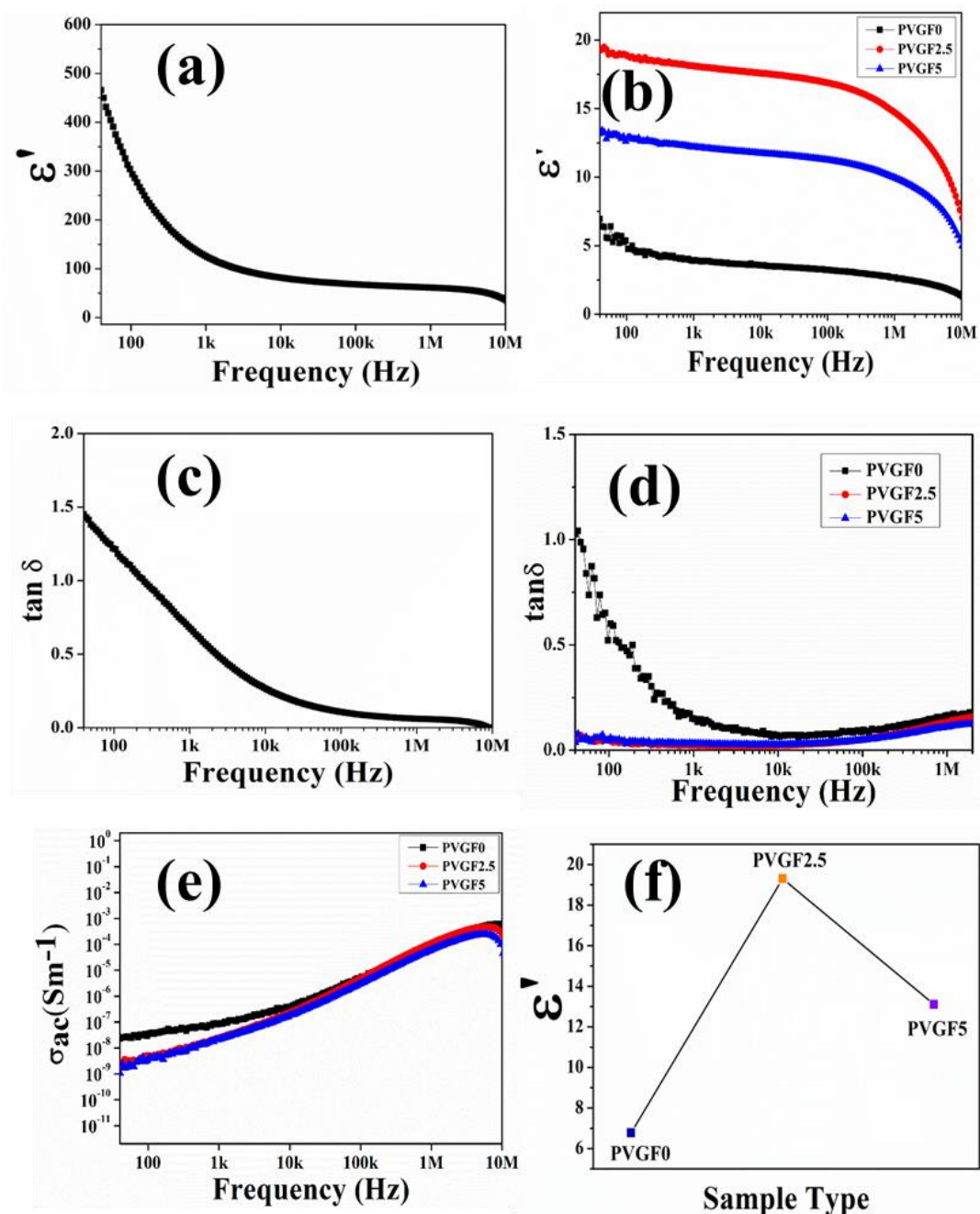
Figure 4.6. *(a) Dielectric constant with the frequency of Gd-incorporated α-hematite nanoparticles suggesting the Gd incorporation enhanced the NPs dielectric constant, (b) Dielectric constants of PVGF0, PVGF2.5, and PVGF5 respectively (c-d) Tangent loss of Gd-incorporated α-hematite NPs and membranes suggesting low energy dissipation (e) Variation of ac conductivities with the frequency for the nanocomposite membranes show the maximum conductivity in PVGF2.5, and (f) Comparison of the dielectric constant of sample PVGF0, PVGF2.5, PVGF5 at 40Hz*

and realignment of the negative moiety of polymeric chain which reduces the polarization.

The piezoelectric coefficients of the membranes have been investigated in a cyclic manner

up to five cycles with standard deviation. All the experimental results show that the PVGF2.5 membrane has high piezo-responsive properties which are further used to harvest non-invasive piezoelectric energy [31-33].

4.3.3 Piezoelectric energy generation

The PVGF2.5 membrane was used for piezoelectric energy generation for having the highest piezo-responsive properties along all the membranes. A 2cm×2cm film was cut and two aluminum electrodes with copper wire were attached on both sides of the film to fabricate the device shown in Figure 4.7(b). The entire sandwich device were covered with a PET (polyethylene terephthalate) coated jacket to save it from any kind of damage.

The fabricated device was used to harvest energy by finger tapping and the open circuit output voltage was measured using the digital oscilloscope (Agilent N2862B 10:1 passive probe). The short circuit currents were obtained using the DAQ6510 multi-meter system, Keithley. The open circuit output voltages were found around 6.5, 16.92, and 10.1V for PVGF0, PVGF2.5, and PVGF5 respectively. The short circuit currents were also recorded and found 0.14, 0.52, and 0.32 μA respectively due to finger tapping with the tapping force of 13.49N. The graph for the instantaneous voltage and the current has been shown in Figures 4.7(c) and 4.7(d) respectively. The force-varying open circuit voltages were measured and found that the voltage increases with the increasing force on the device Figure 4.7(e). The voltage increased appreciably with the increase in the applied force on the device PVGF2.5 and was found to be 5.6V, 11.07V, 16.92V, and 20.44V at 7, 10, 13, and 16 N force respectively. It was found that under a constant mechanical force, the voltage and current generation are maximum in PVGF2.5 which is a good agreement with the experimental evidence by XRD, FTIR, D.C, and d_{33} measurements. The instantaneous
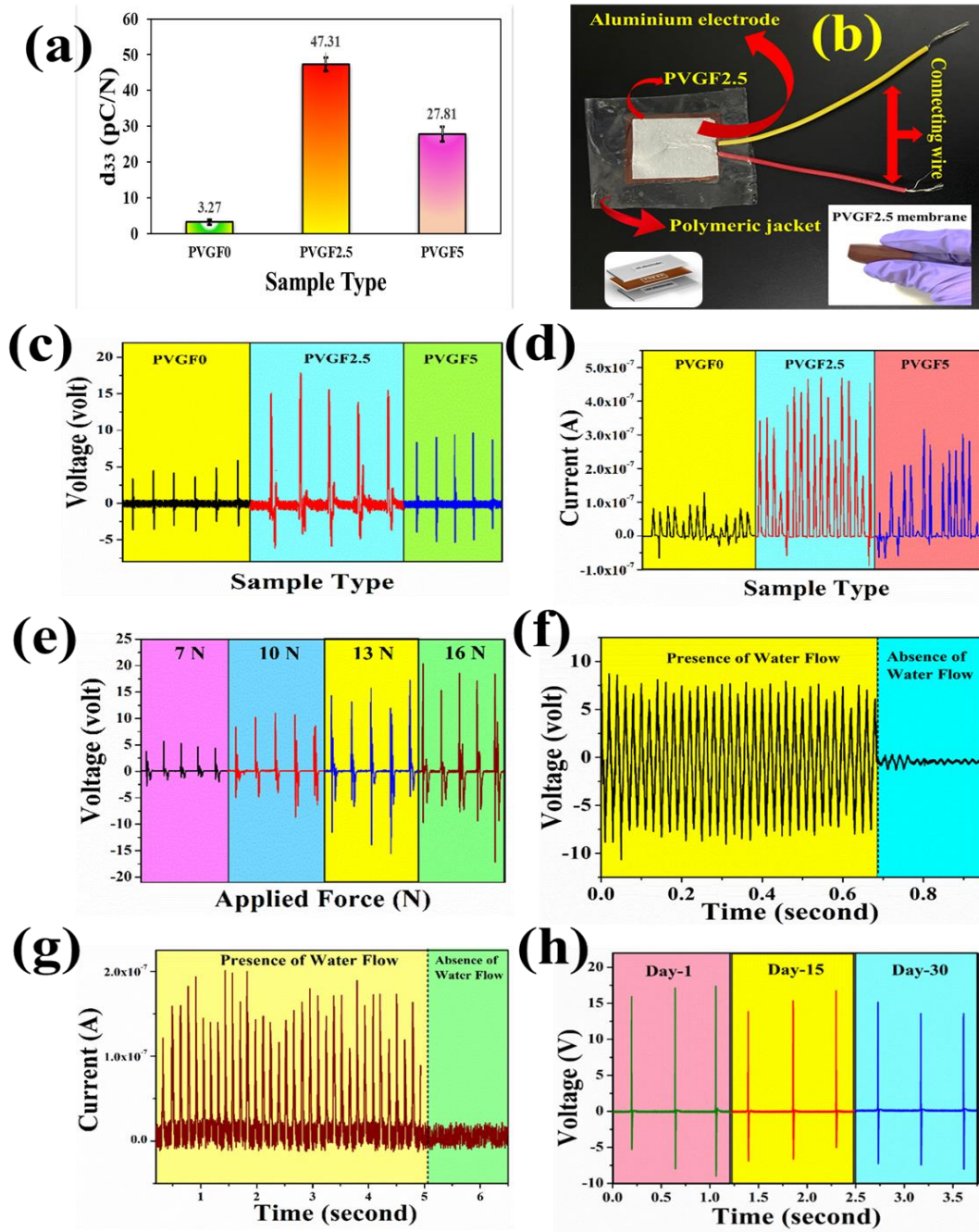
Figure 4.7. *(a) Piezoelectric coefficients of the nanocomposite membranes suggesting PVGF2.5 possess the highest d_{33} value, (b) Real image of the fabricated device and in the inset the fabricated PVGF2.5 nanocomposite membrane, (c, d) Open circuit voltage and short circuit current due to finger tapping on PVGF0, PVGF2.5 and PVGF5 devices, (e) piezoelectric voltage generation under different applying forces (f, g) Open circuit voltage and short circuit current of the PVGF2.5 device under water flow, (h) Performance test of the device over time.*

power density was calculated for the PVGF2.5 membrane of volume ($2 \times 2 \times 0.01$ cm^3) with the help of the mathematical relation stated in equation 3.2 (Chapter 3). The calculated power density was 232.38 µW cm^{-3} for PVGF2.5 at 13.49 N force.

Besides the finger tapping, the device can harvest energy from the water flow as well and it was also found that the open circuit voltage during the flow of water was 8V and the graph for it has been depicted in Figure 4.7(f). The corresponding short circuit current due to the flow of water was obtained around 0.2 µA [Figure 4.7(g)]. Herein, tap water having a TDS (total dissolved solids) value of 162 ppm was taken as the water source and generated the water flow by a simple overhead stirrer. The TDS of water plays a pivotal role in water flow-based energy generation. The water having more TDS applied more force on the device for the dissolved solid in it and the voltage was also enhanced [34]. The mechanism behind the piezo-energy harvesting is illustrated in section 1.7.2 (Chapter 1).

4.3.4 Carcinogenic organic dye degradation using piezocatalysis

To investigate the piezocatalytic effectiveness of the prepared samples, an experiment was conducted using the acidic and carcinogenic Rhodamine B (RhB) dye. A Telesonic ultrasonics machine operating at a frequency of 15 kHz was employed for the degradation experiment. Initially, a glass vial containing 20 mL of dye solution at a concentration of 2.5 ppm was prepared. then, the synthesized PVGF2.5 membrane (2cm x 2cm dimension), the piezocatalyst, was added to the dye solution. Subsequently, the solutions underwent ultrasonic vibration for 35 minutes. At 10-minute intervals, small portions of the solutions were withdrawn from the designated vial, and their optical density was measured at a wavelength of 554 nm. This analysis enabled the quantification of the percentage of piezodynamic degradation of the dyes. The absorbance spectra demonstrate the degradation kinetics of the piezocatalysts. The percentage of efficiency of piezo degradation (η) and the

first-order kinetic constant (k) values were determined by the relation mentioned in equations 3.6 and 3.7 (Chapter 3).

The results indicated that the percentage degradation of RhB dye was approximately 94.3% for PVGF2.5. The PVGF2.5 sample has a rate constant (k) of 7.16×10^{-2} min^{-1} for the dye. This is due to the β-phase formation into the PVDF-HFP matrix, which further enhances the polarizability and results in the degradation of RhB. During the ultrasonic treatment, it was observed that the initial dark pink colour of the RhB dye gradually became transparent within 35 min [Figure-4.8(a)].
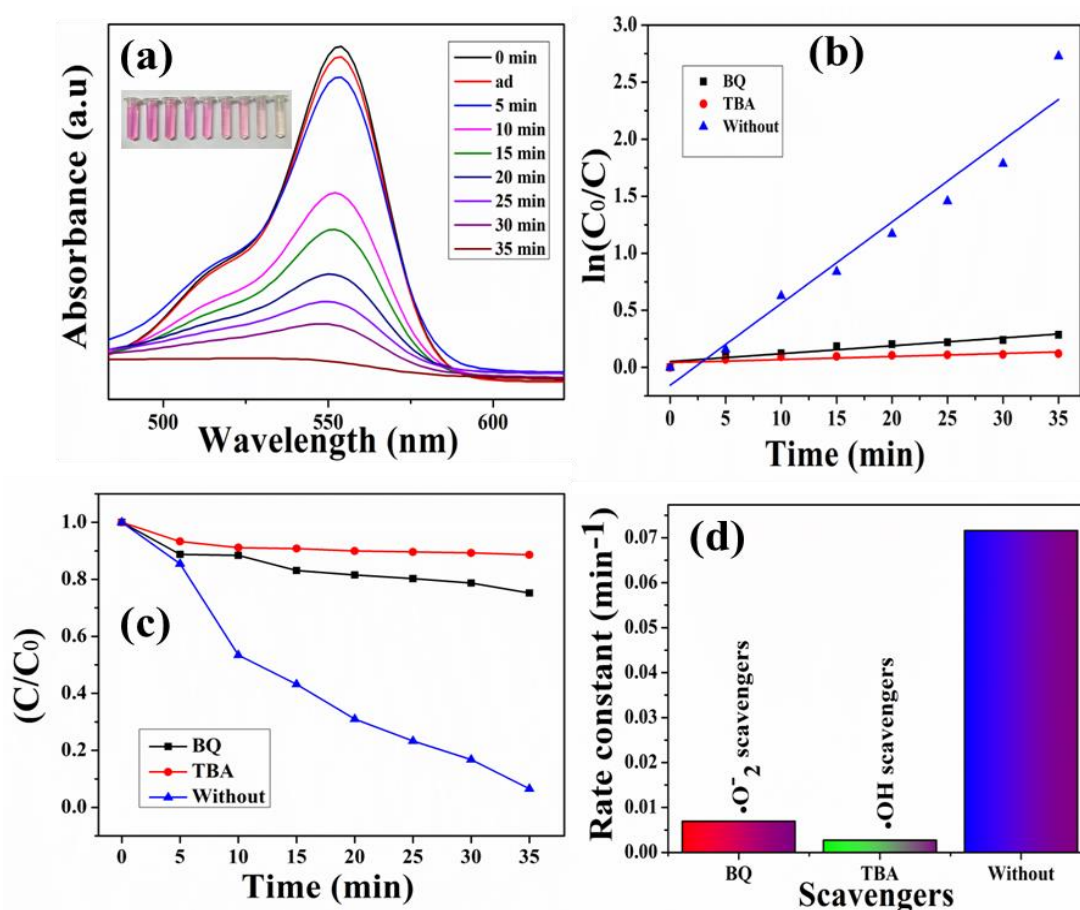
Figure 4.8 *(a) UV-Vis spectra of dye degradation and decolorization of Rhodamine B (RhB), (b-c) Ultrasound-assisted RhB degradation ln(C$_0$/C) and (C/C$_0$) represents the scavenging studies in the presence of several oxygen species and shows •OH radicals as one of the primary species for piezocatalysis, (d) Kinetic rate constant for RhB degradation caused by various scavengers*

4.3.5 Scavenger experiment

Scavenging experiments were conducted to identify the key reactive species responsible for degrading Rhodamine B (RhB) molecules. Figure 4.8(b-c) illustrates degradation curves, showing a decrease in catalytic degradation efficiency upon the addition of scavengers, indicating their active participation in the RhB degradation process. Suppression of RhB degradation was observed when trapping superoxide radical ($O_2\bullet-$) with benzoquinone (BQ) or hydroxyl radical (OH•) with tert-butyl alcohol (TBA). Figure 4.8(c) shows a linear dependence of (C/C_0) on time (t), indicating first-order degradation kinetics. It is shown that adding TBA greatly lowers dye degradation by lowering the reaction rate (0.269×10^{-2} min^{-1}), ensuring the presence and dominance of hydroxyl (•OH) radicals among all in this situation Figure 4.8(d). Hence, the results highlight the significant role of TBA, corresponding to hydroxyl radicals, in organic dye degradation. These experiments provide insights into the degradation mechanism, emphasizing the involvement of specific reactive species, particularly hydroxyl radicals, in the process.

4.3.6 Figure of merits of the membrane/device

The PVGF2.5 membrane that was used to fabricate the device has enormous advantages. It has quite a flexibility, thermal stability, and water-resistive nature along with biocompatibility. The flexibility of the membrane is shown in Figure 4.7(b-inset) whereas Figure 4.5(a, b) ensures its thermal stability up to 475 ºC where mass loss is more negligible in the case of doped PVDF-HFP membrane than that of PVGF0. Another exciting factor of this study is the use of water flow as mechanical energy to convert it into electrical energy. The recyclability of the device has also been investigated and found that after 30 days it does not alter its effectiveness [Figure 4.7(h)]. In this case, output voltage under water flow is nearly 8V and due to finger tapping it is 16.92V. Another interesting aspect of this study

is that this membrane can degrade one of the carcinogenic dye, RhB, by 94.3% in only 35 minutes, which is indeed a remarkable property.

4.4 Summary

This chapter portrays the successful synthesis procedure of Gd-incorporated natural hematite in nano forms and also the incorporation of these nanoparticles into a polymeric matrix to fabricate flexible membranes. The incorporation of the rare earth element (Gd^{3+}) in the α-Fe_2O_3 structure greatly influences the microstrain, which ultimately enhances the polarisability. Moreover, doping of the Gd-loaded hematite in the PVDF-HFP matrix escalates the β-phase of the film, as established from FT-IR, dielectric, and d_{33} studies. The nanoparticle loading also improves the stability of the membrane, making it suitable for commercial use. The solid-state device fabricated from the flexible membrane is capable of generating piezoelectric energy from finger tapping as well as water flow. It is recorded that the voltage generated due to finger tapping is 16.92 V and current 0.52 µA and hence the power density has become 232.38 µW cm^{-3}. Another interesting part of this chapter is that the device herewith can also harvest piezoelectric energy from the water flow like a non-invasive stimulus. Thus, the reusable, robust, free-standing, cost-effective device can be useful for harvesting energy from naturally flowing water sources, cutting down the dependency on conventional energy sources. From the flow of water, it has generated a voltage of 8 V and a current of 0.2 µA which is quite high. Along with this, the piezo response of material has been employed for piezo catalysis to degrade dye (RhB solution). After 35 minutes, the breakdown of this dye solution via piezocatalysis is complete and readily apparent. The dye degradation efficiency is around 94.3% in 35 minutes, which is excellent for the natural NP-based film PVF5. Thus, it can be a sustainable and futuristic solution to eliminate the energy crisis as well as water pollution to the growing industrialization and modernization.

References

1. Sharma, S., Mishra, S.S., Kumar, R. and Yadav, R.M., 2022. Recent progress on polyvinylidene difluoride-based nanocomposites: applications in energy harvesting and sensing. New Journal of Chemistry, 46(39), pp.18613-18646.

2. Ghosh, S., Mondal, D., Roy, S., Roy, J., Bardhan, S., Mazumder, A., Bag, N., Basu, R. and Das, S., 2023. Water flow and finger-tapping mediated piezoelectric energy generation using a natural hematite-based flexible PVDF-HFP membrane. Journal of Materials Chemistry C, 11(39), pp.13418-13428.

3. Ali, A., Chiang, Y.W. and Santos, R.M., 2022. X-ray diffraction techniques for mineral characterization: A review for engineers of the fundamentals, applications, and research directions. Minerals, 12(2), p.205.

4. Roy, S., Bardhan, S., Chanda, D.K., Maity, A., Ghosh, S., Mondal, D., Singh, S. and Das, S., 2020. Cu (II) and Gd (III) doped boehmite nanostructures: a comparative study of electrical property and thermal stability. Materials Research Express, 7(2), p.025020.

5. Raizada, P., Soni, V., Kumar, A., Singh, P., Khan, A.A.P., Asiri, A.M., Thakur, V.K. and Nguyen, V.H., 2021. Surface defect engineering of metal oxides photocatalyst for energy application and water treatment. Journal of Materiomics, 7(2), pp.388-418.

6. Roy, S., Pal, K., Bardhan, S., Maity, S., Chanda, D.K., Ghosh, S., Karmakar, P. and Das, S., 2019. Gd (III)-doped boehmite nanoparticle: an emergent material for the fluorescent sensing of Cr (VI) in wastewater and live cells. Inorganic Chemistry, 58(13), pp.8369-8378.

7. Das, A., Wary, R.R. and Nair, R.G., 2020. Cu modified ZnO nanoflakes: An efficient visible light-driven photocatalyst and a promising photoanode for dye sensitized solar cell (DSSC). Solid State Sciences, 104, p.106290.

8. Saha, P., Debnath, T., Das, S., Chatterjee, S. and Sutradhar, S., 2019. β-Phase improved Mn-Zn-Cu-ferrite-PVDF nanocomposite film: a metamaterial for enhanced microwave absorption. Materials Science and Engineering: B, 245, pp.17-29.

9. Singh, J., Sharma, S., Soni, S., Sharma, S. and Singh, R.C., 2019. Influence of different milling media on structural, morphological and optical properties of the ZnO nanoparticles synthesized by ball milling process. Materials Science in Semiconductor Processing, 98, pp.29-38.

10. Mondal, D., Bardhan, S., Das, N., Roy, J., Ghosh, S., Maity, A., Roy, S., Basu, R. and Das, S., 2022. Natural clay-based reusable piezo-responsive membrane for water droplet mediated energy harvesting, degradation of organic dye and pathogenic bacteria. Nano Energy, 104, p.107893.

11. Chai, H., Gao, L. and Jin, J., 2022. Revealing the Essential Role of Iron Phosphide and its Surface-Evolved Species in the Photoelectrochemical Water Oxidation by Gd-Doped Hematite Photoanode. ChemSusChem, 15(17), p.e202201030.

12. Kahil, H., Faramawy, A., El-Sayed, H. and Abdel-Sattar, A., 2021. Magnetic properties and SAR for gadolinium-doped iron oxide nanoparticles prepared by hydrothermal method. Crystals, 11(10), p.1153.

13. Midekessa, G., Godakumara, K., Ord, J., Viil, J., Lättekivi, F., Dissanayake, K., Kopanchuk, S., Rinken, A., Andronowska, A., Bhattacharjee, S. and Rinken, T., 2020. Zeta potential of extracellular vesicles: toward understanding the attributes that determine colloidal stability. ACS omega, 5(27), pp.16701-16710.

14. Pan, K., Yang, C., Hu, J., Yang, W., Liu, B., Yang, J., Liang, S., Xiao, K. and Hou, H., 2020. Oxygen vacancy mediated surface charge redistribution of Cu-substituted LaFeO3 for degradation of bisphenol A by efficient decomposition of H2O2. Journal of hazardous materials, 389, p.122072.

15. Ahmed, A., Jia, Y., Deb, H., Arain, M.F., Memon, H., Pasha, K., Huang, Y., Fan, Q. and Shao, J., 2022. Ultra-sensitive all organic PVDF-TrFE E-spun nanofibers with enhanced β-phase for piezoelectric response. Journal of Materials Science: Materials in Electronics, 33(7), pp.3965-3981.

16. Fu, Y., Cheng, Y., Chen, C., Li, D. and Zhang, W., 2022. Study on preparation process and enhanced piezoelectric performance of pine-needle-like ZnO@ PVDF composite nanofibers. Polymer Testing, 108, p.107513.

17. Ghosh, S., Bardhan, S., Mondal, D., Sarkar, D., Roy, J., Roy, S., Basu, R. and Das, S., 2023. Natural hematite-based self-poled piezo-responsive membrane for harvesting energy from water flow and catalytic removal of organic dye. Ceramics International, 49(9), pp.14710-14718.

18. Díez, D., Urueña, A., Piñero, R., Barrio, A. and Tamminen, T., 2020. Determination of hemicellulose, cellulose, and lignin content in different types of biomasses by thermogravimetric analysis and pseudocomponent kinetic model (TGA-PKM method). Processes, 8(9), p.1048.

19. AlAhzm, A.M., Alejli, M.O., Ponnamma, D., Elgawady, Y. and Al-Maadeed, M.A.A., 2021. Piezoelectric properties of zinc oxide/iron oxide filled polyvinylidene fluoride nanocomposite fibers. Journal of Materials Science: Materials in Electronics, 32(11), pp.14610-14622.

20. Irwin, P.C., Cao, Y., Bansal, A. and Schadler, L.S., 2003, October. Thermal and mechanical properties of polyimide nanocomposites. In 2003 Annual report conference on electrical insulation and dielectric phenomena (pp. 120-123). IEEE.

21. Moradi, G., Zinadini, S. and Rahimi, M., 2023. Designing of the green γ-AlOOH@ Naringin thin film composite PVDF based nanofiltration membrane and application for pharmaceutical wastewater treatment. Journal of Environmental Chemical Engineering, 11(3), p.109952.

22. Hadi, J.M., Aziz, S.B., Mustafa, M.S., Hamsan, M.H., Abdulwahid, R.T., Kadir, M.F. and Ghareeb, H.O., 2020. Role of nano-capacitor on dielectric constant enhancement in PEO: NH4SCN: xCeO2 polymer nano-composites: Electrical and electrochemical properties. Journal of Materials Research and Technology, 9(4), pp.9283-9294.

23. Ghosh, S., Mondal, D., Roy, S., Roy, J., Bardhan, S., Mazumder, A., Bag, N., Basu, R. and Das, S., 2023. Water flow and finger-tapping mediated piezoelectric energy generation using a natural hematite-based flexible PVDF-HFP membrane. Journal of Materials Chemistry C, 11(39), pp.13418-13428.

24. Sivaprakash, P., Divya, S., Parameshwari, R., Saravanan, C., Sagadevan, S., Arumugam, S. and Esakki Muthu, S., 2020. Influence of Zn 2+ doping towards the structural, magnetic, and dielectric properties of NiFe 2 O 4 composite. Journal of Materials Science: Materials in Electronics, 31, pp.16369-16378.

25. Raza, Q., Bibi, I., Majid, F., Kamal, S., Ata, S., Ghafoor, A., Arshad, M.I., Al-Mijalli, S.H., Nazir, A. and Iqbal, M., 2023. Solar light-based photocatalytic removal of CV and RhB dyes using Bi and Al doped SrFe12O19 NPs and antibacterial properties. Journal of Industrial and Engineering Chemistry, 118, pp.469-482.

26. Kushwah, M., Sagar, R., Rogachev, A.A. and Gaur, M.S., 2019. Dielectric, pyroelectric and polarization behavior of polyvinylidene fluoride (PVDF)-gold nanoparticles (AuNPs) nanocomposites. Vacuum, 166, pp.298-306.

27. Sharmila, B., George, N., Sasi, S., V Antony, J., Chandra, J., Raman, V. and Nambath Purushothaman, D., 2022. A comprehensive investigation of dielectric properties of epoxy composites containing conducting fillers: fluffy carbon black and various types of reduced graphene oxide. Polymers for Advanced Technologies, 33(10), pp.3151-3162.

28. Sebastian, M.T., Ubic, R. and Jantunen, H., 2015. Low-loss dielectric ceramic materials and their properties. International Materials Reviews, 60(7), pp.392-412.

29. Defferriere, T., Klotz, D., Gonzalez-Rosillo, J.C., Rupp, J.L. and Tuller, H.L., 2022. Photo-enhanced ionic conductivity across grain boundaries in polycrystalline ceramics. Nature Materials, 21(4), pp.438-444.

30. Miclea, C., Tanasoiu, C., Amarande, L., Miclea, C.F., Plavitu, C., Cioangher, M., Trupina, L., Miclea, C.T. and David, C., 2007. Effect of temperature on the main piezoelectric parameters of a soft PZT ceramic. Rom. J. Inf. Sci. Technol, 10(3), pp.243-250.

31. Sezer, N. and Koç, M., 2021. A comprehensive review on the state-of-the-art of piezoelectric energy harvesting. Nano energy, 80, p.105567.

32. Zhu, Q., Wu, T. and Wang, N., 2023. From Piezoelectric Nanogenerator to Non-Invasive Medical Sensor: A Review. Biosensors, 13(1), p.113.

33. Shen, Z.Y. and Li, J.F., 2010. Enhancement of piezoelectric constant d33 in BaTiO3 ceramics due to nano-domain structure. Journal of the Ceramic Society of Japan, 118(1382), pp.940-943.

34. Mondal, D., Bardhan, S., Das, N., Roy, J., Ghosh, S., Maity, A., Roy, S., Basu, R. and Das, S., 2022. Natural clay-based reusable piezo-responsive membrane for water droplet mediated energy harvesting, degradation of organic dye and pathogenic bacteria. Nano Energy, 104, p.107893.

Chapter 5

MWCNT Intercalated Natural Hematite-based Activable Nanocomposite for Piezoelectric Energy Generation and ROS-Mediated Carcinogenic Dye Degradation

Chapter 5

MWCNT Intercalated Natural Hematite-based Activable Nanocomposite for Piezoelectric Energy Generation and ROS-Mediated Carcinogenic Dye Degradation

5.1 Introduction

In the previous chapters (Chapters 3 and 4), natural α-hematite nanoparticle-doped PVDF-HFP membrane and Gd incorporated natural α-hematite based PVDF-HFP membrane were used for energy harvesting as well as dye degradation purposes. The studies discussed in Chapter 4 revealed that the addition of Gd^{3+} into α-hematite nanoparticles enhanced their properties, leading to improved performance. Consequently, the PVDF-HFP membrane fabricated with Gd-incorporated hematite nanocomposites demonstrated superior outcomes in both dye degradation and energy generation compared to membranes containing pure α-hematite. Therefore, it can be stated that hematite-mediated nanocomposites improve the piezoelectric characteristics of PVDF-HFP more.

In this chapter, the studies on the developement of highly efficient piezoelectric nanocomposite membrane using functionalized multi-walled carbon nanotube (MWCNT) doped natural α-hematite nanoparticle (NPs)-based polyvinylidene fluoride-hexafluoropropylene (PVDF-HFP), which can harvest energy not only from finger tapping and water flow but also from wind energy, have been discussed. As the naturally available hematite has been used here the device becomes cost-effective, reusable, industrially practicable, and versatile [1] and the MWCNT has excellent electrical as well as physicochemical properties which enhance the polarizability and surface properties of the hematite NPs by introducing more charge carriers and accumulation charges leading towards the enhancement of the dielectric constant [2]. Thus, the incorporation of MWCNT-hematite into the PVDF-HFP matrix results in the rise in polarization (polar β-phase), and dielectric constant that has been measured in this work. The role of the polymer nanocomposite as a piezoelectric energy harvester and piezocatalyst was investigated in this chapter. Initially, X-ray diffraction (XRD), Field Emission Scanning Electron Microscope (FESEM), and Fourier transform infrared (FTIR) spectroscopy were used to study the properties of these polymer nanocomposites. The experimental and theoretical electrical properties of this nanocomposite showed significant piezoelectric polarisation, making it a viable material for piezoelectric applications. The piezo-response technology was utilized to generate piezoelectricity from mechanical perturbations such as finger tapping, water

flow, and wind flow [3]. This MWCNT incorporated hematite doped PVDF-HFP membrane was utilised to degrade organic dye i.e. RhB by piezocatalysis method in which under the influence of ultrasonic vibration, electron-hole pairs were generated on the surface of the membrane due to the development of piezo potential. These electron-hole pairs subsequently came into contact with hydroxyl ions, leading to the formation of reactive oxygen species (ROS). These ROS played a crucial role as the primary component responsible for the degradation of carcinogenic dyes from wastewater. Figure 5.1 shows the schematic representation of the application of MWCNT incorporated hematite-doped PVDF-HFP membrane. This flexible, reusable, cost-effective, super-efficient membrane has the potential to address energy and environmental challenges in the industrial and commercial sectors if properly improvised.
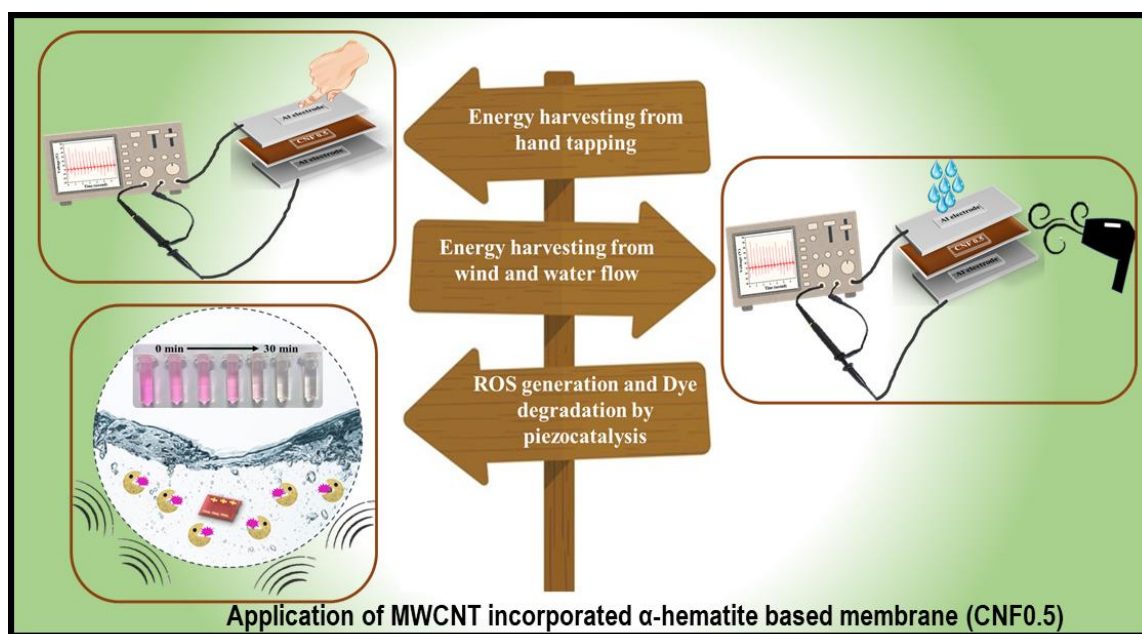
Figure 5.1 Schematic representation of the application of Chapter 5

5.2 Experimental details

5.2.1 Materials

The natural bulk hematite (α-hematite) was obtained from Bharat Engineering, Kolkata, India. Multi-walled carbon nanotube (MWCNT: diameter 50-90 nm, purity: > 95 %), polyvinylidene fluoride-hexafluoropropylene (PVDF-HFP: MW- 214.06 gm/mol), Terephthalic acid, ethylenediaminetetraacetic acid disodium salt dihydrate (EDTA), and p-

benzoquinone (BQ) were purchased from Sigma-Aldrich. Rhodamine B (RhB) was purchased from Loba Chemie Pvt. Ltd, acetone (HPLC-grade), and dimethylformamide (DMF) (HPLC grade) were obtained from Merck, India. All the analytical graded reagents have been used. Millipore water of 18.2 MΩ-cm resistivities has been used during the whole experiment.

5.2.2 Synthesis of MWCNT /α-hematite nanocomposites

The bulk natural hematite was cleaned at first, for removal of the impurities, and α-hematite nanoparticles were synthesized by the ball milling method illustrated in section 1.10.1 (Chapter 1) which was used for the further synthesis procedure.

To synthesize activated nano-hematite, 2 g of α-hematite nanoparticles were dissolved into the 80 ml DI water. After that, 20 µL of hydrochloric acid (37%) and 0.048 g hexamine were added to the prepared solution of hematite NP under 300 rpm stirring condition which was kept at 80 ⁰C overnight. Then the solution was filtered and dried to obtain activated hematite at 70°C. MWCNT was functionalized by chemical modification to synthesize the MWCNT-hematite nanocomposites. In a typical experiment, 50 mg of MWCNT was added to 15 mL ethanol and sonicated for 2 h to avoid agglomeration. The solution was dried and collected in powder form and then 15 mL of 3 (M) HNO_3 and the powder MWCNT were added to make a solution and stirred at 60 ⁰C for 15 minutes. After that, it was added to 15 mL H_2O_2 at 60 ⁰C under continuous stirring before rinsing with DI water. Then the precipitate was washed with the deionized water until the pH of the solution became neutralized. After that, it was dried and functionalized MWCNT was collected. Then it was added to surface-modified natural hematite using the condensation technique. Under ultrasonication, 1 g activated hematite was dissolved into 30 mL DMF and then MWCNT was added to this solution (1% w/w). Afterward, the solution was refluxed for 24 h at 90 ⁰C. Lastly, the solution was centrifuged and dried at 60 ⁰C to obtain MWCNT-incorporated hematite. Hence the collected MWCNT-hematite (CNFNP) was used for further work.

5.2.3 Synthesis of MWCNT-hematite incorporated nanocomposite membranes

To prepare the MWCNT-hematite polymer nanocomposite, MWCNT-hematite powder by varying weight percentages of 0%, 0.5%, and 1% respectively was added into 10 mL DMF solution. The suspension was stirred for 8 h at 60 ºC under 600 rpm with the help of a magnetic stirrer. The solution-casted method was used to fabricate the MWCNT/α-hematite membrane by casting the solution onto the Petri dishes. Then it was dried for 7 h at 70ºC and the free-standing membrane of 0%, 0.5%, and 1% MWCNT /α-hematite nanocomposite was collected and named as CNF0, CNF0.5, and CNF1 respectively. Figure 5.2 represents the whole synthesis procedure schematically.
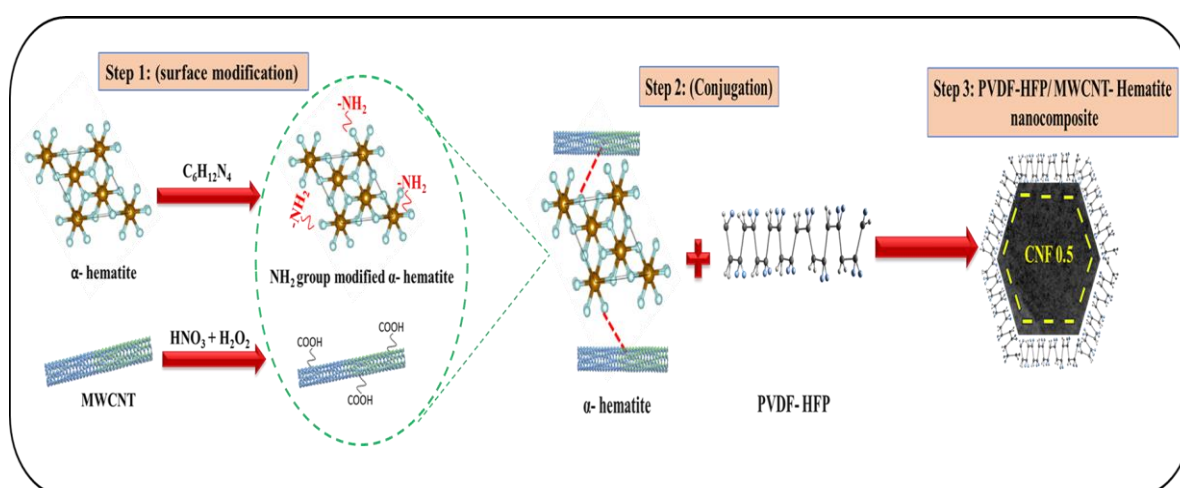
Figure 5.2 *Synthesis procedure of nanocomposite*

5.3 Result and discussion

5.3.1. Physicochemical characteristics of the sample

The structural properties and phase purity of natural hematite, CNT-doped hematite nanoparticles, and nanocomposite-incorporated membrane were analyzed by employing the X-ray diffraction technique (XRD) [4]. The XRD pattern of 1% CNT incorporated hematite nanoparticles (CNFNP) has been depicted in Figure 5.3 (a). The diffraction maxima found in the XRD pattern were well-matched with the JCPDS Card No. 72–0469. The absence of any other extra diffraction peak in the case of CNFNP confirmed the purity of the sample. The crystallographic and microstructural parameters were investigated by employing the

Rietveld refinement technique and tabulated in Table 5.1. It was found that with a very promising goodness of fitting (χ^2: 1.32) the microstrain and crystallite size of the CNFNP nanocomposite was higher than the pristine hematite NPs (Table 5.1). This result suggested that the MWCNT in pristine hematite created stress as a result the microstructural parameters were enhanced which was in very good agreement with the enhanced active sites in the nanocomposite sample. In reality, foreign MWCNT generates stress in the structure of hematite and creates oxygen vacancies which augmented the surface properties and microstructural properties in nanocomposite. The unit cell was visualized by Vesta v3.4.3 (visualization for electronic and structural analysis) software shown in Figure 5.3(b).

Table 5.1 *Refined parameters of pure hematite and MWCNT-doped hematite nanoparticles*

Parameters	α-Hematite NP	CNFNP
a (Å)	5.038	5.033
b(Å)	5.038	5.033
c(Å)	13.761	13.745
alpha (⁰)	90	90
beta (⁰)	90	90
gamma (⁰)	120	120
Size (Å)	423.187	886.110
Strain	0.00045	0.0035
R_p %	18.42	22.92
R_{wp} %	24.31	39.73
χ^2	1.32	1.73

On the other hand, the X-ray diffractograms of three different percentages of CNF-doped PVDF-HFP i.e. CNF0, CNF0.5, and CNF1 have been represented in Figure 5.3(c). It was found that the intensity of the diffraction maxima at 20.1° which was responsible for the formation of polar β-phase was enhanced with increasing CNF percentage and found maximum in the case of CNF0.5.

Figure 5.3 *XRD Analysis of (a) CNT incorporated hematite NP, (b) Microstructural visualization of unit cell from VESTA software, (c) X-ray diffractograms of the nanocomposite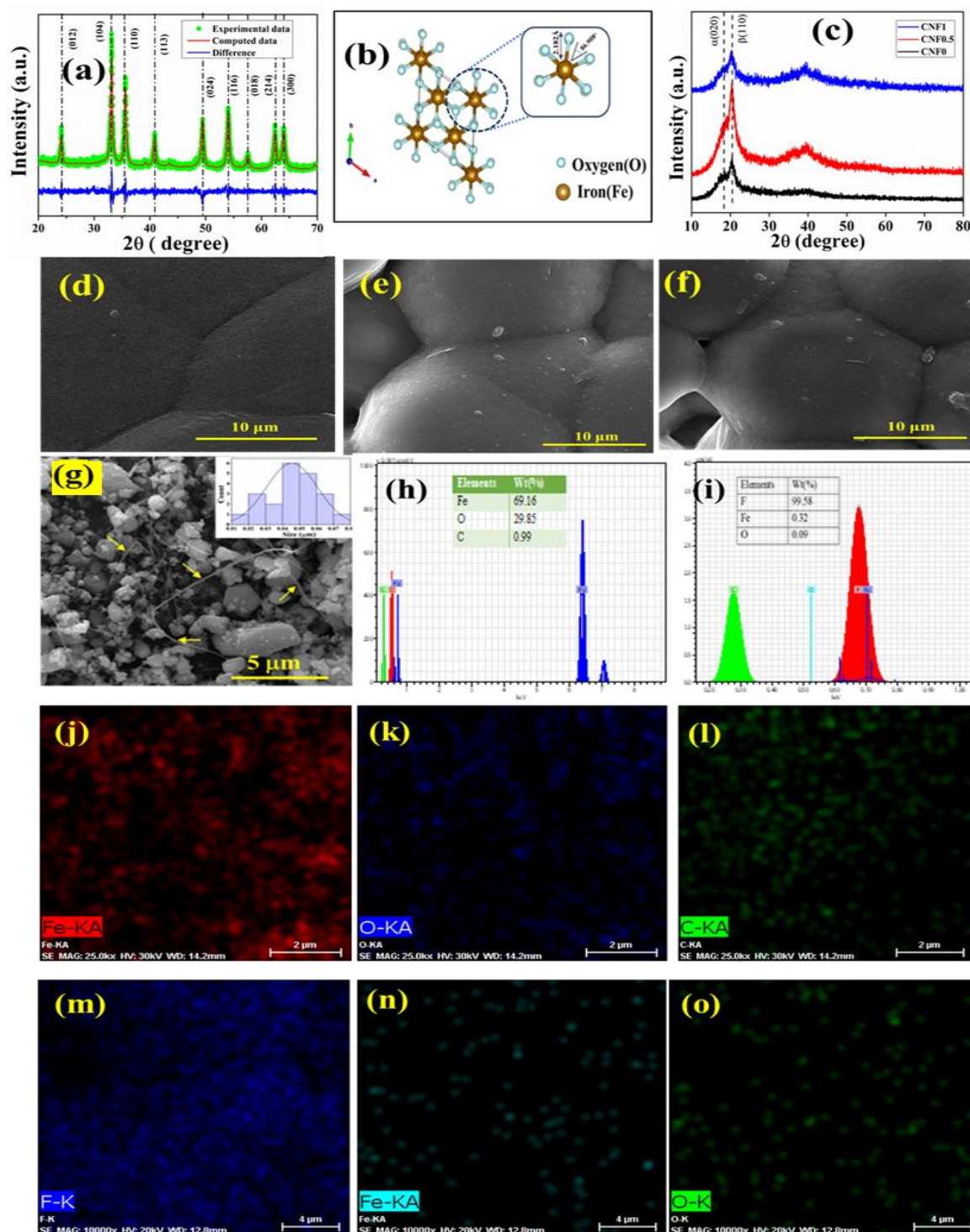 membranes, (d-g) FESEM images of CNF0, CNF0.5, CNF1, and CNFNP, (h, i) EDAX spectra of CNFNP and CKF0.5, Elemental mapping of (j-l) CNFNP and m-o) CNF0.5.*

Whereas, the over-doping of nanocomposite in the polymer matrix reduced its β-phase intensity in CNF1 which validated that the CNF0.5 nanocomposite membrane possessed a maximum polar phase [5]. In reality, the enhanced surface properties and active sites of the nanofillers increase the polar phase of PVDF polymer up to a certain limit after that the electro-active moiety of the PVDF chain is disoriented upon excess doping, and a reduction of polar phases occurs.

The surface properties and morphological characteristics were studied using FESEM [6]. The presence of MWCNT was observed in hematite NPs, confirming the successful nanofillers incorporation [Figure 5.3 (g)]. The size distribution of hematite NPs in MWCNT-incorporated hematite NPs was found nearly 40-50 nm using the FESEM micrograph with the help of ImageJ Software [Figure 5.3(h)]. On the other hand, the FESEM images of CNF0, CNF0.5, and CNF1 membranes are depicted in Figure 5.3(d-f). The nanofillers growth was observed in the CNF0.5 and CNF1 membranes and the increased spherulite morphology along with roughness were also visible in the CNF0.5, and CNF1 membranes compared to CNF0. This spherulite structure ensures the formation of polar β-phase depending on the crystallinity in the material as it is associated with the alignment of the molecular chain, which is greater than the bare PVDF membrane i.e. CNF0 [7,8]. The molecular chains are folded together in an organized manner producing an ordered region known as lamellae forms during the cooling period from the melting condition [5]. This spherulite, which is made up of these lamellae, confirms the crystallinity and the formation of the β-phase in the PVDF matrix. Hence the elevated diameter of the spherulite structure, together with the smooth and homogeneous surface confirmed the lowest polar phase in CNF0 [9,10].

The elemental compositions and stoichiometric ratios of Fe, O, F, and C in the CNF0.5 nanocomposite membrane were analyzed with EDX measurement to confirm the presence of elements and depicted in Figure 5.3(i). It was found that the elements of CNFNP and PVDF were both present in the CNF0.5 nanocomposite membrane with a proper stoichiometric ratio which validated the successful fabrication of the nanocomposite membrane. The mapping data of CNFNP and CNF0.5 depicted a homogeneous distribution of Fe, O, C in CNFNP and Fe, O, F in the PVDF matrix by the proper stoichiometric ratio [Figure 5.3(j-o)].

The FTIR analysis was employed to understand the formation of bonding networks in the nanocomposite as well as the polar β-phase content in nanocomposite membranes [11-12].
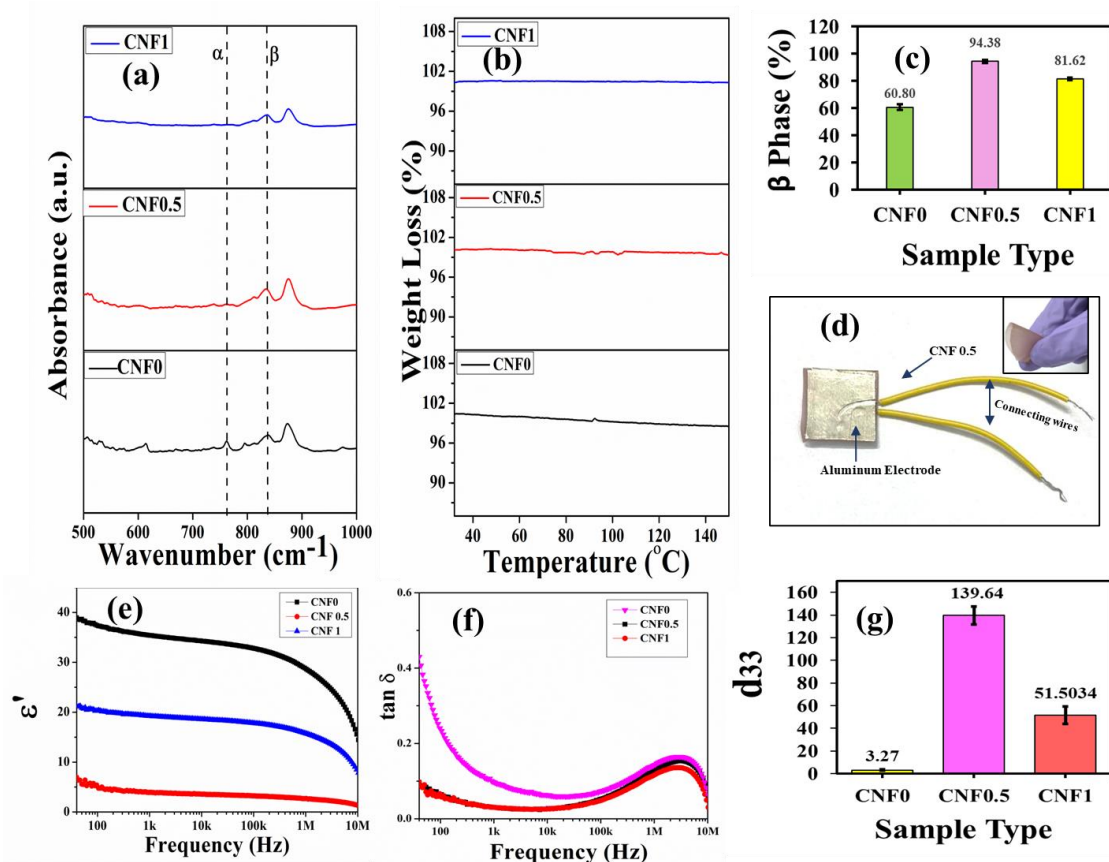
Figure 5.4 *(a) FTIR Spectra of CNF0, CNF0.5, CNF1 (b) Thermogravimetric analysis of the nanocomposite membranes, (c) Percentage of beta phases of the membranes, (d) Fabricated device, (e) Dielectric constants of membranes, (f) Tangent losses, (g) Piezoelectric coefficients of the nanocomposite membranes.*

The FTIR images of the three samples CNF0, CNF0.5, and CNF1 have been shown in Figure 5.4(a). The peak visible nearly 975 cm^{-1} (-CH$_2$ rocking) and 794 cm^{-1} (-CH$_2$ rocking), 765 cm^{-1} and 613 cm^{-1} (-CF$_2$ bending and skeletal bending), 533 cm^{-1} (-CF$_2$ bending) corresponds to the α-phase of the film [13-14]. Another phase i.e. the γ phase nearly at 1234 cm^{-1} was also observed in CNF0. The peak observed at 840 cm^{-1} (CH$_2$ rocking, CF$_2$ stretching, and skeletal C-C stretching), 600 cm^{-1} (CF$_2$ wagging), and 510 cm^{-1} (CF$_2$ stretching) represented the formation of the β-phase [13,14]. It was observed from the FTIR spectra that the peak corresponding to the β-phase was elevated in the case of CNF0.5 compared to the other two samples [Figure 5.4(a)]. Hence, the enhancement of

the polarization due to the realignment of the CF_2 bond in CNF0.5 was confirmed. The fraction of β-phase developed in the material was calculated from the Lambert-Beer law stated in equation 1.8 (Chapter 1).

It was found that the percentage of β-phase of the nanocomposite membranes [Figure 5.4(c)] increased with increasing doping percentage of nanofillers and reduced after a certain critical limit. The percentage of β-phase of the pristine PVDF-HFP (CNF0), CNF0.5, and CNF1 were 60.80 %, 94.38 %, and 81.62 % respectively. In reality, the augmented surface properties of nanofillers (CNFNP: Zeta potential -16.5 mV: Appendix A3.1) enhanced the β-phase formation by fluffing the electropositive $-CH_2$ groups and electronegative $-CF_2$ groups to the opposite side of carbon chain by electrostatic interaction. After a certain limit of nanofillers incorporation in a polymeric system, the extra surface charge reduced the β-phase formation probability by disrupting the periodic arrangement of CH_2 and CH_2 bond as a result over incorporation of nanofillers portrayed a reduction in percentage β-phase (CNF1) [15]. This enhanced polar β-phase of CNF0.5 made it suitable for piezo-responsive applications which was consistent with the XRD and FESEM data.

5.3.2 The electrical properties and piezoelectric coefficient

The dielectric constant (D.C) of any sample is another vital characteristic to the determination of the polarization properties [16]. The dielectric constant contains one real part and one imaginary part representing dielectric permittivity (ε') and tangent loss or dissipation factor (ε'') respectively which were derived with the help of the formula mentioned in equation 1.9 and 1.10 (Chapter 1).

The membrane of 2×2 cm was taken and aluminum electrodes were connected on both sides of the membrane through which wires were connected to measure the electrical properties by a HIOKI, IM 3536 LCR meter keeping a bias voltage of 0.5 V in a frequency range of 40 Hz to 10 MHz. The dielectric constant and tangent loss were examined for the hematite nanoparticles, CNFNP, and three membranes (CNF0, CNF0.5, and CNF1). The dielectric constant of CNFNP was 1.8×10^5, while pure hematite nanoparticles exhibit ~300 (Figure A3.2). This indicates that the integration of multi-walled carbon nanotubes (MWCNT) into natural hematite nanoparticles enhances polarization. Therefore, MWCNT-incorporated hematite NPs were introduced into a PVDF-HFP matrix to boost membrane polarization. In the case of membranes, the maximum dielectric constant was found for the CNF0.5 (39.03) membrane whereas the other two (CNF0, CNF1) exhibited D.C values 6.68 and 21.48

respectively at 40 Hz. Figure 5.4(e) represents the dielectric constants (D.C) for CNF0, CNF0.5, and CNF1 with varying frequencies. The dielectric constant was observed to be decreased with increasing frequencies. The Maxwell-Wagner interfacial polarization could adequately explain the reason for this phenomenon [17-18]. In the dielectric material, nonconductive grain boundaries separate the conducting grains of the dielectric material. The external electric field in the low-frequency region is not enough to pull out the conductive grain which creates dipoles and hence the polarisation [19]. In high-frequency regions, the dipoles could not change their orientation quickly with the field thus the dielectric constant reduced [20]. It was evident from the dielectric constant determination that the CNF0.5 unveiled maximum D.C with a nominal tangent loss which validated that CNF0.5 showed maximum polarization property [Figure 5.4(f)]. In reality, the maximum polar β-phase in CNF0.5 was responsible for this high D.C which also validated the maximum intrinsic polarization of the membrane which made the membrane a promising piezo-responsive nanocomposite.

On the other hand, the DFT calculation showed the theoretical dipole moment of CNF0.5 was greater than the CNF0. The dipole moment increased from 11.486 Debye to 13.193 Debye. The single point energy for CNF0.5 was -2671.7599 and in the case of CNF0 was -2770.976. The non-zero frequency modes of the calculation validated its authenticity. This high negative energy value corresponded to the stability of the nanocomposite systems. This enhancement in theoretical values of electrical parameters also validated the increased polarizations in experimental results (XRD, FTIR, FESEM) and made the CNF0.5 membrane a potential candidate for piezo-responsive applications.

Further, the piezo-responsive properties of the nanocomposite membranes were estimated by calculating the piezoelectric coefficients using equation 3.1 (Chapter 3). The CNF0.5 membrane exhibited the maximum value of d_{33} (139.64 pC/N) whereas the d_{33} for CNF0 and CNF1 membranes were 3.27 pC/N and 51.50 pC/N respectively. The value of d_{33} for the three membranes is depicted in Figure 5.4(g). These high values of d_{33} in the CNF0.5 nanocomposite membrane validated the experimental data of XRD, FESEM, FTIR studies. The electrical properties and theoretically calculated value of polarization by DFT indicated that this membrane acquired maximum polarization, hence maximum piezo-response. For such favourable property, CNF0.5 was studied for piezo-responsive applications like energy generation and wastewater remediation [21].

5.3.3 Generation of piezoelectric energy using the nanocomposite membrane

As the CNF0.5 membrane displayed maximum piezo-response in experimental and theoretical characterizations thus it was utilized for the fabrication of a device that could harvest piezoelectric energy. A 2×2 cm CNF0.5 membrane was taken which would act as the primary layer of the device and two aluminum electrodes along with copper wires were mounted on both sides of the primary layer forming a sandwich structure. The sandwich-structured device was encapsulated with the polyethylene terephthalate (PET) cover to provide a barrier against all types of harm like mechanical damage, water splashes, etc. The image of the device is shown in the Figure. 3 (d).

The open circuit piezoelectric voltage was measured by DSO under periodic hand-tapping of force 13.91 N (S2) and this was found to be 51.8 V. The open circuit output voltage is shown in Figure 5.5(a). The instantaneous short circuit current was measured using the DAQ6510 multi-meter system, Keithley which is found to be 11.6 μA [Figure 5.5(b)]. Subsequently, the power density was calculated using equation 3.2 (Chapter 3) maintaining the volume of the device i.e. $2 \times 2 \times 0.018$ cm^3. Henceforward, the power density has been determined to be 8.684 mW/cm^3 which is quite significant.

Further renewable mechanical energy sources like water flow and wind energy were employed for piezoelectric energy generation by the CNF0.5 nanocomposite device. Here, water flow was generated with an overhead stirrer and the CNF0.5 membrane-mediated device was placed in the vicinity of the water flow. This flow of water acted as the external stimulus and helped to generate instantaneous output voltage due to the flow. The output voltage due to water flow was recorded as nearly 7.2 V shown in Figure 5.5(c).

Additionally, this device can also harvest another waste mechanical impulse (wind flow) mediated piezoelectric energy. The device was positioned in front of the wind flow generated by a hair drier (1000 W, air pressure 40 N/m^2), which developed an output voltage of 0.6 V [Figure 5.5(d)]. It was obtained that the water flow and wind flow generated quite a promising amount of piezoelectric energy, which may open up a path for mitigating the energy crisis and may be a valuable alternative to fossil fuels. In both cases, the water and wind flow acted as external mechanical stimuli to harvest energy. The detailed mechanism had already been mentioned elaborately in section 1.7.2 (Chapter 1).
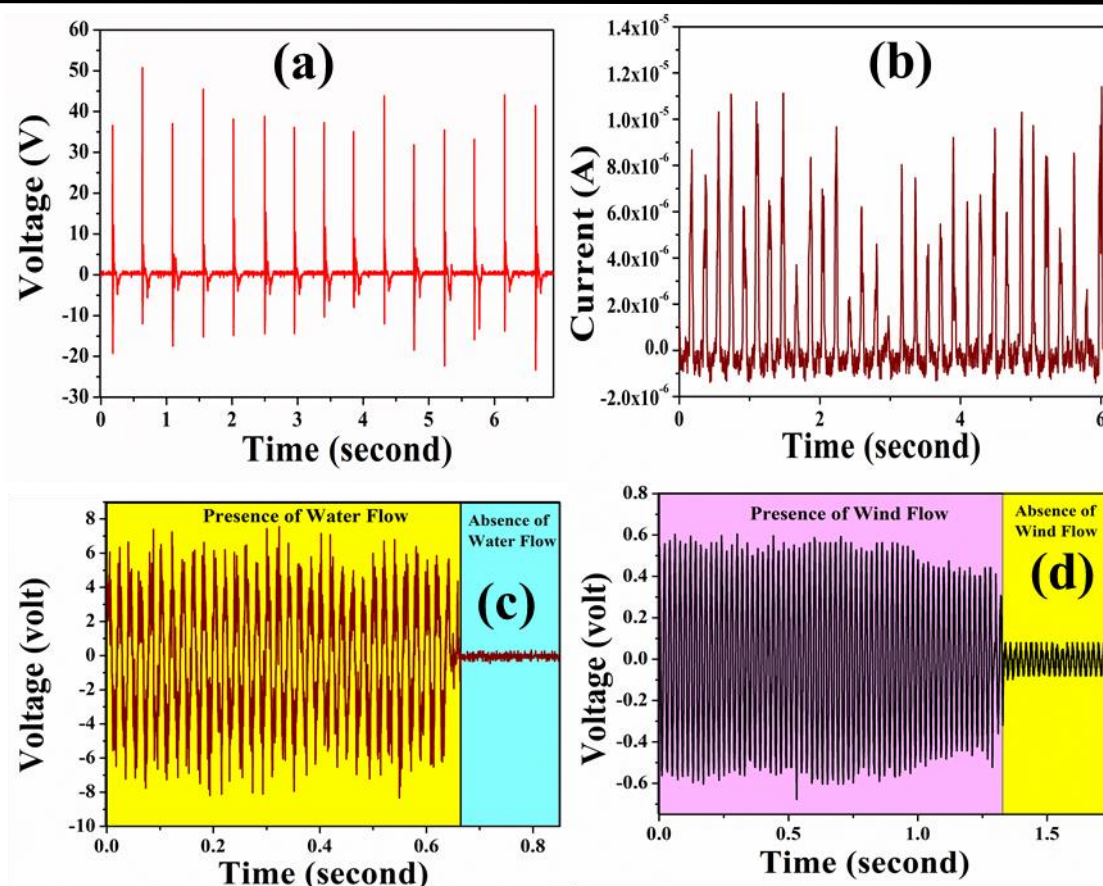
Figure 5.5 *(a, b) Piezoelectric output voltage and current by finger tapping, (c, d) Piezoelectric voltage generation by wind flow, and water flow*

5.3.4 Industrial dye degradation by piezocatalysis

The CNF0.5 membrane was further employed for piezocatalytic the degradation of RhB dye as it exhibited the highest polarisation, the β-phase, and d_{33} value. Hence 2×2 cm^2 CNF0.5 film was been taken for the piezocatalytic experiments. RhB dye, one of the carcinogenic dyes, was initially taken in a 15 mL glass vial which was placed into an ultrasonic bath sonicator with a frequency of 33 ± 5 kHz (Telsonic Ultrasonic Bath Sonicator), and the sample was immersed into the dye solution to continue the process of dye degradation by the piezo catalysis method. However, to ensure full adsorption, the sample was immersed in the RhB solution for at least 30 minutes before beginning the experiment, which revealed a very low adsorption percentage. The entire experiment was carried out in complete darkness to avoid any photonic interaction during the test. A temperature-controlled water bath system was employed to remove the ultrasound-mediated heating. After each 10-

minute interval, the solution was taken out from the vial and collected to study the degradation kinetics using a Lambda 25 UV-visible spectrophotometer.

The decoloration of the RhB dye was observed after 30 min and the degradation percentage of RhB dye was nearly about 98.7% which is quite satisfactory, shown in Figure 5.6 (a). The percentage of degradation of dye concentration (η) was analyzed using the following relation 3.6 (Chapter 3).
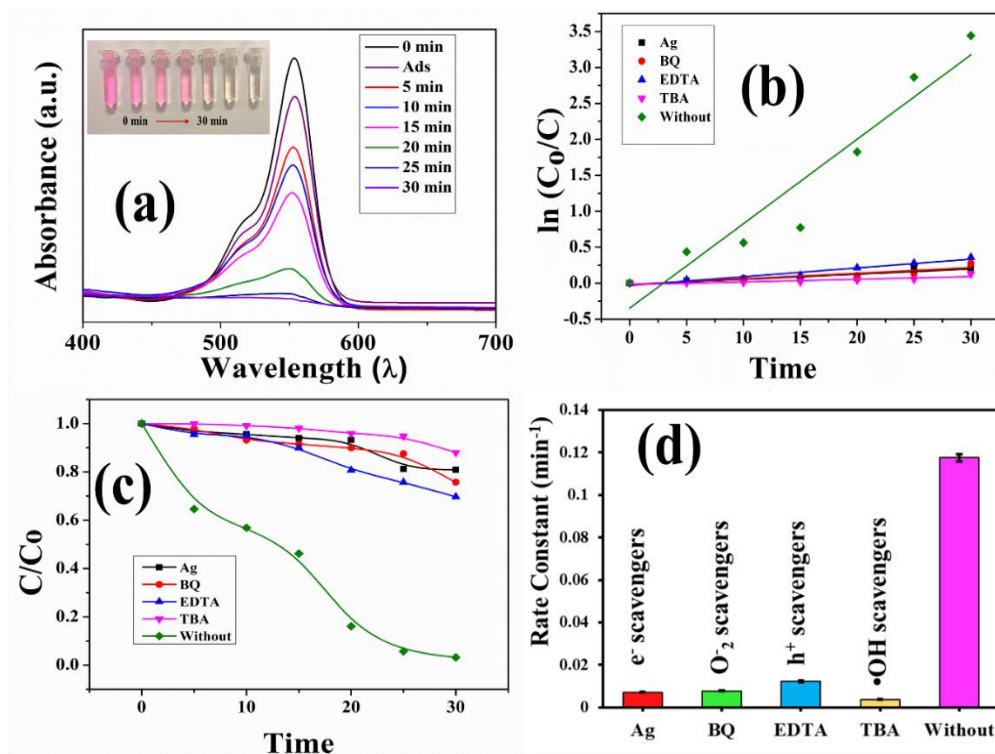
Figure 5.6 *(a) RhB dye degradation in 30 min, (b) First order reaction kinetics by different scavengers, (c) Degradation of dye using different scavengers, (d) Reaction rate constant of different scavengers*

The production of ROS through piezocatalysis was validated by the ROS scavenging experiments, which confirmed the dominant ROS responsible for the experiment [22]. The ethylenediaminetetraacetic acid (EDTA), silver nitrate ($AgNO_3$), tertbutanol (TBA), and p-benzoquinone (BQ) were utilized as scavengers of hole (h^+), electron (e^-), hydroxyl radicals ($\bullet OH$), and superoxide radicals ($\bullet O_2^-$) respectively [23]. Due to the addition of these scavengers, the formation of ROS i.e. hole (h^+), electron (e^-), hydroxyl radicals ($\bullet OH$), and superoxide radicals ($\bullet O_2^-$) hampered [24]. Hence the most active ROS responsible for the degradation of the dye has been more trapped by that particular scavenger which aids in

identifying the most dominating ROS [25]. In this experiment, with the addition of EDTA, $AgNO_3$, TBA, and BQ the percentage of degradation was decreased as these scavengers affected the rate constant of the piezocatalysis reaction [Figure 5.6(d)].

The kinetics of the reaction have been depicted in Figure 5.6(b-c). The rate constant after adding $AgNO_3$, BQ, EDTA, and TBA in the dye solution the rate constant became 0.00361, 0.00391, 0.00611, and 0.00186 min^{-1} respectively whereas the reaction rate without adding the scavenging elements was 0.05873 min^{-1} calculated using the formula stated in equation 3.7 (Chapter 3). Hence, the addition of scavengers slackened the process of piezocatalysis and for TBA, this process was lowest, ensuring that the degradation of the dye was due to the creation of more •OH. This degradation experiment suggested that the CNF0.5 membrane decomposed carcinogenic organic RhB dye with 98.7 % degradation efficiency with a high first-order reaction kinetics of 0.05873 min^{-1}. This promising piezocatalytic efficiency made this membrane an effective wastewater remediator for mitigating water pollution. The dye degradation using piezocatalysis was accomplished by employing the method referred to as the screening charge effect, which is elaborated on in detail in Chapter 1, section 1.8.1.

5.3.5 Figure of merit of the CNF0.5 nanocomposite membrane

The nanocomposite membrane exhibited promising thermal stability and flexibility, making it applicable in a long range of environmental conditions. The thermogravimetric analysis (TGA) of the nanocomposite membranes in Figure 5.4(b) suggested that the device was stable up to a temperature as high as 150 $^{\circ}$C. The utilization of water flow as mechanical energy for electrical energy conversion, as well as the employment of wind energy, was another fascinating aspect of this research. It was observed that the efficiency of the device was not altered much even after 60 days, indicating its reusability [Figure 5.7(b)]. The output voltage under the flow of water and wind were 7.2 V and 600 mV respectively, whereas finger tapping resulted in voltage generation of magnitude 51.8 V. Furthermore, the membrane also showed the excellent ability to degrade carcinogenic dye i.e RhB almost 98.7% in only 30 minutes using the piezocatalysis method [Figure 5.7(a)]. The efficacy of piezocatalysis remained almost unaltered even after 5 cycles. The thermal stability, energy generation, and dye degradation stability of the CKF0.5 membrane made it reusable and stable in environmental alteration.
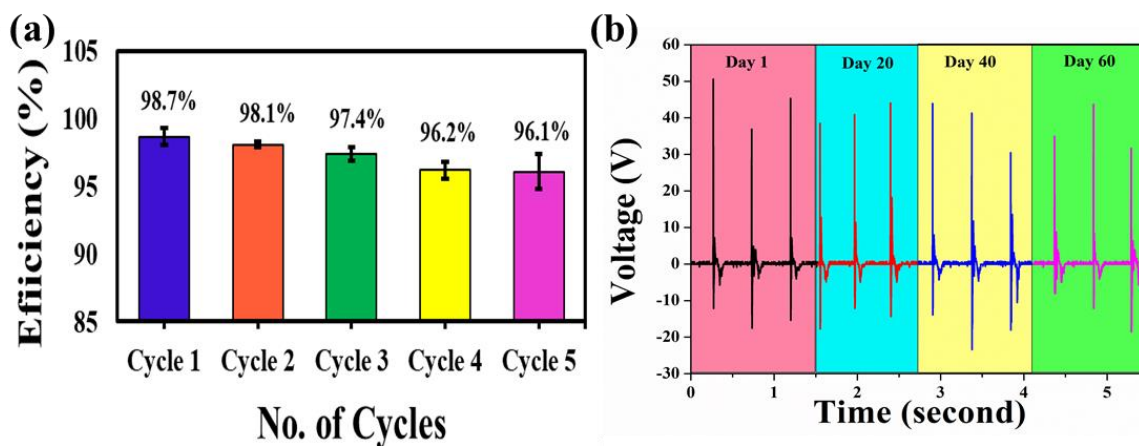
Figure 5.7 *Recyclability test of CNF0.5 nanocomposite membranes in terms of (a) Dye degradation, (b) Energy generation*

5.4 Summary

This work describes the successful synthesis of MWCNT-doped natural hematite nanoparticles incorporated in self-poled, free-standing PVDF-HFP membrane by varying the percentage of MWCNT-doped hematite (CNF0, CNF0.5, CNF1) and applying this to fabricate a device that enables piezoelectric energy harvesting from different renewable mechanical sources. The physicochemical properties of all samples have been analyzed and CNF0.5 has shown maximum polarizability (D.C: 39.03, Dipole moment by DFT calculation: 13.193 Debye), polar β-phase (94.38 %) which is the basic requirement for being a piezoresistive material. The piezoelectric energy generated by tapping a finger (13.91 N), water flow, and wind flow are portrayed in this chapter, the values of voltages being 51.8 V, 7.2 V, and 600 mV respectively. The membrane has also been used for carcinogenic organic dye degradation purposes which degrades the RhB only in 30 mins by 98.7% which is quite significant and it remains constant for up to 5 cycles validating the reusability of the membrane for industrial purposes. Hence this natural nanomaterial-based reusable membrane enables generating piezo voltage from renewable mechanical energy sources as well as degrading carcinogenic dye can be a riveting and eccentric way to battle the energy crisis and water pollution while also achieving futuristic development.

References

[1] Ghosh, S., Mondal, D., Roy, S. and Das, S., 2023. Recent advances in the synthesis and biomedical applications of α-hematite nanoparticles. *Sayam-A Journal of Science*, *1*(1), pp.01-08.

[2] Shukla, V., 2019. Review of electromagnetic interference shielding materials fabricated by iron ingredients. *Nanoscale Advances*, *1*(5), pp.1640-1671.

[3] Mariello, M., Fachechi, L., Guido, F. and De Vittorio, M., 2021. Multifunctional sub-100 μm thickness flexible piezo/triboelectric hybrid water energy harvester based on biocompatible AlN and soft parylene C-PDMS-Ecoflex™. *Nano Energy*, *83*, p.105811.

[4] Roy, S., Bardhan, S., Chanda, D.K., Roy, J., Mondal, D. and Das, S., 2020. In situ-grown Cdot-wrapped Boehmite nanoparticles for Cr (VI) sensing in wastewater and a theoretical probe for chromium-induced carcinogen detection. *ACS Applied Materials & Interfaces*, *12*(39), pp.43833-43843.

[5] Geng, C., He, S., Yu, S., Johnson, H.M., Shi, H., Chen, Y., Chan, Y.K., He, W., Qin, M., Li, X. and Deng, Y., 2024. Achieving Clearance of Drug-Resistant Bacterial Infection and Rapid Cutaneous Wound Regeneration Using An ROS-Balancing-Engineered Heterojunction. *Advanced Materials*, p.2310599.

[6] Jothi Prakash, C.G. and Prasanth, R., 2021. Approaches to design a surface with tunable wettability: a review on surface properties. *Journal of Materials Science*, *56*, pp.108-135.

[7] Ghosh, S., Mondal, D., Roy, S., Roy, J., Bardhan, S., Mazumder, A., Bag, N., Basu, R. and Das, S., 2023. Water flow and finger-tapping mediated piezoelectric energy generation using a natural hematite-based flexible PVDF-HFP membrane. *Journal of Materials Chemistry C*, *11*(39), pp.13418-13428.

[8] Chen, M., Wang, Y. and Zhao, Z., 2022. Monolithic metamaterial-integrated graphene terahertz photodetector with wavelength and polarization selectivity. *Acs Nano*, *16*(10), pp.17263-17273.

[9] An, Z., Yokota, H., Kurihara, K., Hasegawa, N., Marton, P., Glazer, A.M., Uesu, Y., Ren, W., Ye, Z.G., Paściak, M. and Zhang, N., 2023. Tuning of Polar Domain Boundaries in Nonpolar Perovskite. *Advanced Materials*, *35*(11), p.2207665.

[10] Ye, K., Yan, J., Liu, L., Li, P., Yu, Z., Gao, Y., Yang, M., Huang, H., Nie, A., Shu, Y. and Xiang, J., 2023. Broadband Polarization-Sensitive Photodetection of Magnetic Semiconducting MnTe Nanoribbons. *Small*, *19*(29), p.2300246.

[11] Roy, S., Bardhan, S., Mondal, D., Saha, I., Roy, J., Das, S., Chanda, D.K., Karmakar, P. and Das, S., 2021. Polymeric carbon dot/boehmite nanocomposite made portable sensing device (Kavach) for non-invasive and selective detection of Cr (VI) in wastewater and living cells. *Sensors and Actuators B: Chemical*, *348*, p.130662.

[12] Choi, J.Y., Check, B., Fang, X., Blum, S., Pham, H.T., Tayman, K. and Park, J., 2024. Photocatalytic Hydrogen Peroxide Production through Functionalized Semiconductive Metal–Organic Frameworks. *Journal of the American Chemical Society*.

[13] Ghosh, S., Bardhan, S., Mondal, D., Sarkar, D., Roy, J., Roy, S., Basu, R. and Das, S., 2023. Natural hematite-based self-poled piezo-responsive membrane for harvesting energy from water flow and catalytic removal of organic dye. *Ceramics International*, *49*(9), pp.14710-14718.

[14] Lewis, S.L., Russell, L.M., Saliba, G., Quinn, P.K., Bates, T.S., Carlson, C.A., Baetge, N., Aluwihare, L.I., Boss, E., Frossard, A.A. and Bell, T.G., 2022. Characterization of sea surface

microlayer and marine aerosol organic composition using STXM-NEXAFS microscopy and FTIR spectroscopy. *ACS Earth and Space Chemistry*, *6*(7), pp.1899-1913.

[15] Ruan, L., Yao, X., Chang, Y., Zhou, L., Qin, G. and Zhang, X., 2018. Properties and applications of the β phase poly (vinylidene fluoride). *Polymers*, *10*(3), p.228.

[16] Venkatesh, M.S. and Raghavan, G.S.V., 2005. An overview of dielectric properties measuring techniques. *Canadian biosystems engineering*, *47*(7), pp.15-30.

[17] Vu, T.T.N., Teyssedre, G., Le Roy, S. and Laurent, C., 2017. Maxwell–Wagner effect in multi-layered dielectrics: interfacial charge measurement and modelling. *Technologies*, *5*(2), p.27.

 [18] Prodromakis, T. and Papavassiliou, C., 2009. Engineering the Maxwell–Wagner polarization effect. *Applied Surface Science*, *255*(15), pp.6989-6994.

[19] Revil, A., 2013. On charge accumulation in heterogeneous porous rocks under the influence of an external electric field. *Geophysics*, *78*(4), pp.D271-D291.

[20] Wang, H. and Yang, L., 2023. Dielectric constant, dielectric loss, conductivity, capacitance and model analysis of electronic electroactive polymers. *Polymer Testing*, *120*, p.107965.

[21] Mondal, D., Bardhan, S., Das, N., Roy, J., Ghosh, S., Maity, A., Roy, S., Basu, R. and Das, S., 2022. Natural clay-based reusable piezo-responsive membrane for water droplet mediated energy harvesting, degradation of organic dye and pathogenic bacteria. *Nano Energy*, *104*, p.107893.

[22] Bag, N., Roy, J., Mondal, D., Ghosh, S., Bardhan, S., Roy, S., Bhandary, S. and Das, S., 2024. Utilization of experimental and theoretical piezoresponse of BTO nanocrystal for rapid decomposition of the pathogenic coliform bacteria. *Ceramics International*, *50*(5), pp.7998-8009.

[23] Wang, Y., Xu, Y., Dong, S., Wang, P., Chen, W., Lu, Z., Ye, D., Pan, B., Wu, D., Vecitis, C.D. and Gao, G., 2021. Ultrasonic activation of inert poly (tetrafluoroethylene) enables piezocatalytic generation of reactive oxygen species. *Nature communications*, *12*(1), p.3508.

[24] Hong, M., Yao, J., Rao, F., Chen, Z., Gao, N., Zhang, Z. and Jiang, W., 2023. Insight into the synergistic mechanism of sonolysis and sono-induced BiFeO3 nanorods piezocatalysis in atenolol degradation: Ultrasonic parameters, ROS and degradation pathways. *Chemosphere*, *335*, p.139084.

[25] Roy, J., Roy, S., Mondal, D., Bag, N., Chowdhury, J.R., Ghosh, S., Bardhan, S., Mondal, R., Basu, R. and Das, S., 2024. Gd-doped bismuth ferrite nanocomposite: A promising candidate for piezocatalytic degradation of organic dyes and pathogenic E. coli. *Surfaces and Interfaces*, *44*, p.103579.

Chapter 6

Conclusion & Outlooks

Chapter 6

Conclusion & Outlooks

The world is facing an unprecedented energy crisis, caused by rapidly decreasing fossil fuel reserve, rising energy demand, and the terrible environmental consequences due to our existing energy production systems. Addressing this crisis requires a multifaceted strategy. With the depletion of fossil fuel supplies, environmental concerns, and geopolitical conflicts, it is clear that a shift to sustainable and renewable energy sources is not only desired but also necessary. However, this transformation must be carefully orchestrated to assure fair access, financial solidity, and eco-sustainability.

In addition to this, another major concern is water pollution, which is a serious and widespread problem nowadays. Industrial waste, sewage, agricultural runoff, oil spills, and other pollutants contaminate our scarce freshwater sources, endangering human health, ecosystems, and the entire aquatic food chain. Failure to prevent this poisonous tide might leave significant sections of the world's water supply undrinkable and inhabitable for a variety of animals. Henceforth, water pollution must be mitigated and reversed through an innovative, cost-effective, and nontoxic method. One of the ubiquitous and widely available iron oxide rock minerals i.e. α-hematite has been selected for this research work due to its biocompatibility, nontoxicity, and significant surface and electrical properties. The properties of the natural α-hematite have been enhanced by incorporating various dopants and then it is used to address both the energy crisis as well as water pollution by fabricating piezo-responsive polymer nanocomposites by the conjugation with PVDF-HFP. The widespread availability of α-hematite and its enhanced physicochemical properties with modification increases the surface interaction with PVDF-HFP polymer and fabricated promising nanocomposite membranes for tackling these global concerns.

In Chapter 2, the collected natural α-hematite has been nanonized by top-down method by avoiding any chemical and synthetic route. The nanonization of the bulk natural α-hematite has been achieved by ball milling technique and then the α-hematite in nano form as well as in bulk form have been characterized to study their several properties such as structural, morphological, electrical, etc by several techniques which reveal that the dielectric permittivity (~ 400), purity (99.21%), etc. have been improved in nano α-hematite. Hence, nanonized α-hematite has been selected further for other experimental procedures.

In Chapter 3, the nanosized natural α-hematite with improved properties has been applied to fabricate devices for answering problems like energy crisis and water pollution by incorporating it into the well-known piezoresposive fluoropolymer (PVDF-HFP). Here, the nanosized natural α-hematite with varying weight percent has been incorporated in the PVDF-HFP matrix to modulate the properties of the membrane such as dielectric constant, polarisation, β-phase, etc which are the key parameters of piezoelectric properties. Several characterization techniques have been employed to identify the optimal α-hematite doped membrane which is PVF5 (5% α-hematite doped PVDF) in this case. This PVF5 membrane has been used to fabricate a device that is capable of generating open circuit voltage of 42 V and the short circuit current of 0.898 μA due to hand tapping whereas 5 V has been obtained due to water flow. This membrane can also degrade a carcinogenic dye namely RhB with 94.1% within just 40 min. Hence, this biodegradable natural hematite NPs doped PVDF film, is competent to act as a nano piezoelectric energy harvester with additional capability to degrade dye via piezocatalysis.

Chapter 4 describes a study of the doping of rare earth material i.e. Gd^{3+} into the natural hematite NPs to enhance the properties of the NPs. The incorporation of Gd^{3+} into hematite natural rock NPs significantly increases polarisation due to the large positive surface charge of the resultant nanocomposite. Despite the negative surface charge of natural hematite, the

addition of a small quantity of rare earth metal produces oxygen vacancies and microstrain, resulting in active sites. Hence, Gd^{3+} incorporated hematite has been doped into the PVDF-HFP matrix to enhance its polarization, β-phase nucleation, and piezoelectric properties and create a solid-state device capable of harvesting 16.92 V and 8V from finger tapping and water flow, respectively, and degrading RhB dye by 94.7% in 35 minutes. As a result, Gd^{3+}-hematite NPs incorporate a free-standing, reusable PVDF membrane providing another way for device fabrication which can eliminate both the issue of energy crisis as well as water pollution.

In Chapter 5, the incorporation of conducting MWCNT into α-hematite NPs leads to a change in the microstructural parameters due to the creation of stress and oxygen vacancies in the NPs resulting in enhanced active sites in nanocomposites. These changes illustrate better polarization and dielectric constant due to conducting MWCNT and insulating hematite interface creation. The high surface charge has also been achieved in the case of MWCNT incorporated $α-Fe_2O_3$ NPs (CNFNP) than the pure $α-Fe_2O_3$ NPs. The dielectric constant of CNFNP is 1.8×10^5, while pure hematite nanoparticles exhibit ~300. Hence, the MWCNT-decorated natural hematite NPs have been incorporated into self-poled, free-standing PVDF-HFP membrane by varying percentages of 0.5% and 1% namely CNF0.5, CNF1 respectively, and CNF0 represents the pure PVDF-HFP membrane, to improve the properties of the pure membrane, and these all are characterized with the several methods like XRD, FESEM, FTIR etc. which unveils that CNF0.5 exhibits maximum polarizability, β-phase formation. Therefore, CNF0.5 has been used to fabricate a device which can perform as a piezoelectric energy harvester utilizing mechanical energy from different sources such as water flow, wind flow and finger tapping. This device can be able to produce 53.9 V, 7.2 V, and 0.6 V from finger tapping, water flow, and wind flow respectively. This membrane can also degrade RhB dye with 98.7% efficacy. Thus, the device built with CNF0.5 presents a new approach for harvesting energy from two major renewable energy sources: water and wind energy, also

degrading contaminated water. As a result, this has the potential to solve two significant global

issues: the energy crisis and water pollution.

Material	Piezoelectric coefficient (d_{33})	Piezo-voltage	Force	Degraded organic dye	Degradation% (Time in mins)	Reference
BaZrTiO3–BaCaTiO3 /PVDF	600 pC/N	20.61 V	Applying stress – 500 N	N.M	N.M	[1]
MnO2/PVDF	38 pC/N	3.2 V	Hammer Tapping (0.1 MPa)	N.M	N.M	[2]
AlN	N.M	0.7 V	Finger Bending	N.M	N.M	[3]
ZnO-nanorod	N.M	4-6 V	Palm Clapping	N.M	N.M	[4]
MoS$_2$ shell arrays	N.M	1.2 V	Tapping 4.2 kPa	N.M	N.M	[5]
SiO$_2$/ZnO	N.M	0.696 V	Applying force 34 N	N.M	N.M	[6]
Graphene (0.03 wt%)/PVDF–TrFE nanobelts	22.3 pm V^{-1}	35 mV	N.M	N. M	N.M	[7]
Au/ZnO	N.M	54 mV	Electrostimulation	N.M	N.M	[8]
PLLA	3 ± 1 pm V^{-1}	1 V	External force (0.3 MPa)	N.M	N.M	[9]
CaBi$_4$Ti$_4$O$_{15}$ - PDMS	N.M	23 V	Applying force with acceleration 5 m/s^2	N.M	N.M	[10]
P(VDF-TrFE)	−31 pC/N	1.7 V	Applying force 2.3MPa	N.M	N.M	[11]

Bi$_2$WO$_6$ nanosheets	27 Pc/N	N.M	N.M	RhB	80% (80)	[12]
sodium niobate nanowires	12 p.m./V	N.M	N.M	RhB	95% (160)	[13]
BaTiO$_3$/C hybrid	200 pC/N	N.M	N.M	RhB	75.5% (40)	[14]
heat-treated cellulose nanocrystal	N.M	N.M	N.M	RhB	96.6% (180)	[15]
lead zirconate titanate	N.M	N.M	N.M	RhB	37 (150)	[16]
M13 nanopillars-PDMS	10.4 ± 0.5 pm V^{-1}	200 mV	Periodic force (30 N)	N.M	N.M	[17]
Fish Scale Collagen	5.0 pC/N	4 V	Force 0.17 MPa	N.M	N.M	[18]
fish swim bladder	22 pC/N	10 V	Finger impact (1.4 MPa)	N.M	N.M	[19]
Demineralised prawn shell	2.3pC/N	1 V	5.2 kPa	N.M	N.M	[20]
Onion skin-PDMS	2.8 pC N^{-1}	18 V	Mechanical force (17 N)	N.M	N.M	[21]
Treated chicken feather-PDMS	1.6–2.1 pC N^{-1}	10V	Finger impart (0.13–0.31 MPa)	N.M	N.M	[22]
Volcano mud clay based PVDF	50.10pC/N	125V	Hand tapping (12.7N)	N.M	N.M	[23]
Cotton based PVDF	15 pC/N	65 V	Finger tapping 23 N	N.M	N.M	[24]
hydroxyapatite	N.M	N.M	N.M	RhB	92% (30)	[25]
Hematite based membrane	**37.26 pC/N**	**4 V, 4 V**	**Hand tapping (14.99 N), Water droplets**	**RhB**	**94.1% (40)**	**Work in Chapter 3**

Gd-incorporated hematite based membrane	47.32 pC/N	16.92 V, 8V	Finger Tapping (13.49 N), Water flow	RhB	94.3% (35)	Work in Chapter 4
MWCNT-decorated hematite based membrane	139.64 pC/N	53.9 V, 7.2 V, 0.6 V	Finger Tapping (13.91 N), Water flow, Wind flow	RhB	98.7% (30)	Work in Chapter 5

Table 6.1 *Comparison of piezoelectric energy harvesting and piezocatalysis data with*

previous works

Therefore, developing a low-cost, reusable, highly efficient piezoresponsive membrane might be a promising approach in the field of energy generation and water remediation. Enhancing the piezoelectric nature of the fabricated membrane and applying the piezoresponse of the membrane to power generation and catalytic process open up a new avenue for harvesting renewable energy as well as water treatment by degrading dye, pollutants, etc. which has been done throughout this work. Table 1 compares several materials used in piezo-energy harvesting and piezocatalysis, highlighting their efficiency. From the table , it is evident that the efficiency of the device made of hematite conaining nanocomposite is far better than the contemporary devices. Thus, this thesis explores the use of natural rock nanomaterials (α-hematite) based solid state devices to address both the energy issue and water pollution simultaneously and effectively. Hence this work represents a promising way to combat the two significant challenges like energy crisis and water pollution by using cost-effective reusable, biocompatiable, flexible efficient membranes consisting of widely available natural α-hematite.

References

[1] Shin, D.J., Ji, J.H., Kim, J., Jo, G.H., Jeong, S.J. and Koh, J.H., 2019. Enhanced flexible piezoelectric energy harvesters based on BaZrTiO3–BaCaTiO3 nanoparticles/PVDF composite films with Cu floating electrodes. *Journal of Alloys and Compounds*, *802*, pp.562-572.

[2] Zhao, Q., Yang, L., Chen, K., Ma, Y., Peng, Q., Ji, H. and Qiu, J., 2020. Flexible textured MnO2 nanorods/PVDF hybrid films with superior piezoelectric performance for energy harvesting application. *Composites Science and Technology*, *199*, p.108330.

[3] Guido, F., Qualtieri, A., Algieri, L., Lemma, E.D., De Vittorio, M. and Todaro, M.T., 2016. AlN-based flexible piezoelectric skin for energy harvesting from human motion. *Microelectronic Engineering*, *159*, pp.174-178.

[4] Zhang, Z., Chen, Y. and Guo, J., 2019. ZnO nanorods patterned-textile using a novel hydrothermal method for sandwich structured-piezoelectric nanogenerator for human energy harvesting. *Physica E: Low-dimensional Systems and Nanostructures*, *105*, pp.212-218.

[5] Han, J.K., Kim, S., Jang, S., Lim, Y.R., Kim, S.W., Chang, H., Song, W., Lee, S.S., Lim, J., An, K.S. and Myung, S., 2019. Tunable piezoelectric nanogenerators using flexoelectricity of well-ordered hollow 2D MoS2 shells arrays for energy harvesting. *Nano Energy*, *61*, pp.471-477.

[6] Zhao, Y., Fu, Y., Wang, P., Xing, L. and Xue, X., 2015. Highly stable piezo-immunoglobulin-biosensing of a SiO 2/ZnO nanogenerator as a self-powered/active biosensor arising from the field effect influenced piezoelectric screening effect. *Nanoscale*, *7*(5), pp.1904-1911.

[7] Han, Y., Jiang, C., Lin, H., Luo, C., Qi, R. and Peng, H., 2020. Piezoelectric nanogenerators based on helical carbon materials and polyvinyledenedifluoride–trifluoroethylene hybrids with enhanced energy-harvesting performance. *Energy Technology*, *8*(6), p.1901249.

[8] Ma, K., Qi, G., Wang, B., Yu, T., Zhang, Y., Li, H., Kitte, S.A. and Jin, Y., 2021. Ultrasound-activated Au/ZnO-based Trojan nanogenerators for combined targeted electro-stimulation and enhanced catalytic therapy of tumor. *Nano Energy*, *87*, p.106208.

[9] Sultana, A., Ghosh, S.K., Sencadas, V., Zheng, T., Higgins, M.J., Middya, T.R. and Mandal, D., 2017. Human skin interactive self-powered wearable piezoelectric bio-e-skin by electrospun poly-l-lactic acid nanofibers for non-invasive physiological signal monitoring. *Journal of materials chemistry B*, *5*(35), pp.7352-7359.

[10] Hajra, S., Sahu, M., Oh, D. and Kim, H.J., 2021. Lead-free and flexible piezoelectric nanogenerator based on CaBi4Ti4O15 Aurivillius oxides/PDMS composites for efficient biomechanical energy harvesting. *Ceramics International*, *47*(11), pp.15695-15702.

[11] Wang, A., Hu, M., Zhou, L. and Qiang, X., 2019. Self-powered well-aligned P (VDF-TrFE) piezoelectric nanofiber nanogenerator for modulating an exact electrical stimulation and enhancing the proliferation of preosteoblasts. *Nanomaterials*, *9*(3), p.349.

[12] Kang, Z., Qin, N.I., Lin, E., Wu, J., Yuan, B. and Bao, D., 2020. Effect of Bi2WO6 nanosheets on the ultrasonic degradation of organic dyes: Roles of adsorption and piezocatalysis. *Journal of cleaner production*, *261*, p.121125.

[13] Wang, S., Wu, Z., Chen, J., Ma, J., Ying, J., Cui, S., Yu, S., Hu, Y., Zhao, J. and Jia, Y., 2019. Lead-free sodium niobate nanowires with strong piezo-catalysis for dye wastewater degradation. *Ceramics International*, *45*(9), pp.11703-11708.

[14] Chen, L., Jia, Y., Zhao, J., Ma, J., Wu, Z., Yuan, G. and Cui, X., 2021. Strong piezocatalysis in barium titanate/carbon hybrid nanocomposites for dye wastewater decomposition. *Journal of Colloid and Interface Science*, *586*, pp.758-765.

[15] Guan, J., Jia, Y., Chang, T., Ruan, L., Xu, T., Zhang, Z., Yuan, G., Wu, Z. and Zhu, G., 2022. Highly efficient piezo-catalysis of the heat-treated cellulose nanocrystal for dye decomposition driven by ultrasonic vibration. *Separation and Purification Technology*, *286*, p.120450.

[16] Feng, Y., Ling, L., Wang, Y., Xu, Z., Cao, F., Li, H. and Bian, Z., 2017. Engineering spherical lead zirconate titanate to explore the essence of piezo-catalysis. *Nano Energy*, *40*, pp.481-486.

[17] Shin, D.M., Han, H.J., Kim, W.G., Kim, E., Kim, C., Hong, S.W., Kim, H.K., Oh, J.W. and Hwang, Y.H., 2015. Bioinspired piezoelectric nanogenerators based on vertically aligned phage nanopillars. *Energy & Environmental Science*, *8*(11), pp.3198-3203.

[18] Ghosh, S.K. and Mandal, D., 2016. High-performance bio-piezoelectric nanogenerator made with fish scale. *Applied Physics Letters*, *109*(10).

[19] Ghosh, S.K. and Mandal, D., 2016. Efficient natural piezoelectric nanogenerator: Electricity generation from fish swim bladder. *Nano Energy*, *28*, pp.356-365.

[20] Ghosh, S.K. and Mandal, D., 2017. Bio-assembled, piezoelectric prawn shell made self-powered wearable sensor for non-invasive physiological signal monitoring. *Applied Physics Letters*, *110*(12).

[21] Maiti, S., Karan, S.K., Lee, J., Mishra, A.K., Khatua, B.B. and Kim, J.K., 2017. Bio-waste onion skin as an innovative nature-driven piezoelectric material with high energy conversion efficiency. *Nano Energy*, *42*, pp.282-293.

[22] Kar, E., Barman, M., Das, S., Das, A., Datta, P., Mukherjee, S., Tavakoli, M., Mukherjee, N. and Bose, N., 2021. Chicken feather fiber-based bio-piezoelectric energy harvester: an efficient green energy source for flexible electronics. *Sustainable Energy & Fuels*, *5*(6), pp.1857-1866.

[23] Das, N., Sarkar, D., Saikh, M.M., Biswas, P., Das, S., Hoque, N.A. and Ray, P.P., 2022. Piezoelectric activity assessment of size-dependent naturally acquired mud volcano clay nanoparticles assisted highly pressure sensitive nanogenerator for green mechanical energy harvesting and body motion sensing. *Nano Energy*, *102*, p.107628.

[24] Tiwari, S., Devi, A., Dubey, D.K. and Maiti, P., 2023. Induced Piezoelectricity in Cotton-Based Composites for Energy-Harvesting Applications. *ACS Applied Bio Materials*, *6*(4), pp.1536-1545.

[25] Yin, G., Fu, C., Zhang, F., Wu, T., Hao, S., Wang, C. and Song, Q., 2023. Piezocatalytic degradation of organic dyes and production of H2O2 with hydroxyapatite. *Journal of Alloys and Compounds*, *937*, p.168382.

Appendices
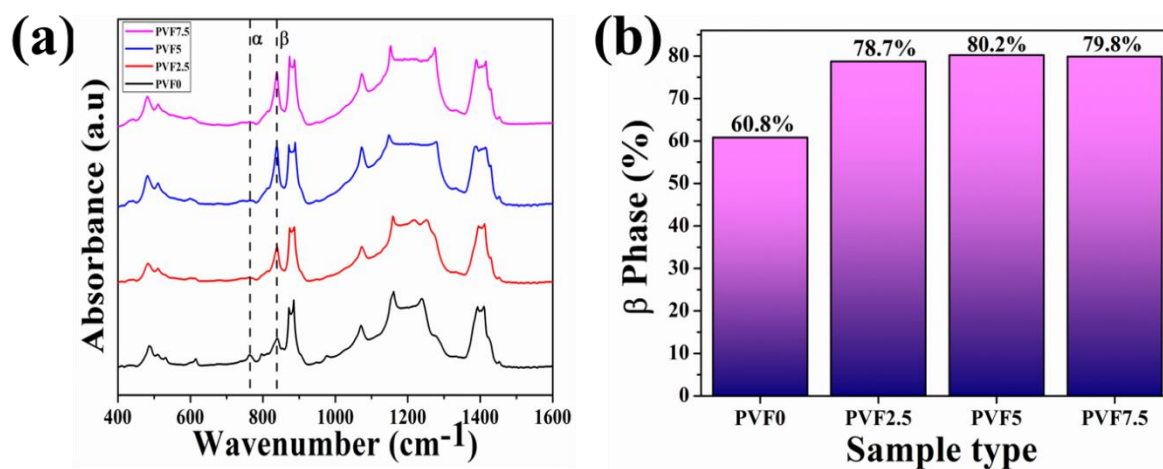
Appendix 1

Supporting information of Chapter 3

Figure A1.1 *(a) FTIR Spectra (b)) β-Phase of sample PVF0, PVF2.5, PVF5, PVF7.5*

DFT data of PVF5

Number of atoms: 32   Geometry Index: 15

Coordinates:

C	-6.361250548849	3.456684508055	0.403776106803
C	-5.712759886923	2.180675716220	-0.139030589363
C	-4.210391193214	1.989240721261	0.121583417226
C	-3.311276808246	3.153649789200	-0.273433625826
H	-3.900196002897	1.099879278268	-0.432318497647
H	-4.073763377038	1.776177650497	1.185409876884
C	-1.837624553660	3.137006695374	0.133969459667
C	-0.992883590773	1.927559420730	-0.237616314867
H	-1.784058919791	3.274071709701	1.217391824230
H	-1.402432095074	4.023222258441	-0.327769537380
C	0.476785510291	1.957057630586	0.207675975996
C	1.259878108803	3.224199300963	-0.129006691091
H	0.966716161336	1.095740127497	-0.252746155255
H	0.513702891497	1.807186814678	1.290559246462

C	2.739336494803	3.253003137613	0.248535594663
C	3.571072019273	2.092672370560	-0.269767585383
H	2.829028007473	3.298564195517	1.339036411788
H	3.134764135227	4.191242779191	-0.158681709758
F	-7.734312310311	3.331295665454	0.331526483745
H	-6.046888902311	4.310205166491	-0.198104179817
H	-6.070716041227	3.614215683687	1.447271003673
F	-5.962586232655	2.105154848497	-1.483242200500
F	-6.342725037831	1.103789142352	0.438949626296
F	-3.405993534656	3.365992854754	-1.620365637848
F	-3.798677605873	4.308178396490	0.337063063398
F	-1.052394884228	1.710253565307	-1.587613286124
F	-1.543350044146	0.802330461851	0.359091378569
F	0.672137095388	4.303271548564	0.514593270625
F	1.150883725510	3.482278229827	-1.476476272057
F	3.287663004320	0.938119797308	0.461616876793
H	4.638048335558	2.311997861721	-0.147169879118
H	3.363936080220	1.890972673344	-1.328197454783

S3: PVF0 DFT data

Number of atoms: 32   Geometry Index: 45

  Coordinates:

C	-8.376656599044	2.591866676610	-0.103459324393
C	-7.223352733353	3.576730485767	-0.123249902508
H	-8.294481265544	1.889786110133	-0.938485188236
H	-9.310316937008	3.153310401755	-0.202108556328
H	-8.395106822477	2.029081295828	0.834735914917
C	-5.842242416237	2.930668655909	0.006768601294
C	-4.669844664580	3.903255178718	0.038838938750
H	-5.690730671289	2.255579895818	-0.840126483992

H	-5.812802815587	2.332438683744	0.921808479146
C	-3.289113650659	3.214344470076	0.148180122471
C	-2.109426629645	4.167186917575	0.191001978083
F	-7.395718914547	4.484175365345	0.893726948602
F	-7.290126721322	4.288671032020	-1.297059162562
C	-0.773119569135	3.427104892091	0.073167215451
C	0.416716632116	4.380285209724	0.039822240355
H	-0.763749569322	2.830663329812	-0.844804243846
H	-0.639319624426	2.737276892054	0.913596884166
C	1.744860723354	3.686063538425	-0.260688770483
F	-4.645557399828	4.656840270127	-1.102177887291
F	-4.769057620794	4.755472613053	1.101342942248
F	-3.179912510535	2.365620799171	-0.928679319186
F	-3.303847647340	2.427636693135	1.274773560786
F	0.505227947116	5.038127056993	1.242535580415
F	0.187765865559	5.344154259741	-0.916230641418
C	2.981720192059	4.568727418863	-0.164324678013
H	1.689523438723	3.269835579445	-1.272035085723
H	1.877743944745	2.850368934964	0.434585491237
H	-2.214554851945	4.878808246016	-0.631126616867
H	-2.163354759393	4.730894445093	1.126370821297
F	2.828705059748	5.704095304075	-0.904481622030
F	3.211303191473	4.934443767550	1.130537873512
H	3.875647399116	4.045995580371	-0.527626109853

Appendix 2
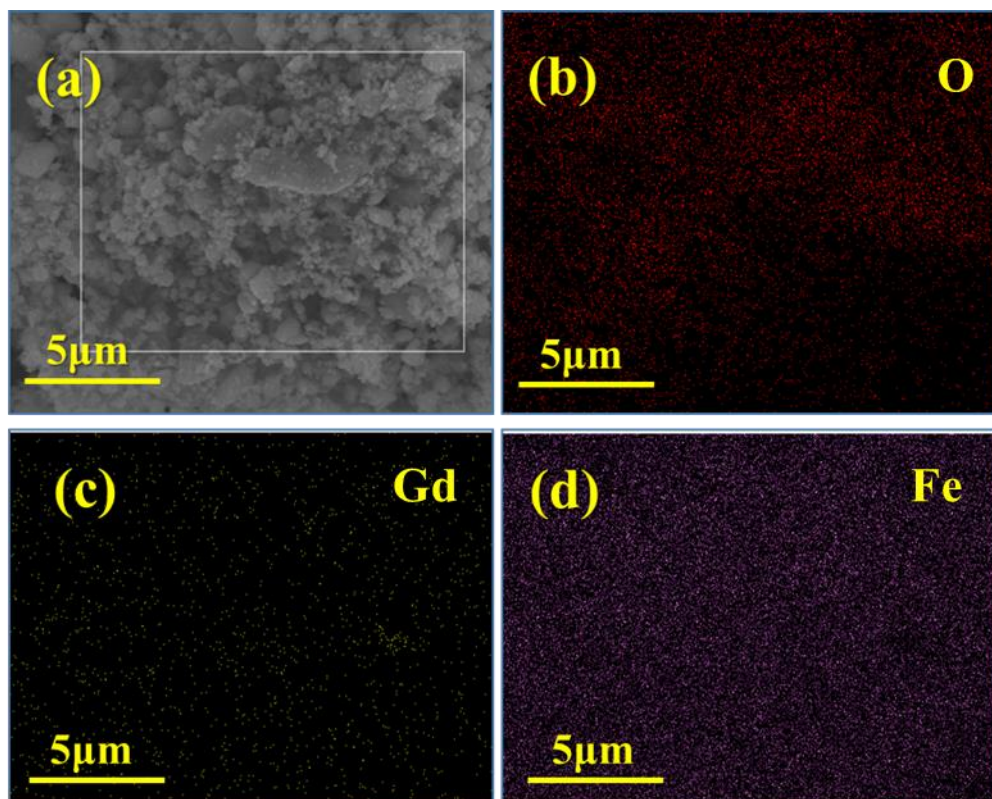
Supporting information of Chapter 4

Figure A2.1 *Gd incorporated α-hematite (a) and mapping (b-d) of PVGF2.5 membrane suggesting the homogeneous distribution of doped Gd incorporated in α-hematite*
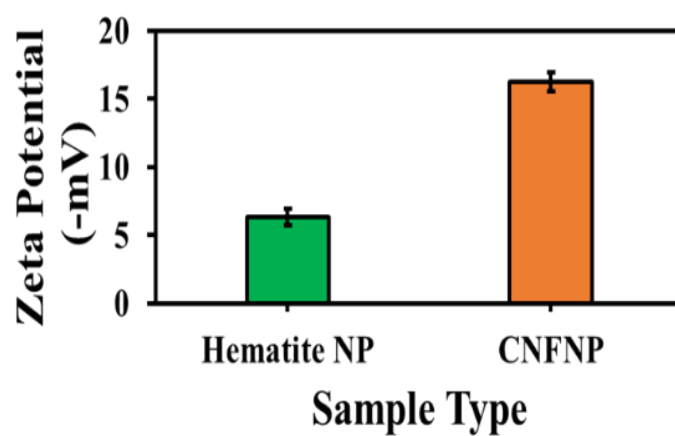
Appendix 3

Supporting information of Chapter 5

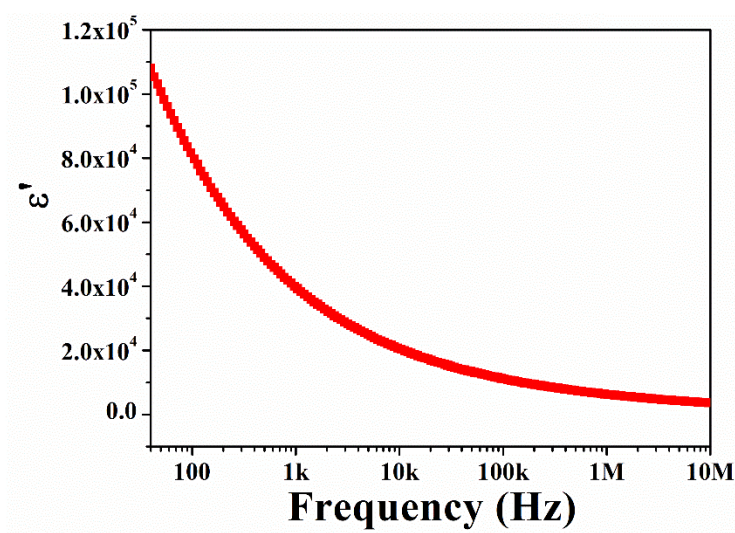**Figure A3.1** *Zeta Potential of MWCNT incorporated α-hematite*

Figure A3.2 *Dielectric constant of CNFNP*

Appendix 4

Copyrights

Thank you for your order!

Dear Miss. Saheli Ghosh,

Thank you for placing your order through Copyright Clearance Center's RightsLink®
service.

Order Summary

Licensee:	Miss. Saheli Ghosh
Order Date:	May 16, 2024
Order Number:	5790771390055
Publication:	Journal of Environmental Sciences
Title:	One-step preparation of MoO x /ZnS/ZnO composite and its excellent performance in piezocatalytic degradation of Rhodamine B under ultrasonic vibration
Type of Use:	reuse in a thesis/dissertation
Order Total:	0.00 USD

View or print complete details of your order and the publisher's terms and conditions.

Sincerely,

Copyright Clearance Center

Thank you for your order!

Dear Miss. Saheli Ghosh,

Thank you for placing your order through Copyright Clearance Center's RightsLink®
service.

Order Summary

Licensee:	Miss. Saheli Ghosh
Order Date:	May 16, 2024
Order Number:	5790780290262
Publication:	Journal of Colloid and Interface Science
Title:	Effective promoting piezocatalytic property of zinc oxide for degradation of organic pollutants and insight into piezocatalytic mechanism
Type of Use:	reuse in a thesis/dissertation
Order Total:	0.00 USD

View or print complete details of your order and the publisher's terms and conditions.

Sincerely,

Copyright Clearance Center

Thank you for your order!

Dear Miss. Saheli Ghosh,

Thank you for placing your order through Copyright Clearance Center's RightsLink® service.

Order Summary

Licensee:	Miss. Saheli Ghosh
Order Date:	May 16, 2024
Order Number:	5790780791939
Publication:	Journal of Environmental Chemical Engineering
Title:	Synthesis and characterization of ZnO-GO composites with their piezoelectric catalytic and antibacterial properties
Type of Use:	reuse in a thesis/dissertation
Order Total:	0.00 USD

View or print complete details of your order and the publisher's terms and conditions.

Sincerely,

Copyright Clearance Center

NATIONAL SEMINAR

On

Physics at Surfaces and Interfaces of Soft Materials (PSISM-2019)

Organised by Condensed Matter Physics Research Centre,
Department of Physics, Jadavpur University, Kolkata – 700032.

CERTIFICATE OF PARTICIPATION

This is to certify that Mr./Mrs/Dr./Prof. _Saheli Ghosh_

Has participated/presented (oral/poster) a paper entitled _Boehmite based 'MFNS³_

... Conversion ... In the seminar on

Physics at surfaces and interfaces of soft materials (PSISM-2019) during 26-27 st September, 2019 held at

Department of Physics, Jadavpur University, Kolkata – 700032.

Prof. B. D. Chattopadhyay

Dr. Sanat Karmakar
(Conveners)

DST-SERB Sponsored

One Day Workshop on Material Synthesis & Characterization Techniques

Organized by: Department of Physics, Jadavpur University, Kolkata-700032

Certificate of Presentation

This Certificate is awarded to

Mr./ Ms. .. Saheli . Ghosh. . . . . .for successfully presenting a paper entitled Optical Characterisation . in the Workshop organized by Department of Physics, Jadavpur University, Kolkata on 29th February 2020

28/02/2020

Head, Department of Physics, Jadavpur University

Certificate No :
UXFZPO-CE000028

Basanti Devi College
Certificate of Participation

This is to certify that

Saheli Ghosh   of **Jadavpur University**

has participated in the One-day International Webinar on "New Outlooks in Modern Physics" organized by the Department of Physics, in collaboration with IQAC, Basanti Devi College on 17th July (Friday) 2020.

Dr. Sima Gupta Roy
HOD, Dept. of Physics
Basanti Devi College

Dr. Aditi Sarkar
Coordinator, IQAC
Basanti Devi College

Dr. Indrila Guha
Principal
Basanti Devi College

Sree Narayana College for Women, Kollam, Kerala

Affiliated to the University of Kerala and Accredited with Grade B (CGPA 2.68) by NAAC

ONE CASTE ONE RELIGION ONE GOD

International Webinar series

CROSSROADS 2020

22nd to 30th July 2020

Certificate of Participation

This is to certify that **Saheli Ghosh, Researcher, Physics, Jadavpur University** has participated in the **International Webinar** on '**Nanotechnology Against COVID-19**', Organised by Post Graduate and Research Department of Chemistry, Sree Narayana College for Women, Kollam, Kerala, India on **23 July 2020.**

Dr. Poornima Vijayan P.
Convenor

Dr. Chithra P.G.
Co-ordinator

Dr. Nisha J. Tharayil
Principal

Dr. Chithra P.G.
Head of the Department

ASUTOSH COLLEGE

92, S. P. Mukherjee Road

Kolkata – 700 026

Website: www.asutoshcollege.in , E-mail: mail@asutoshcollege.in

Two Day National Webinar on Fundamental Physics

Organized by

Department of Physics, in Collaboration with IQAC, Asutosh College

Certificate of Participation

This is to certify that ,

Smt. Saheli Ghosh of Jadavpur University,

has participated in the webinar on '*Role of Symmetries in Physics*' presented by Dr. Biswarup Mukherjee, HAG Professor, Department of Physical Science, IISER, Kolkata, held on 27ᵗʰ August, 2020.

&

on '*Quasiperiodic order in Physics*', presented by Dr. Arunava Chakrabarti, Professor, Presidency University, held on 28ᵗʰ August, 2020.

Tathagata Raychaudhuri

Dr.Tathagata Ray Chaudhuri

Co-ordinator IQAC, Asutosh College

Smita Sarathi Bhattacharya

Dr. S.S.Bhattacharyya

Convenor & H.O.D.

Dept. of Physics, Asutosh College

Manas Kabi

Dr. Manas Kabi

Bursar, Asutosh College

Prof. Apurba Ray

Vice-Principal, Asutosh College

Dated: 30-08-2020

SRM INSTITUTE OF SCIENCE AND TECHNOLOGY

Kattankulathur - 603 203, Tamil Nadu, India.

7th International Conference on Nanoscience and Nanotechnology (ICONN-2023)

(Virtual Conference) March 27 - 29, 2023

Certificate of Participation

This is to certify that **Mr./Ms./Dr. Saheli Ghosh** has participated and presented a paper entitled **Piezoelectric energy generation under finger tapping and water flow using Gd-incorporated natural hematite decorated PVDF-HFP membrane** in the 7th International Conference on Nanoscience and Nanotechnology (ICONN-2023) organized by Department of Physics and Nanotechnology, SRM IST, India during March 27 - 29, 2023, in association with Shizuoka University, Japan; National Yang Ming Chiao Tung University, Taiwan; GNS Science, New Zealand; University of Rome Tor Vergata, Italy, Asian Consortium on Computational Materials Science (ACCMS), Japan; Indian Ceramic Society; Indian Physics Association (IPA); Solar Energy Society of India (SESI); Innovation, Science & Technology Foundation - Tirupati (ISTF-T) and co-sponsored by Defence Research and Development Organization (DRDO), India; Council of Scientific & Industrial Research (CSIR), India; The Indian Science Congress Association (ISCA) and Springer Nature.

Head
Department of Physics and Nanotechnology
SRM IST, KTR

Chairperson
School of Applied Sciences
SRM IST, KTR

450

ASSOCIATION OF INDIAN UNIVERSITIES, DELHI
&
THE ASSAM ROYAL GLOBAL UNIVERSITY, GUWAHATI

ANVESHAN 2022

EAST ZONE STUDENT RESEARCH CONVENTION

CERTIFICATE

This is to certify that

Mr./Ms./Dr. _Saheli Ghosh_

Son/Daughter of Shri _Sanjay Kr. Ghosh_ enrolled in _PhD._

Department / Faculty of _Physics_

Jadavpur University / Institute participated in East Zone Student Research

Convention held at The Assam Royal Global University, Guwahati during March 01-02, 2023.

His/Her proposal/project entitled _VIKRAM: an "all-in-one" module for combating water pollution and energy crisis_

under the category of _Basic Science (2nd Position)_

Dr. Usha Rai Negi
Assistant Director (Research)
Association of Indian Universities,
New Delhi

Prof. (Dr.) Rohit Singh
Pro Vice-Chancellor
Zonal Coordinator- Anveshan 22
The Assam Royal Global University, Guwahati

Prof. (Dr.) S.P. Singh
Vice-Chancellor
The Assam Royal Global University
Guwahati

Ganpat University
|| विद्यया समाजोन्नतिः ||

ANVESHAN

National Student Research Convention
March 16-17, 2023

Certificate of Participation

This is to Certify that Mr / Ms. _Sabeli Ghosh_

affiliated with _Jadavpur University_

_____ has participated in **Anveshan: National**

Student Research Convention organized by Association of Indian Universities, New Delhi and hosted by Ganpat University, Gujarat during

March 16-17, 2023. He/She presented a Research Project titled _Vikran: An "All - in - one" model._

by combating water pollution and energy crisis

under the category of _Basic Sciences_

Dr. Kiran Amin
Anveshan Co-convener
Deputy Pro Vice Chancellor
Ganpat University

Dr. Ajay Gupta
Anveshan Convener
Director - R&D
Ganpat University

Dr. Amarendra Pani
Anveshan Convener
Joint Director (Research)
Association of Indian Universities

Dr. Mahendra Sharma
Pro-Chancellor & Director General
Ganpat University

Powered by
ongc

INSTITUTION'S
INNOVATION
COUNCIL

G20

PROJECTSET
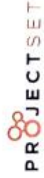
A one-day seminar in

"COMMEMORATION OF CENTENARY BIRTH ANNIVERSARY OF PROF. SHYAMAL SENGUPTA"

Condensed Matter Physics Research Centre
Estd. 1990

Organised by

Condensed Matter Physics Research Centre & Department of Physics, Jadavpur University

CERTIFICATE OF PARTICIPATION

This certificate has been awarded to **Saheli Ghosh** of Dept. Of Physics, Jadavpur University in appreciation of her poster presentation titled **Natural rock-based polymeric membrane: an "all-in-one" module for combating water pollution and energy crisis**

at the one day seminar in "Commemoration Of Centenary Birth Anniversary Of Prof. Shyamal Sengupta" held at Jadavpur University, Kolkata, India on 7th February 2024.

07.02.2024

H.O.D. Dept. Of Physics, JU

7/02/2024

Co-Ordinator CMPRC, JU